Nanoscale Ordering of Coordination Compound and Networks at Solid Surfaces

Marta Karolina Trelka

Solid State Physics Department

Universidad Autónoma de Madrid

2010

THESIS FOR DEGREE OF DOCTOR OF PHILOSOPHY

Under supervision of Dr. Roberto Otero Martín and Dr. José María Gallego Vázquez

UAM
UNIVERSIDAD AUTONOMA
DE MADRID

Contents

Resumen

En esta tesis se va a estudiar el crecimiento de moléculas orgánicas que tienen o pueden formar un enlace de coordinación con átomos metálicos en su estructura. Hemos decidido investigar porfirinas y subftalocianinas que representan grandes estructuras aromáticas, y además, por otra parte, el acido oxálico que es una molécula pequeña, de solo dos grupos carboxílicos, capaz de formar enlaces de coordinación con metales de transición como el hierro.

Las técnicas experimentales básicas para las estudios de estos sistemas han sido el microscopio del efecto túnel (STM, *Scanning Tunneling Microscopy*) y la espectroscopia de fotoemisión de rayos X (XPS, *X-Ray Photoemission Spectroscopy*) bajo condiciones de ultra alto vacio (UHV, *Ultra-High Vacuum*). Gracias a estas técnicas podemos sacar informaciones cualitativas y cuantitativas de nanostructuras orgánicas.

En la parte experimental se van a presentar estudios de porfirinas de zinc sobre superficies de cobre y oro, distintas especies de subftalocianinas (de cloro o fluor añadido en los grupos fenilos o en el centro de anillo aromático) y los estudios de acido oxálico con hierro evaporado posteriormente en sobre la superficie para obtener un enlace de coordinación.

Dichas moléculas pueden tener gran importancia en las aplicaciones en optoelectrónica o células solares y en sistemas biológicos gracias sus propiedades de auto-organización en grandes estructuras en el nivel manométrico.

Introduction

The XX century opened new possibilities for Science in many different ways. In particular, many advances in knowledge took place because of the development of new instrumentation. One example of this is the Scanning Tunneling Microscope (1) (2), a technique which has played a significant role for our understanding of the processes at the atomic scale. In recent years it has been shown that STM and other techniques can be used for the investigation of the adsorption and self-assembly of organic compounds at the nanoscale, and from these investigations we can extract important information about the physical interactions that control these processes with implication for chemistry or biology (3) (4) (5) (6) (7)

In particular it was shown that codeposition of metallic atoms with organic material might lead to the self-assembly of a mixed compound in which metallic atoms are linked together by organic ligands (8). Such structures have been named 2D Metal-Organic Coordination Networks (2D MOCN's) in analogy to the well known 3D Metal-Organic Frameworks, compounds with a great variety of applications ranging from catalysis to magnetism, and consisting in 3D lattices of metal ions linked by coordination bonds with organic ligands. The purpose of this thesis is to explore the nature and strength of these coordination bonds to direct the growth of novel nanostructures with well defined shape and size that should optimize its performance in a number of possible applications. In nature there are a lot of examples of coordination compounds between organic materials and metallic ions; for example in hemoglobin an iron center is coordinated through four nitrogen atoms to the aromatic ring; another example is chlorophyll, whose porphyrin ring is coordinated to a magnesium atom.

First we will show experiments with porphyrin molecules, large organic macrocycle molecules which contain a Zn atom in its structure. This atom will be shown to be significant for the metal-organic bonding of neighboring molecules through oxygen bridges. The analysis techniques which will be used are Scanning Tunneling Microscopy (STM) and X ray Photoemission Spectroscopy (XPS).

Another experiment presented in this thesis will be investigation of subphthalocyanine (SubPc) molecules on a copper surface. As in the case of porphyrins, the subphtalocyanine molecule is a large macrocycle aromatic compound with a boron atom in the center of the macrocycle ring linked to the heteroatoms at the aromatic ring and to another axial ligand (in our case chlorine or fluorine atoms). For this molecule we expect a strong molecule-molecule interaction because of the high dipole moment along the boron-ligand axis.

In the last part we will tackle the study of metal-organic bonding in the small dicarboxylic molecule (Oxalic Acid) at copper and gold surfaces. The purpose of this investigation is to create a coordination network together with magnetic iron atoms. The distance in between two iron atoms is very small in comparison to other reported

studies. This small distance suggests that the system might show magnetic properties. For the understanding of the self assembly of this structure we will use STM and XPS. .

Chapter 1: Experimental techniques

As explained in the introduction, the purpose of the thesis is to investigate the role that metal-organic bonds play into the self-assembly and adsorption of different organic molecules. We therefore need not only information about the structure of the molecules, but also about their chemical state (for example if one particular group is deprotonated or not).

The main techniques used for the experiments were Scanning Tunneling Microscopy and X-Ray Photoemission Spectroscopy. In some cases complementary information is obtained by additional techniques such as NEXAFS (Near Edge X-ray Absorption Fine Structure) and theoretical calculations based on DFT (Density Functional Theory).

1.1 Experimental set-up

The equipment used for the experiments consists of an ultra high vacuum system with a commercial Aarhus-type variable temperature microscopy (possibility to cool down till 80 K and scanning between 80 and 230 K). Besides microscopy, the chamber also contains a mass spectrometer, a LEED/Auger optics, and facilities in the preparation chamber for performing the cleaning of the sample and the evaporation of the molecules. The experiments were carried out in a base pressure of 10^{-10} mbar. A picture and a scheme of the Ultra High Vacuum (UHV) (9) system are shown in Figure 1.

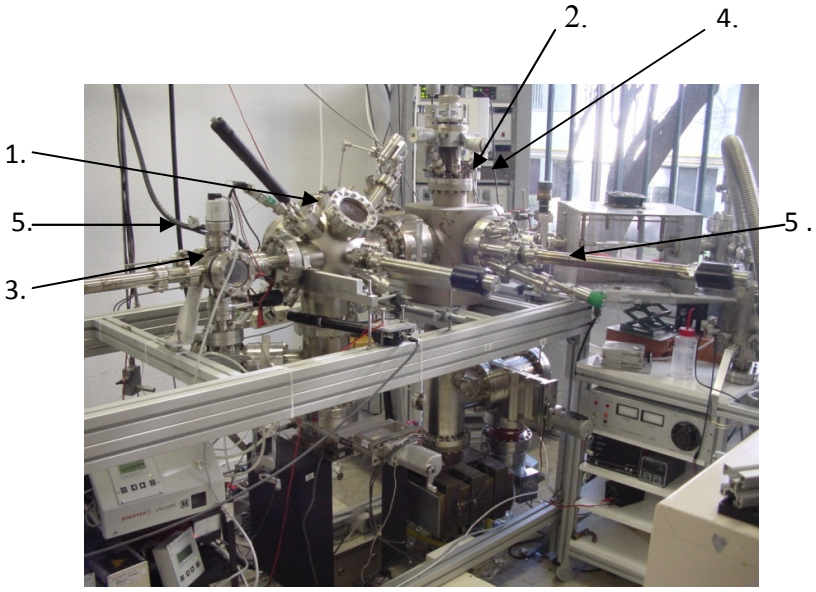

1. STM chamber
2. Pre chamber
3. MOKE chamber
4. LEED/Auger
5. Evaporators

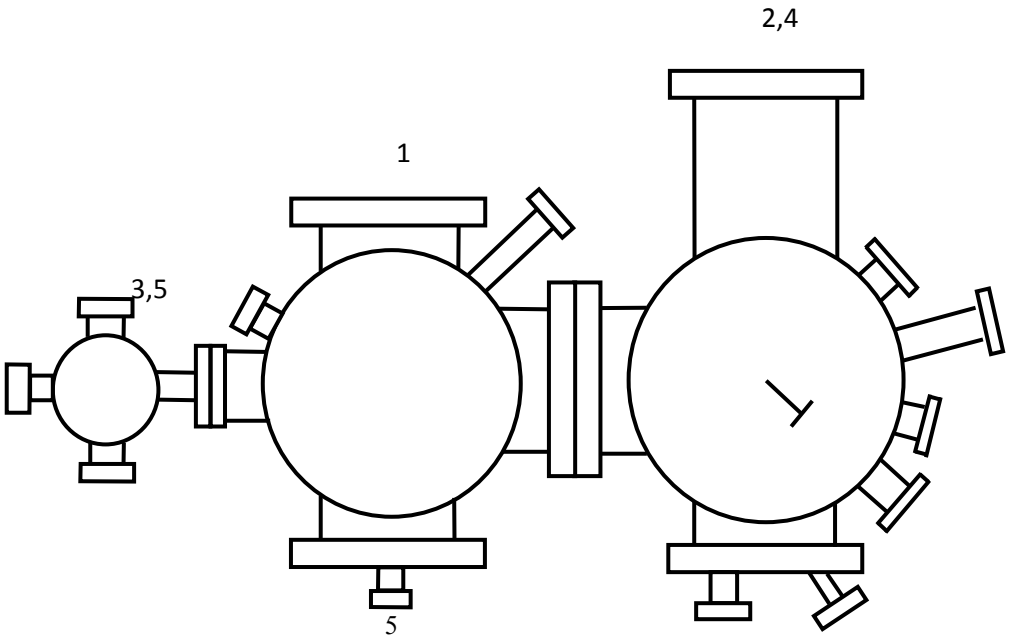

Figure 1. Experimetal set-up.

1.2 STM theory

The principle of the STM is electron tunneling, i.e. the passage of one electron between two conductors separated by a potential barrier higher than the electron's kinetic energy. It was first observed in macroscopic conductor-insulator-conductor junctions for applied voltages between the conductors smaller than the insulator energy gap. In Figure 2 a schematic representation of tunneling junctions in a planar conductor-insulator-conductor model is shown. (2)

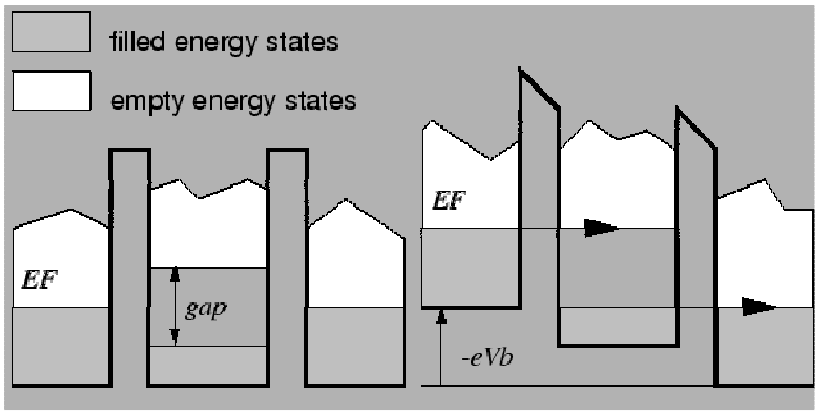

Figure 2. Tunneling junction diagram showing the tunneling of electrons through thin insulating layers for applied voltages below the gap.

STM differs from planar junctions in that the insulator is replaced by vacuum and we have 3D variation of the tunneling current. To understand properly the three dimensional STM theory we should define the electron potential in the tunnel gap between sample and the tip, describe the electronic states of the tip and surface and a wave function of the tunneling electrons in the tunnel gap.

The theories of the STM are mainly based on the Bardeen formalism. In this case the interaction between surface and the tip is very weak and can be neglected; the tunnel current can be obtained from the separated tip and sample potentials. A straight forward calculation yields:

$$I = \frac{2\pi e}{\hbar} \iint_{\mu,\nu} d\mathbf{k}_\mu d\mathbf{k}_\nu \rho_{punta}\left(\mathbf{k}_\mu\right) \rho_{muestra}\left(\mathbf{k}_\nu\right) \left[f\left(E_\mu\right) - f\left(E_\nu + eV\right) \right] \left| M_{\mu\nu} \right|^2 \delta\left(E_\mu - E_\nu - eV\right)$$

where μ and ν corresponds to the electronic states of the tip and sample with moments $\mathbf{k}_\mu$ and $\mathbf{k}_\nu$ respectively; densities of states are showed as $\rho_{punta}\left(\mathbf{k}_\mu\right)$ and $\rho_{muestra}\left(\mathbf{k}_\nu\right)$; and $M_{\mu\nu}$ is a matrix of transmission between states of the tip and surface.

The transfer Hamiltonian approach was applied to the STM theory by Tersoff and Hamann (10) (11). They considered small voltages and made the assumption that the tip is spherical with radius R. Having this in mind, the matrix M can be described only by spherically symmetric s-wave functions. In the Tersoff-Hamann approximation, STM images are determined by the contours of constant density of states at the Fermi level.

The decay length for the wave-functions of the electron at the tip and at the surface in vacuum determines the tunnel barrier. Tunnel current consequently decreases exponentially with increasing the distance *d* between the tip and surface.

$$I \propto \exp\ -2\mathrm{d}\frac{\sqrt{2\mathrm{m}\Phi}}{\hbar}$$

where *m* is the electron mass, Φ is the apparent barrier height, closely related to the surface work function, and ħ is the Planck`s constant. For typical work function values of 4 eV, when the distance is changed by 1 Å the tunnel current decreases in factor of ten. (12) (1) (13)

1.3 Variable Temperature Scanning Tunneling Microscopy (VT-STM)

As described in the previous paragraph, the principle of the technique is the tunneling current that appears between a metallic tip and a conductive sample when their electronic wave functions start to overlap. The tip, made usually of W or PtIr, is approached to the surface at a distance (around 5 Å) (1) (12) where the overlap between wave functions of the sample and tip can occur. When we applied a bias voltage V_t,, electrons can tunnel from the sample to the tip (or the other way around depending on the polarity of the applied bias) and at this conditions some current I_t (for voltages in the range of volts and tip-sample distances below 1 nm, the current is in the range of nano ampers) is established. The basic scheme of the Aarhus type STM from SPECS (14) is shown below in Figure 3.

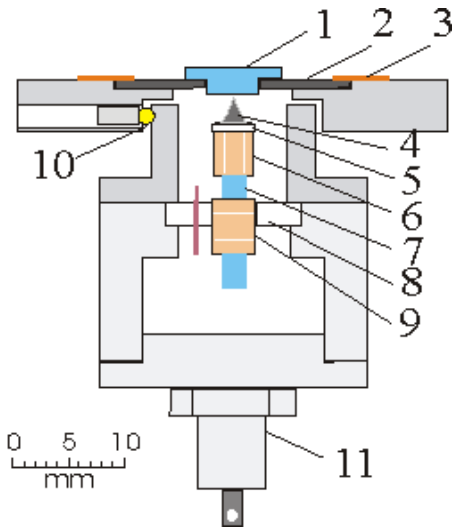

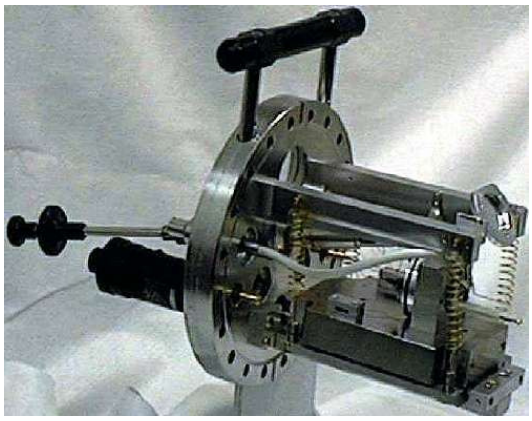

1. Sample
2. Sample holder
3. Clamps
4. Tip
5. Tip holder
6. Scanning tube
7. Motor tube for approaching
8. Motor mechanism
9. Approaching mechanism
10. Quartz
11. Zener Diods

Figure 3. Scheme of the Aarhus type STM.

The Aarhus type microscope consists of two piezoelectric tubes, one responsible for the x, y and z movement of the tip (scanning tube) and a linear motor for the positioning of the tip (motor tube). When voltage of different polarity is applied to two opposite electrodes of the scanning tube, one expands and the other contracts, and in this way x and y scanning in the surface plane is achieved. For z axial motion the

voltages of the inner electrode has to be changed. The compact construction of the microscope leads to fast scanning with reduced external vibrations. (2) We can distinguish two different imaging modes, one with the constant current and other with fixed distance tip-surface (Figure 4). The Aarhus type microscope works in both conditions. (1)

- *Constant current mode*: in this case the tip is scanning the surface at constant tunnel current with the preset values and continuously adjusting the vertical position of the tip with the feedback voltage V_z

- *Constant height mode*: in this case the tip can be rapidly scanned at constant average z position with respect to the surface, and it is the value of the tunneling current that maps the surface corrugation.

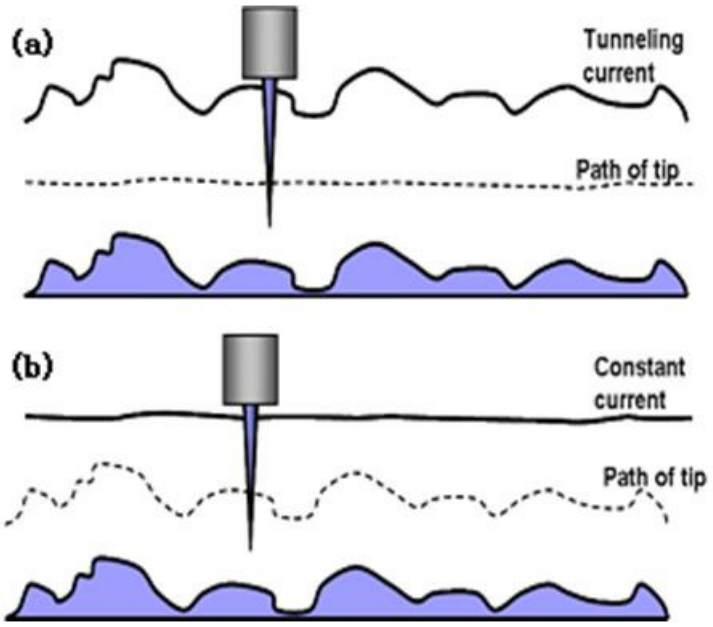

Figure 4. Different imaging modes, a constant height b constant tunneling current

For the purposes of this thesis it will be important to keep in mind that STM images not always directly reflect the surface topography, but on the contrary electronic effects might have considerable weight in determining the shape of the STM images.

1.4. X -Ray Photoemission Spectroscopy

This spectroscopic technique allows us to investigate the geometric structure, chemical composition and electronic properties of solid surfaces .The basics of the technique is related to the photoelectric effect (15) (16): photon irradiation induces emission of electrons from the surface provided that the photon energy hν is higher than work function.

When the photon energy of the incoming beam is in the X ray-range, photoemission from both the core levels and valence levels into the vacuum occurs. The

core levels are inner quantum shell states and do not play a role in chemical bonding, opposite to valence-level electrons. As a first approximation, electrons which are deep inside the atoms are relatively insensitive to their surroundings and even condensed in the solid phase they retain the binding energies E_b that are signature of the chemical nature of atom. On the other hand, the outer electrons participate in chemical bonding in a solid and the valence band energies are affected by the whole electronic structure of the solid, and not just the chemical nature of the atoms (17).

However, looking in more detail to the energy position of the core levels in a solid or in a molecule it becomes obvious that even though the electrons in the core levels do not participate directly in chemical bonding, its fine structure and energy levels do depend slightly on the chemical environment of a given atom. For example, atoms linked to strongly electronegative groups will be partially deprived of charge. This will make the remaining electrons feel more tightly bonded to the nucleus, due to the reduction in electron-electron repulsion and, therefore the level will be shifted to higher binding energies. This is the well known chemical shift effect which will enable us to extract information on the local environment of each chemical species adsorbed on a surface.

The kinetic energy of emitted photoelectron can be written E_{kin}:

$$E_{kin} = h\nu - E_B + \varphi$$

where $h\nu$ is the energy of the incoming photon, E_B is the binding energy with respect to the Fermi level of the solid and φ is the work function of the sample. $E_B+\varphi$ can thus be interpreted as the binding energy of the electron in a solid with respect to the vacuum level.

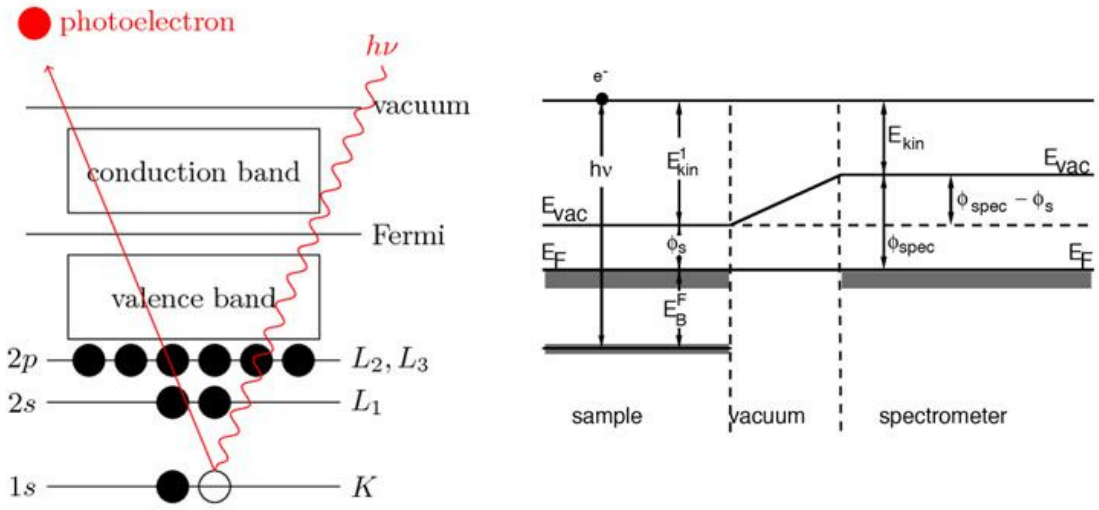

Figure 5. Schematics of the XPS process.

The photon energy hν is equal to the energy available to excite a core electron. Nevertheless some photon energy is lost to overcome the potential barrier energy associated with the interaction energy of the electron in the nucleus $E_B+\varphi$. The remaining energy after this process is transformed into the kinetic energy of the photoemitted electrons. From this it is clear that for a fixed photon energy, photoemission from the atoms with well defined core levels will give photoelectrons with well known kinetic energies changing systematically from the element to the element. (18) (19) (see Figure 5).

Experimentally we need to determine the electron energy distribution, i.e. the number of detected electrons N(E) as a function of their kinetic energy. For that purpose the analyzer is built of two electrically isolated hemispheres with a potential difference in between them. This analyzer (See Figure 6)is working as follows: only electrons of a chosen kinetic energy (pass energy) can flow through the detector because of the electrostatic field which separate electrons. Electrons of kinetic energy higher or lower than the chosen one are neutralized and lost in the inner or outer hemisphere. To produce a photoelectron spectrum the electron kinetic energies have to be slowed down by the use of a negative electrode. By changing the negative voltage at this electrode, electrons with differing kinetic energies can be allowed through the analyzer to the detector. We measure the kinetic energy but usually the binding energy is shown in the spectra. Such binding energies are used to characterize the chemical nature and chemical environment of the elements present in the sample (20) (21) .

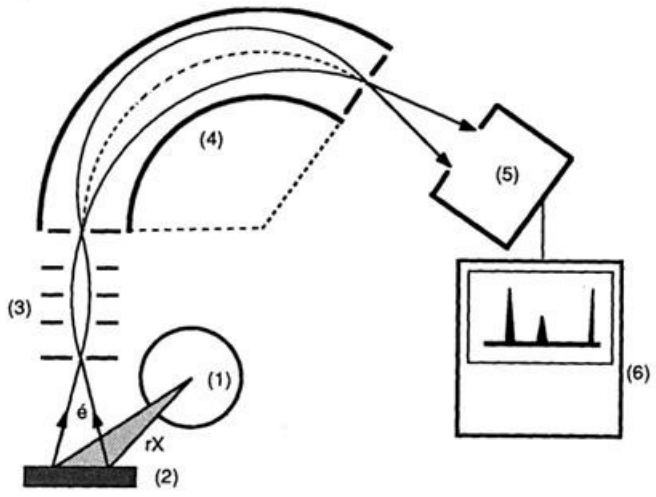

Figure 6. XPS analyzer. (1) X-rays tube; (2) Sample; (3) Electronic focusing system; (4) Spectrometer; (5) Electrons detector (channeltron); (6) Data acquisition.

1.5 Preparation of the surface.

For the preparation of the surface repeated processes of sputtering and annealing were used. First, the metallic surface was sputtered by Ar^+ ions with energy of 1 keV for 10 minutes, in this way we are able to clean the sample from the chemical contaminants and after this the annealing procedure till 800 K for also 10 minutes to recrystallize the surface. In this way we are able to achieve an atomically clean surface as an example is shown Cu (111).

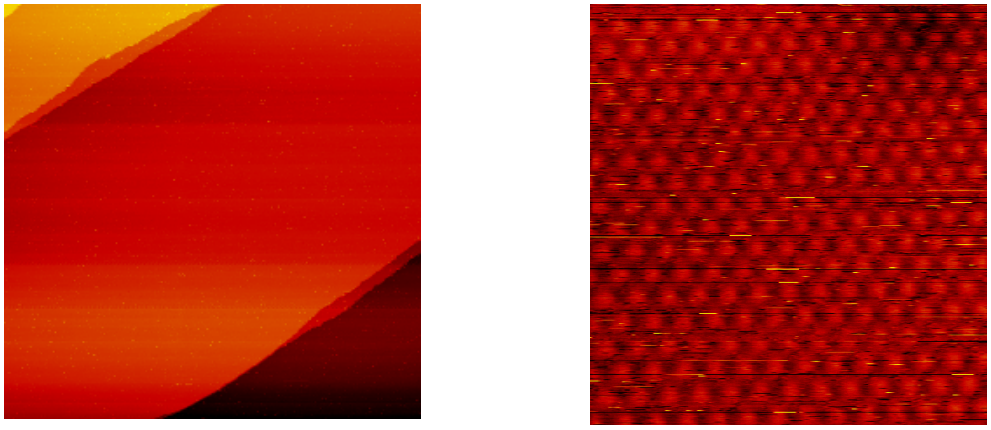

Figure 7. Atomically clean Cu (111) surface a) 500Å x 500 Å, 0.3nA, 2V; b) 33Å x 39Å, 0.2nA, 2V.

The organic molecules used for the experiments were as powder in solid phase. For sublimation onto clean surface they were introduced to the MOKE chamber operated in a pressure of 10^{-8} mbar. The different molecules have different sublimation temperatures and to control this we have used a thermocouple for controlling the glass crucible temperature. In this way we can check the temperature of the powder in the vacuum conditions. Other evaporators were mounted directly into the STM and pre chambers. In case of sublimation of the molecules in the analysis chamber we could evaporate powder directly to the microscope. In this case it is possible to evaporate the molecules at low temperature, depending on the temperature of the STM. Porphyrin and SubPc molecules were evaporated into the MOKE chamber and then transferred to the analysis chamber STM measurements. Oxalic acid molecules were sublimated from the MOKE chamber and also from the STM chamber for having images at low temperature in time of deposition. The evaporator attached to the analysis chamber can be moved towards the microscope to sublimate as close of the STM as possible.

Chapter 2: Self-assembly of porphyrins on Cu(100) and Au(111) surfaces

2.1. Introduction

Porphyrins are large hetrocyclic macrocycle compounds composed of four pyrrole rings linked together by methine bridges (-CH-). The macrocycle has 22 π electrons and follows a Hückel`s rule, i.e. the number of π electrons equals 4n+2 for n integer, which means that some electrons are delocalized over the macrocycle ring.

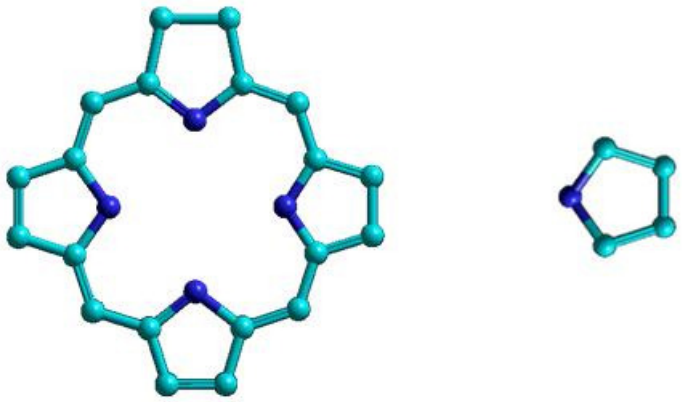

Figure 8. Shows schematically the structure of the macrocycle ring and a pyrrole unit.

Porphyrin can be derivatized in many different ways, for example by attaching new units to the meso position of the ring (position between pyrrole rings). In our studies we will investigate porphyrins with a mesityl group in the meso positions.

A heteroatom can be inserted in the center of the macrocycle ring by deprotonation of the remaining two hydrogens of the pyrrole rings and coordination to the four pyrrole rings in a symmetric manner. In the case of porphyrins the most common heteroatoms are metal ions like Zn, Co, Mg or Fe with an oxidation state +2 or +3. Porphyrins without any ion in the ring are named empty. Porphyrins containing iron play an important role in biological processes, for example they are responsible for the transportation of oxygen in the red blood cells (22) (23). Red blood cells contain hemoglobin, and bonded to its protein chains, it contains the so called heme group, i.e. a porphyrin with an Fe ion at the center. Figure 9 represents the heme group and hemoglobin molecule. The iron atom is linked in the plane to the nitrogens from the pyrrole units and the heme group to the globular protein through the aromatic ring (24).

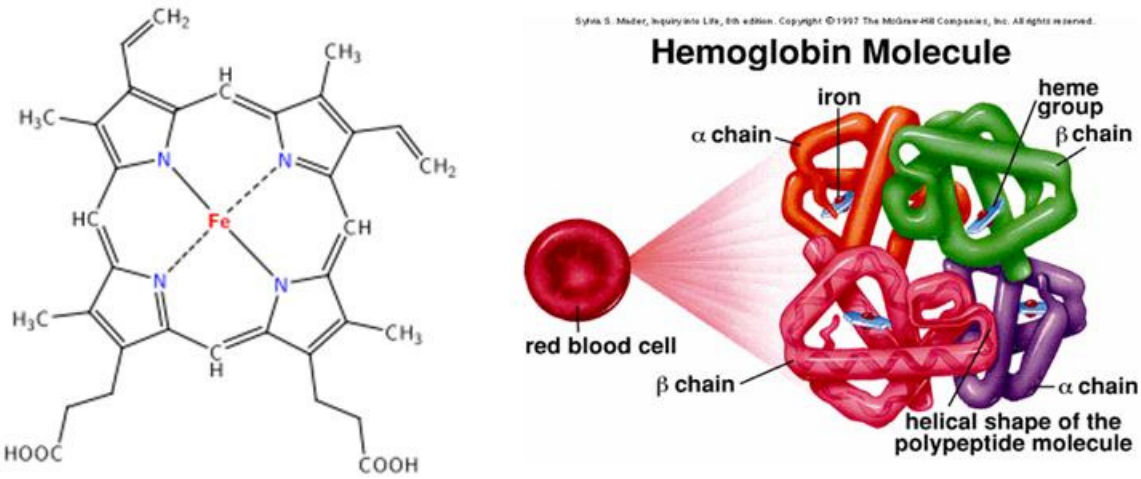

Figure 9. On the left structure oh the heme group with iron linked to the pyrrole units. On the right structure of hemoglobin molecule within protein chains. (24)

2.1.1. Biological functions of porphyrins

Depending on the metal atom at the center, porphyrins can be good electron donors from the electronic point of view (25) (26) (27). They can thus be used in organic solar cells (28) (29) and other devices which require capturing of light, since they are also good dyes and pigments. This ability is related to the other essential biological process in which porphyrins derivatives are involved: photosynthesis. In this case the porphyrin macrocycle ring has a magnesium ion in the center. The derivative of magnesium porphyrin is a chlorin pigment called chlorophyll and occurs in the green parts of the plants and in cyanobacterias. Chlorophyll molecules are similary built as hemoglobin, the chlorin group being surrounded by proteins. Protein complexes containing chlorophyll are called photosystems. Chlorophyll can have chains attached to the macrocycle ring. Figure 10 represents one particular chlorophyll molecule (30) (31).

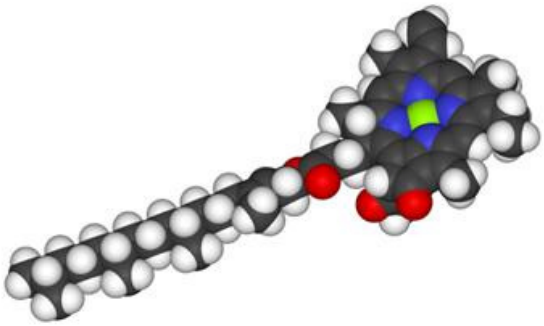

Figure 10. Structure of chlorophyll a the most common in the nature. In the center of the macrocycle ring magnesium ion.

Photosynthesis is a process in which plants capture light energy, convert it into chemical energy and store it as a sugar. Carbon dioxide and water are changed into sugar and in addition oxygen is released as a waste product. The process begins when sun light is absorbed by protein chloroplasts, which are organelles for absorbing a

photon. The absorption of light triggers the release of an electron which is used in the process of reduction and synthesis (32) (33) (34).

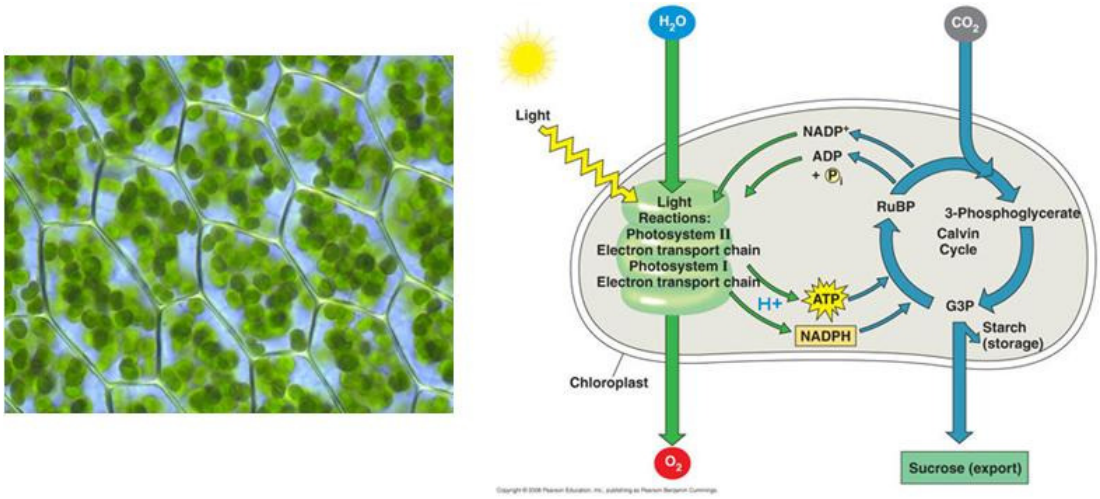

Figure 11. Plant cells with green pigment and scheme of the photosynthesis process.

The first steps in the photosynthesis process are similar to the ones found in manmade photovoltaic devices (PV). For example, in a typical semiconductor p-n junction PV device, a photon excites an electron which will subsequently flow from the p-type area to the n-type area of the semiconductor. (35) The hole is flowing in the other direction, from n type to the p type, as represented in Figure 12.

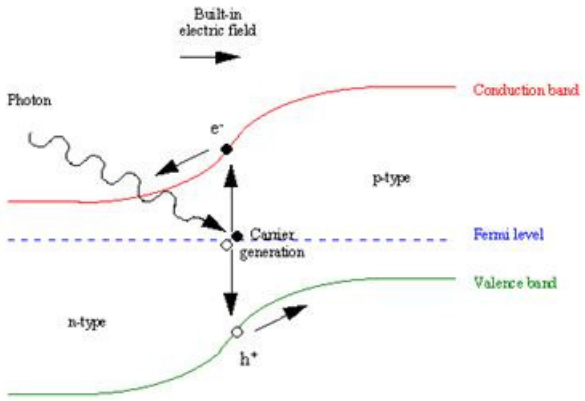

Figure 12. Scheme of manmade photovoltaic system.

The efficiency of photovoltaic devices to convert sun light energy into electricity is about 30% and to improve it, the photosystems (which have efficiencies about 90%) are investigated for possible future transformation from biological inspired systems to technology.

Some of this extra efficiency comes from the existence of specialized structures for the capture of the light. For example purple bacteria uses a nanoscale antenna known as light harvesting complex LHC (antenna complex) (36).This complex is built of

chains of proteins together with chlorophyll a, b and carotenoid molecules. The role of chlorophylls is to absorb the light of different wave spectra, while carotenoids prevent damage of chlorophylls. Antenna complexes capable of harvesting light consist on 200-400 chlorophyll molecules arranged in a specific manner so as to maximize the excitation lifetime thereby enhancing the antenna efficiency for capturing. light (37) (see Figure 13).

Figure 13. Structure of antenna complex in purple bacteria. In green and red bacteriochlorophyll a, b in orange carotenoids, in white proteins. (37)

Other example of light harvesting complex is the one occurring in the green sulfur bacteria. After years of evolution, these bacteria created nanorod like structures which enable them to capture the light in the dim light condition of the sea water where they live. Interestingly it has been shown that those structures can be linked together by self-assembly of the pigment bacterichlorophyll (Bchl) even in non-biological environment.

To build a protein complex, such as the LHC described above, in a man-made light harvesting devices is difficult because their structure and function depend very sensitively on ambient conditions. On the other hand self-assembled structures like the ones described for green bacteria are more likely to be incorporated into devices. The structure of the self-assembled rods of Bchl in green bacteria has been studied experimentally and theoretically. Psencik has proposed a model for the Bchl c molecules in 1D assemblies based on theory calculations. The main bonding motive is the coordination bond between the Mg atom at the chlorin core and the oxygen atoms at the acetyl and hydroxyl moieties. This Mg-O bonding results in two different kinds of stacks α and β, but both of them the distance between the oxygen from the acetyl group to the other hydroxyl side is around 3.3 Å (see Figure 14).

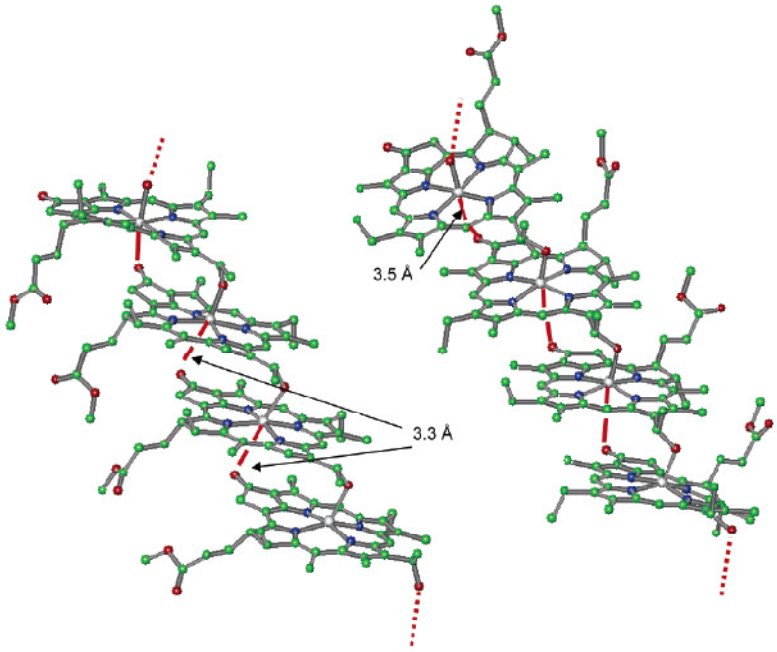

Figure 14. Bchl c molecules linked together by Mg-O bonding. Distance in between two oxygens from acetyl and hydroxyl group around 3,3 Å and 3,5 Å.

The same kind of structures have been found in related synthetic Zn porphyrin molecules. Thus, for the kind of compounds appearing in ref (38) they find the structure displayed in Figure 15. Here, the zinc atom is linked to the oxygen atom of the following molecule from one side, while from the other the oxygen atom from the acetyl group is bonded to the Zn atom of the previous molecule,. The Zn-O distance is around 3,2 Å.

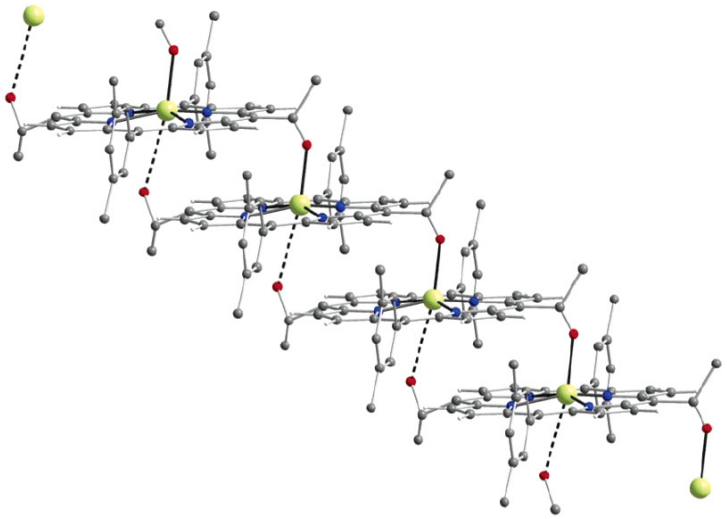

Figure 15. Porphyrin molecules linked together by Zn-O, in green zinc atom, in red an oxygen atom, in blue nitrogen atom and in gray carbon atom.

2.1.2 The TMP and Zn-TMP porphyrins

The purpose of the conducted experiments is to sublimate porphyrin derivative molecules into metallic surfaces that can self-assemble into large nanorod structures similar to those described as for Bchl c molecules. In this case we have chosen Zn porphyrin to self-assemble through Zn atom as was described in the introduction.

Many previous studies of porphyrin on solid surfaces have been recently performed. In the case of tetraarylporphyrin derivatives, the molecular conformation is due to the steric repulsion and π overlapping interactions between the meso aryl groups and the macrocycle ring. Furthermore, the 2D arrangement is the result of the competition between molecule-substrate or molecule-molecule interactions. If the molecule contains strong substituent groups that can form directional bonds, then the porphyrin-porphyrins interaction plays a main role; in the opposite case the preferential interaction is porphyrin-substrate one. In order to explore the possibility of building 1D stacks of porphyrin molecules on solid surfaces we have chosen meso-tetrakis(2,4,6-trimethyl)phenylporphyrin, i.e., an empty porphyrin (TMP) and the same molecule but with a Zn atom inserted into the macrocycle ring (Zn TMP). In this molecule, the rotation of the mesityl groups around the σ bonds is limited, both in solution and in the solid state, due to the presence of the methyl groups in the ortho positions, and this limits the extent of the distortion of the porphyrin core;. Figure 16 shows the gas conformation of the TMP molecule.

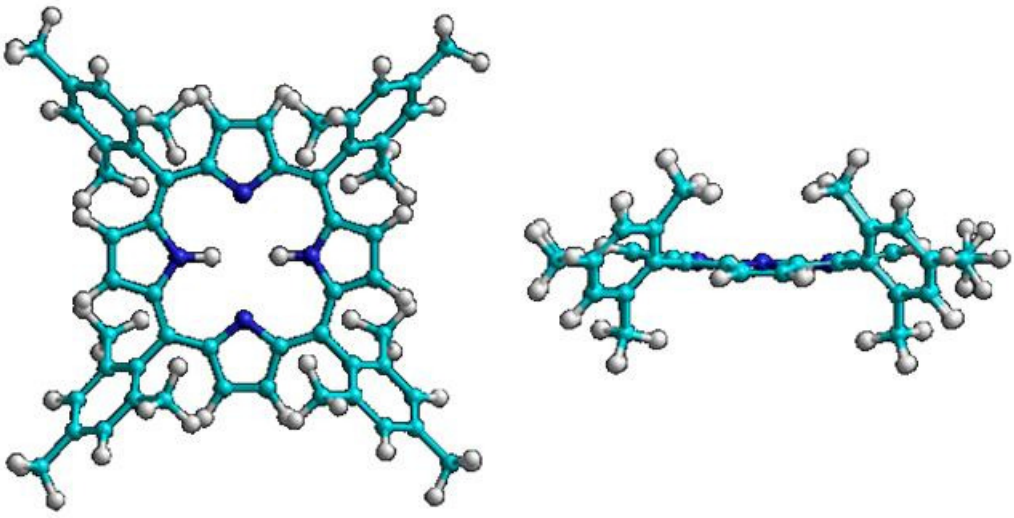

Figure 16. Molecular conformation of TMP molecule using HyperChem calculations.

After theoretically checking the optimal orientation of the mesityl groups, it has been found that the groups should be rotated around the σ bonds at an angle of θ ~ 60º.The twisting of the σ bonds can be done either with C_4 symmetry or with C_{2v} symmetry. Our calculations show that the C_{2v} conformation is slightly more stable. In this way the molecule presents a rectangular shape: the mesityl groups are placed above the macrocycle ring in a rectangle of dimensions 5.0 Å x 8.4 Å and the other four

groups are situated below the plane of the ring. The macrocycle ring is not planar but a little bit bent, the pairs of C atoms forming the outer edge of each pyrrole ring being displaced by ~ 0.3 Å above and below the mean porphyrin plane. Figure 17 displays the molecular energy as a function of the angle θ between porphyrin core and the phenyl rings.

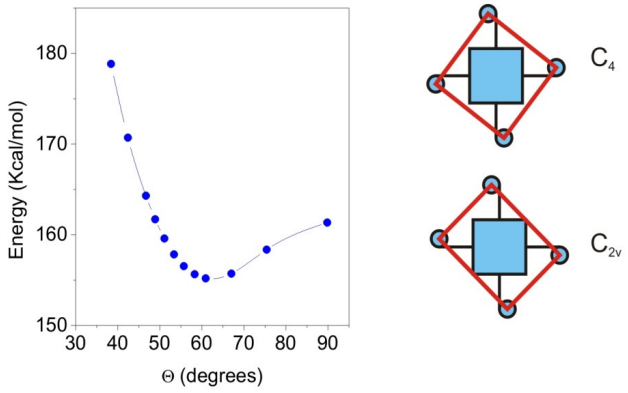

Figure 17. Molecular energy as a function of the θ angle between macrocycle plane and phenyl rings and two schematic representations of the minimum energy conformers for TMP molecules. The large square represents the pophyrin core whereas the blue circles represent the upper methyl groups of rotated mesityl gourps.

2.1.3 Experimental and Theoretical Methods

Both types of porphyrins were synthesized at ICIQ (Institut Català d'Investigació Quimica) in Tarragona by Prof. A. Echavarren group. The Cu(100) surface was prepared by cycles of Ar+ sputtering (500 eV) and annealing at 850 K, until no contamination was present by Scanning Tunneling Microscopy (STM) inspection. Molecules were deposited from the glass crucible (450 K) on the clean copper surface which was held at room temperature . In all the reported cases STM imaging was done at 150 K to prevent molecular diffusion and enhance the stability of the tunneling junction. UPS and XPS experiments were done in a different chamber at the Centro de Astrobiología in the group of Dr. J. A. Martín Gago.

Gas phase calculations described above for isolated TMP molecules were done by molecular mechanics using the MM+ force field of the HYPERCHEM 7.5 molecular modeling package. Density Functional Theory calculations were performed by the group of Prof. Fernando Martín at the Departamento de Química of the Univeridad Autónoma de Madrid using the Gaussian code (39).

2.2. Results for Empty TMP Molecules on Cu(100)

It the following we will discuss the molecular organization and self-assembly of thin films at low and high coverage.

2.2.1 STM results of TMP molecule on Cu(100): Low coverage

At low coverage (0.2 ML or less) decoration of the steps edges by the molecules is observed, implying a high diffusion coefficient at room temperature. In spite of the mobility it was not possible to find large islands on the surface which indicates weak porphyrin-porphyrin interactions (see Figure 18).

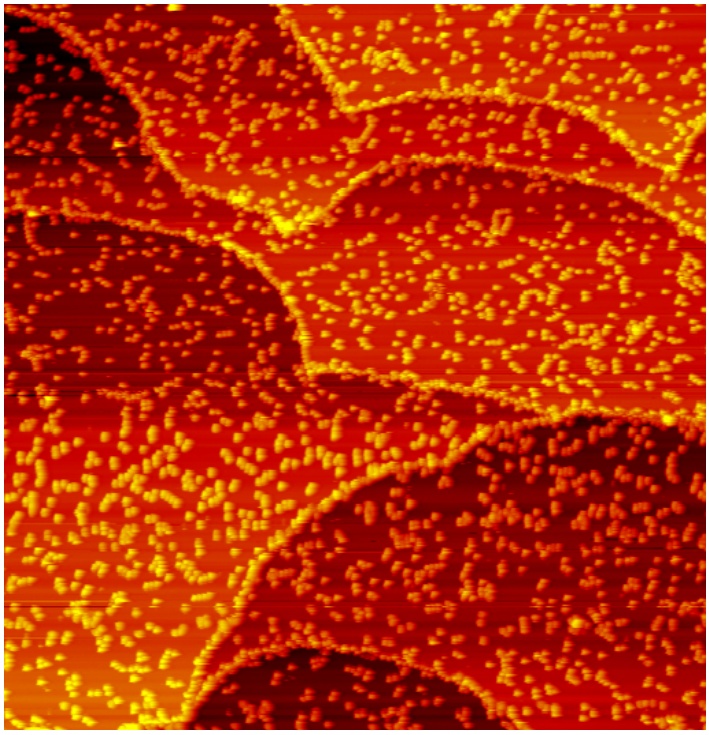

Figure 18. Molecular adsorption at low coverage. Surface displays mainly adsorption at the step edges and small clusters at the terraces. (2260 Å x 2350 Å, 0.5nA, 2.5V)

When we take a closer look to the molecules on the terrace the rectangular symmetry shape of the porphyrins appears (see Figure 19). Each of the molecules is imaged as six lobes, two of them darker and four of them brighter, with three lobes at each side of the main symmetry axis, which is aligned with the high symmetry directions of the Cu(100) surface. The four external lobes (darker) have an apparent height of 2.1 Å, and the internal two (brighter) around 2.3 Å. When we superimpose a structure of the molecule to the STM image we observe that the four darker lobes correspond to the four raised methyl groups and the two brighter lobes are consistent to the pyrrole rings of the porphyrin core situated above the macrocycle ring. The measured size of the rectangular shape of the external methyl groups on the STM images is 4.4 Å x 10.6 Å.

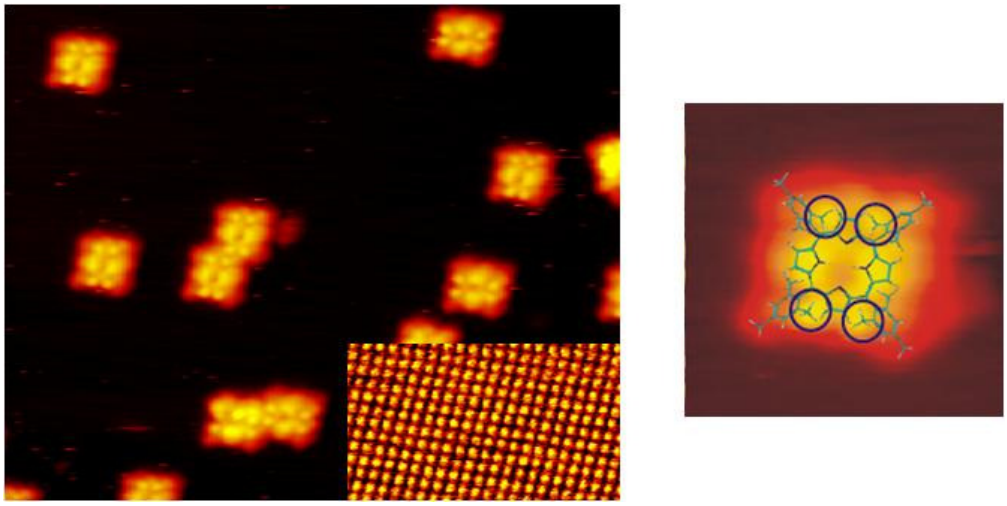

Figure 19. Closer look at the adsorption of the porphyrin. At the right superimposed structure of the molecule at the STM image.(200 Å x 160 Å, 0.7A, 2.5V).

2.2.2 TMP molecule on Cu(100) surface at high coverage

When we increase the amount of evaporated molecules we observe that large islands start to growth at the surface. Figure 20 displays STM images for coverages of 0.45 and 0.65 ML of TMP molecules on the copper surface. Large ordered islands are covering almost the whole substrate after further dosing.

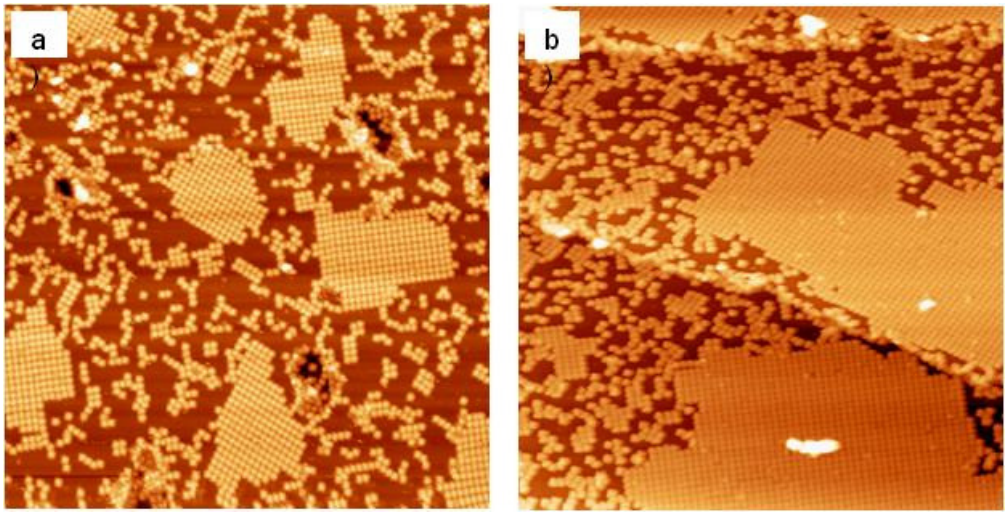

Figure 20. Large ordered islands of TMP on Cu(100) surface.(1180 Å x 1320 Å); a) 0.45 ML, I =0.71 nA; V = -3.0 V; b) 0.65 ML, I = 0.32 nA, V = -3.0 V

Taking a closer look to the islands we are able to distinguish two different orientational domains with an approximately square unit cell of 16.4 ± 1 Å long in both cases, but with their main axis rotated ~ 53º ± 5º with respect to each other. The structure within these domains are consistent with commensurate networks with an epitaxial relationship given by

$$\begin{pmatrix} b1 \\ b2 \end{pmatrix} = \begin{pmatrix} 6 & 2 \\ -2 & 6 \end{pmatrix} \begin{pmatrix} a1 \\ a2 \end{pmatrix} \qquad \begin{pmatrix} b1 \\ b2 \end{pmatrix} = \begin{pmatrix} 6 & -2 \\ 2 & 6 \end{pmatrix} \begin{pmatrix} a1 \\ a2 \end{pmatrix}$$

where b1 and b2 are the unit cell vectors of the molecular overlayer and a1 and a2 are the primitive vectors of the Cu(100) surface (see Figure 21).

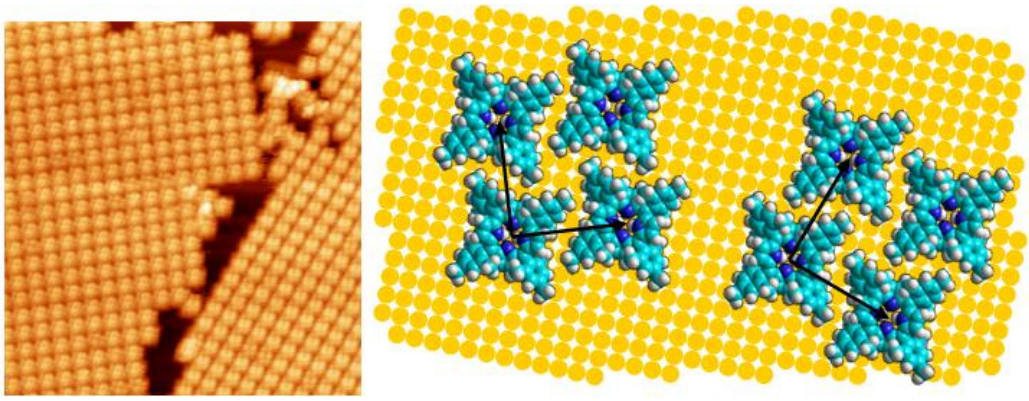

Figure 21. Two different domains of TMP molecule. (340Å x 350Å I = 0.32 nA; V = -3.0 V).

The structure is close-packed, indicating weak vdW intermolecular interactions between neighboring molecule, in good agreement with the observation of lack of aggregation for lower coverages.In general, such vdW interactions lead to a close-packing of cross-shaped molecules. As was described before, the close-packing of achiral molecules might be chiral (4)This is precisely the case of our porphyrin molecules, the two domains found being mirror symmetric and thus enantiomeric to each other.

2.2.3 UPS measurements on thin films of porphyrins

We have measured the UPS spectra of a different thickness films of TMP on Cu(100) (see Figure 22).

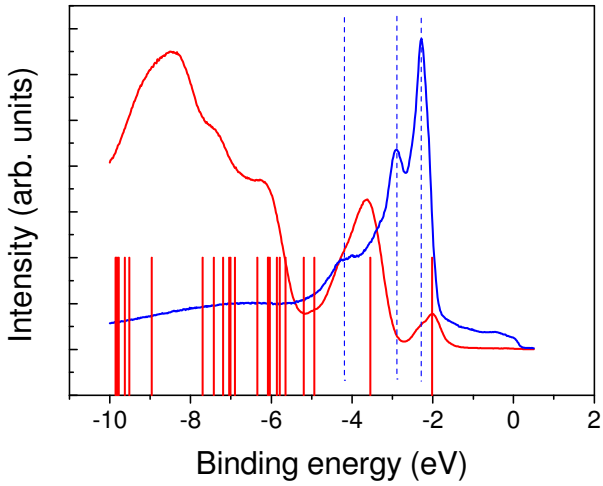

Figure 22. Photoemission spectra (red line) of a thick TMP film deposited on Cu(100).

The blue line shows the clean copper spectra and the red line the spectra of a thick film of TMP on Cu(100). It can be distinguished that the HOMO level is at -2.1 eV below the Fermi level. The vertical lines are the energy values of the molecular orbitals (with a rigid shift of 1.5eV) calculated *ab initio* with the HYPERCHEM software package which are seen to agree with the experimental spectra. The reason for such a shift in the energy levels is not entirely clear, as it does not correspond to the well known energy level alignment rules at interfaces.

2.3. Adsorption of Zn TMP molecules onto Cu(100) and Au(111) surfaces investigated by STM and XPS techniques.

In this paragraph we will focus on the investigation of metal porphyrin with a Zn atom inserted. It will be shown by a combination of different techniques that long 1D coordination polymers of porphyrins, similar to the rods of Bchl c in the green bacteria, are obtained on different substrates.

2.3.1 STM studies after deposition of Zn TMP molecule onto Cu(100) surface

In contrast to the case of empty TMP, where island growth is found for high enough coverages, for the metallated Zn-TMP we observe the formation of one dimensional rods trough the terraces with lengths of about 0.1 – 0.2 μm. The rods show an ordered pattern of protrusions that will be discussed later on (see Figure 23). STM imagles also reveal the existence of disordered areas of molecules from which the tubes grow. In addition some isolated molecules are found on the step edges and terraces. Both the rods and the disordered islands are rather high (0.9 nm), which seems to suggest a non planar adsorption of the Zn-TMP molecules on the surface (it might also suggest multilayer growth, but as we will see later the former option seems to be the right one).

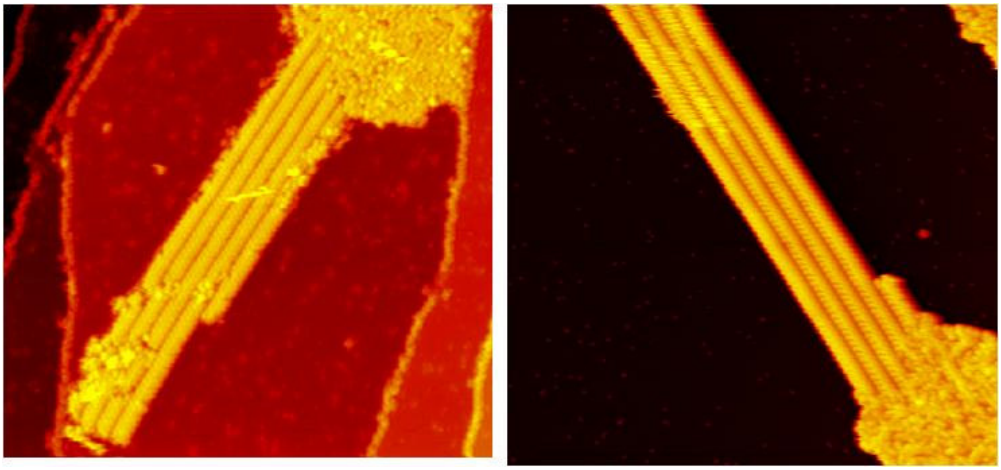

Figure 23. High resolution STM images of o Zn TMP molecule on Cu(100) surface. a 9840 Å x 9840Å 0.5nA -3.4V b 1045Å x 1260Å 0.5nA -2.1V

2.3.2 STM studies after deposition of oxygenated Zn TMP molecule onto Au(111) surface

The growth behavior of these molecules seems to be very severely affected by the presence of the metal ion. Such large differences require further experiments to be understood. To understand the role of the substrate on the formation of the rods we have changed the substrate to a less reactive surface as Au(111). Even though we have changed the chemical nature and the crystalline arrangement of the surface atoms, after deposition onto clean Au(111) surface we could clearly observe 1 D rods of molecules again (See Figure 24). The formation of the tubes seems thus to be independent from the surface. We have therefore a clear argument to say that the driving force in the formation and self-assembly of the rods is the intermolecular interactions.

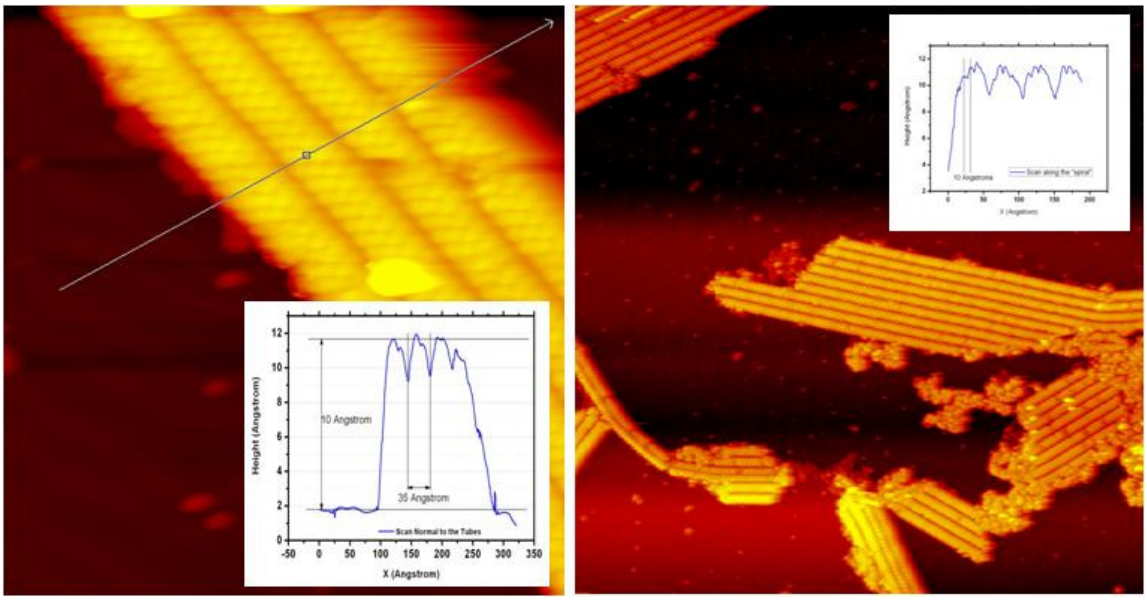

Figure 24. This figure display a high and width of the nanorods. 1570 Å x 1890 Å 0.5nA -1.9V, 314Å x 378 Å 0.1nA -2.1V

High-resolution images of the porphyrin nanorods reveal an ordered array of protrusions with a typical size of about 0.6 nm, i.e. significantly smaller that the size of a single molecule, and a typical height of about 0.9 nm (See Figure 24). A planar adsorption geometry, in which the porphyrin ring is placed parallel to the surface, seems to be inconsistent with our observations of the nanorods.

Furthermore, we could observe additional adsorption on top of the tubes, as seen on Figure 25. The line scan shows that adsorbed molecules are higher than the top of the tubes by around 5.25 Å.

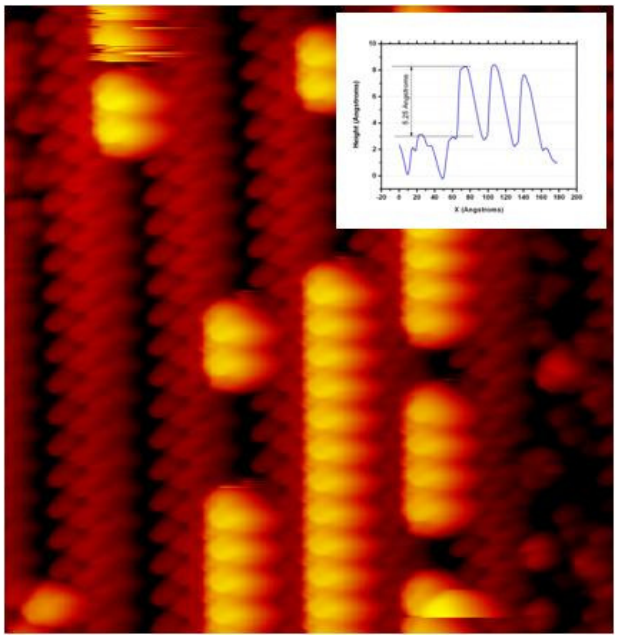

Figure 25. Additional adsorption on the top of the tubes. 209Å x 252Å 0.2nA -2.9V

2.3.3 STM measurements after annealing Zn TMP molecule on Cu(100) surface

The rod morphology is however not the thermodynamically stable state for the molecules on the surface. After heating up to 525 K rods cannot be found on the STM images any longer. Instead, 2D arrays of much lower protrusions height with square shape cover all of the surface. Their size corresponds to a planar adsorption geometry (see Figure 26). Similar images have been previously reported by Prof. Raval's group in Liverpool, and they interpreted the short TMP-TMP distance as indicating a covalent bond between the molecules. (40)

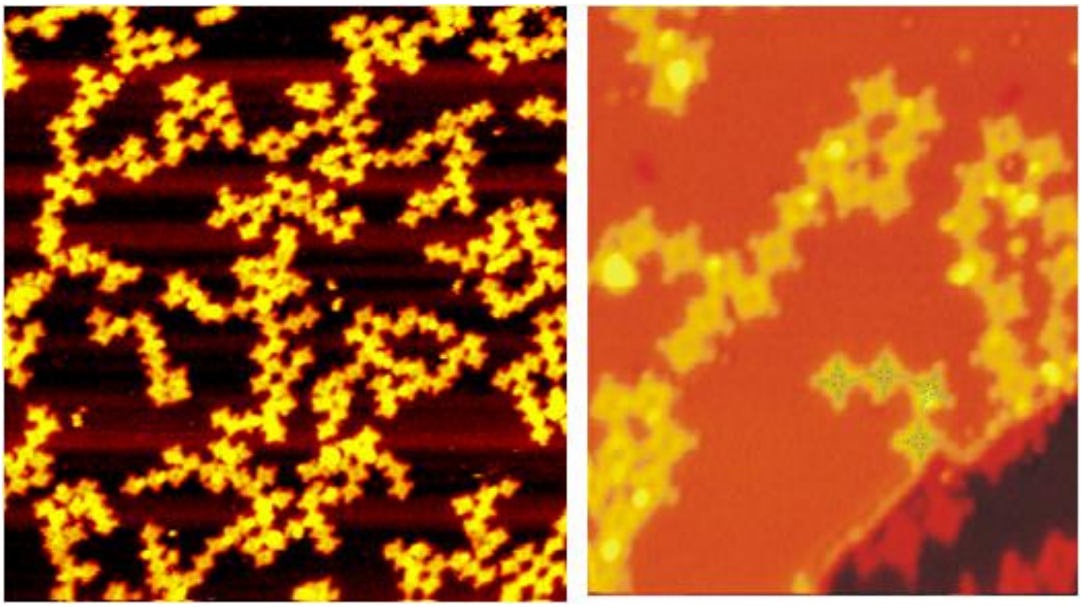

Figure 26. STM images after desorption of oxygen from the molecule after annealing till 525 K. a) 522Å x 630Å, 0.62nA, -1.68V; b) 209Å x 252Å, 0.7nA -2.1V.

2.3.4 XPS measurements of TMP and Zn TMP molecules

In order to investigate the chemistry involved in tube formation and tube disassembly we have performed XPS measurements. Apart from the expected C 1s, N 1s and Zn 2p core level peaks, at about 284.8 eV, 398.3 eV and 1021 eV binding energies respectively, we clearly detect an oxygen signal (O1s at 531.4 eV binding energy) for the sample deposited at RT before annealing. Oxygen is not present at the molecule by itself, and it is not found for the empty TMP molecules, which suggest that oxygen containing molecules might be coordinating to the central Zn atom of the molecule (See figure 27). After annealing the oxygenated Zn TMP molecule the XPS spectra shows that the oxygen peak disappears, corresponding to the change from the rod morphology to the flat adsorption geometry. This result indicates that without oxygen nanotubes cannot self-assemble. Annealing, however leaves the other peaks mostly unchanged, which proves that the Zn atoms keep coordinated at the center of the Zn-TMP molecules. This is also in agreement with the existence of a single peak for the N 1s level after annealing. Empty TMP porphyrins show a double peak arising from the protonated and deprotonated pyrrole nitrogens in TMP..

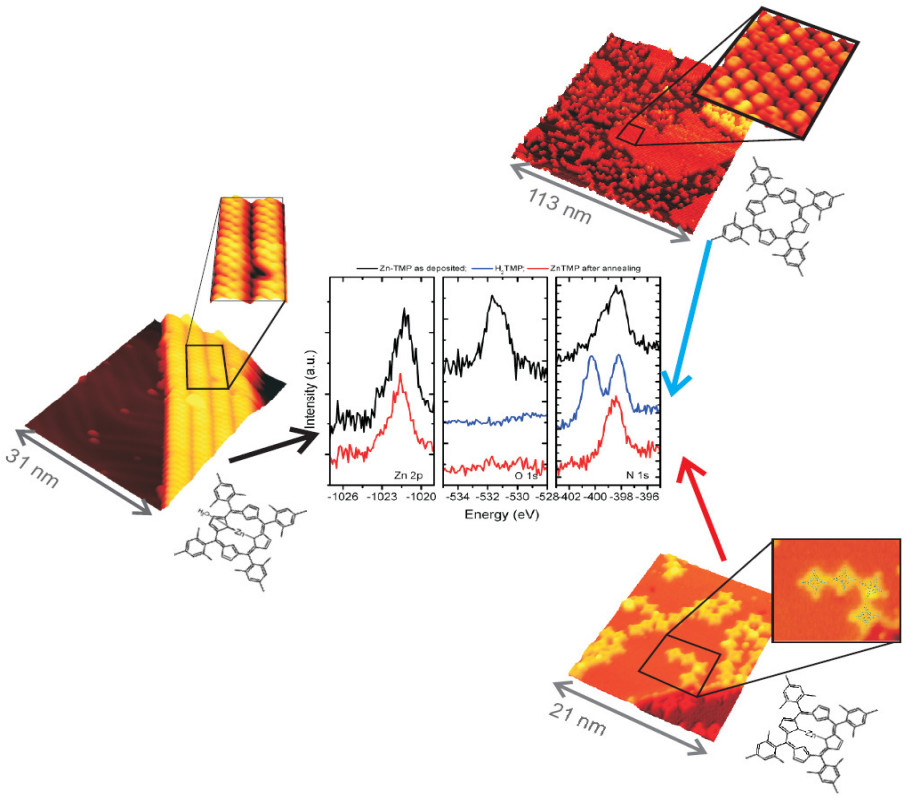

Figure 27. STM and XPS results of TMP and oxygenated Zn TMP molecules. Black curves correspond to tube morphology of the Zn-TMP molecules as deposited, the red curves to the flat lying Zn-TMP molecules after annealing, and the blue curves correspond to the spectra of empty TMP molecules.

Taking into account all the information we suggest that Zn pophyrin molecular stacks are linked together by a coordination bond between Zn atom and an oxygen

containing axial ligand that bridges neighboring Zn-TMP molecules. The oxygen containing molecule could be water or acetate used during the synthesis process. Figure 28 displays the structure of Zn TMP molecule and the same molecule with a linked water to the Zn atom. (41)

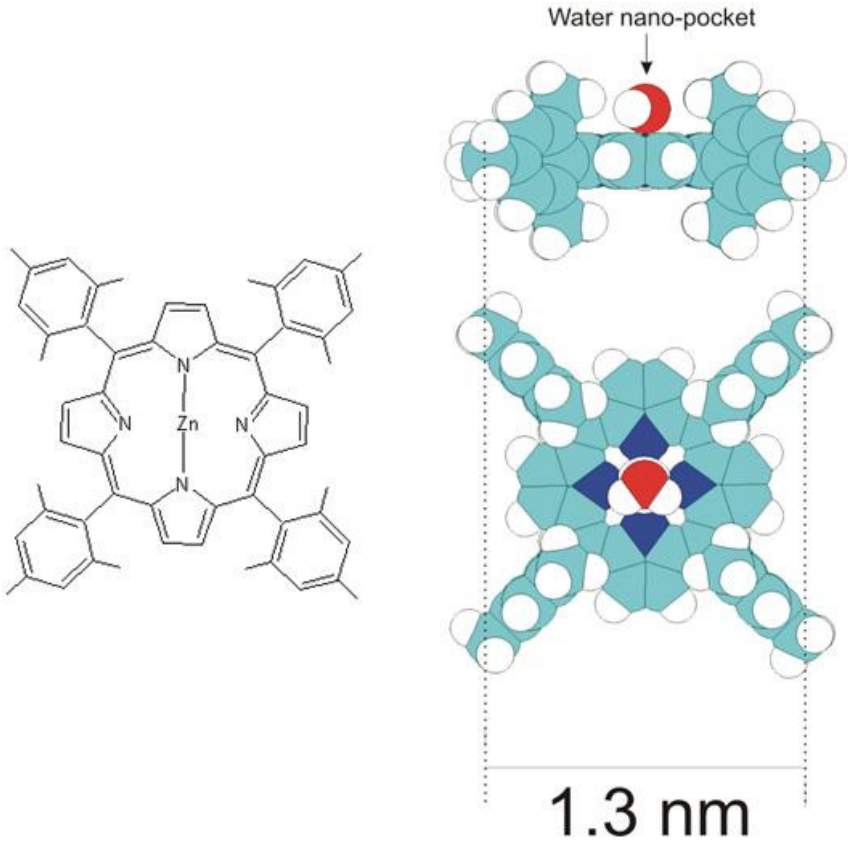

Figure 28. Structure of metaleted porphyrin and Zn TMP molecule with water coordinated to the Zn atom.

The structure of this molecule seems to be particularly well-suited for the formation of such coordination polymers on the surface. The oxygen from the water or acetate ligands is the only available atom to link two Zn atoms at the core of neighboring porphyrins. Mesityl groups create some kind of a pocket which prevents the ligands from reacting with the surface during the adsorption process onto the metal substrate. On the other hand, self-complementarity in the molecular shape (by a 45º rotation with respect to the C_4 symmetry axis perpendicular to the porphyrin plane) enables contact between the oxygen atom and the Zn atoms of oxygenated ZnTMP molecules.

2.3.5 DFT calculations of oxygenated Zn TMP molecule

In order to investigate the stability of oxygen containing ligands in our Zn-TMP we have performed theoretical Density Functional Theory for two Zn-TMP molecules linked together by a water molecule. A stable minimum energy state was found when the two molecules are rotated 45º with respect to their C_4 axis, in such a way that the lone pairs in the oxygen atom of the ligand can interact with both Zn centres (see Figure

29). Thus, the ZnTMP molecules are linked to each other through coordination with bridging ligands. Similar structures are known to occur in solution for a variety of metalloporphyrins and phthalocyanines with different ligands acting as linkers (42) (43) (44) (45) (46).

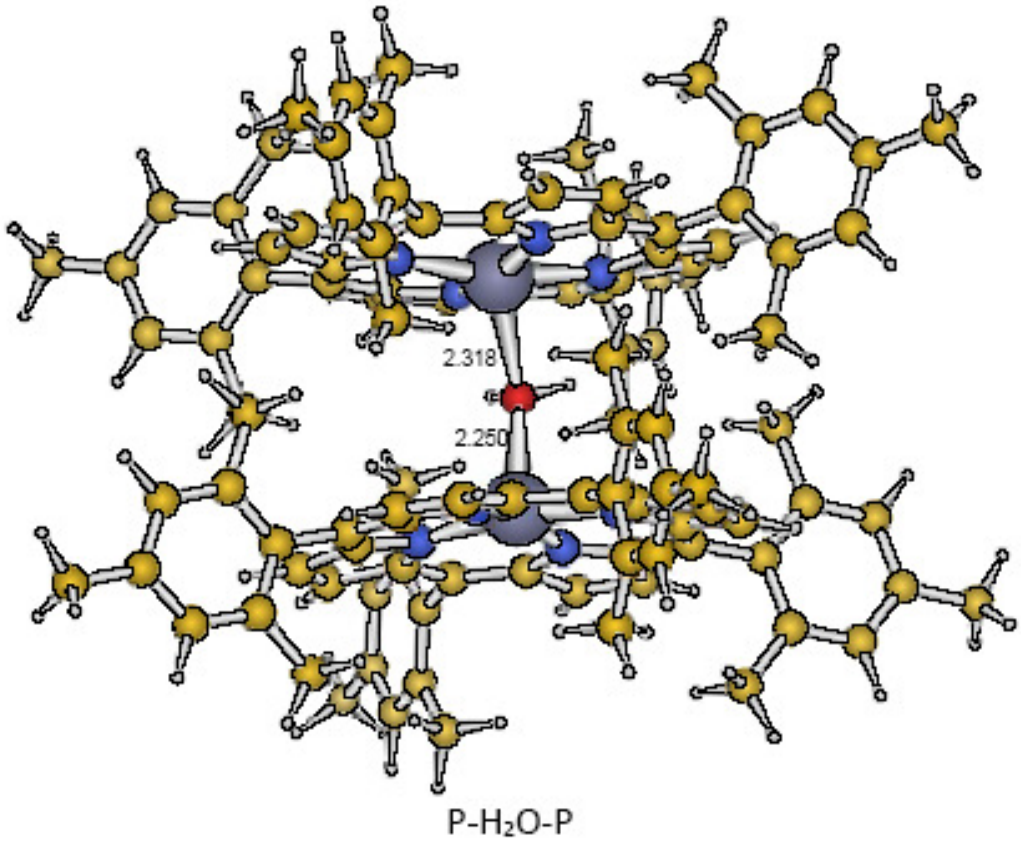

Figure 29. Porphyrin molecules linked together by an oxygen atom, in this case from water molecule. The stabilization energy provided by the coordination bond to the formation of the coordination polymer is calculated to be about 0.6 eV/monomer

2.3.6 A Structural Model for the Tubes

Based upon the theoretical models mentioned above we propose the following structure for the observed nanorods. Each porphyrin molecule is rotated by 45º around its C_4 axis with respect to its neighbors. The ZnTMP molecules are linked to each other through coordination with oxygen atom. An STM image of such a tube can be expected to show bright protrusions at the position of the topmost mesityl groups, and lighter protrusions for the remaining mesityl groups pointing towards the top of the tube (see Figure 30).

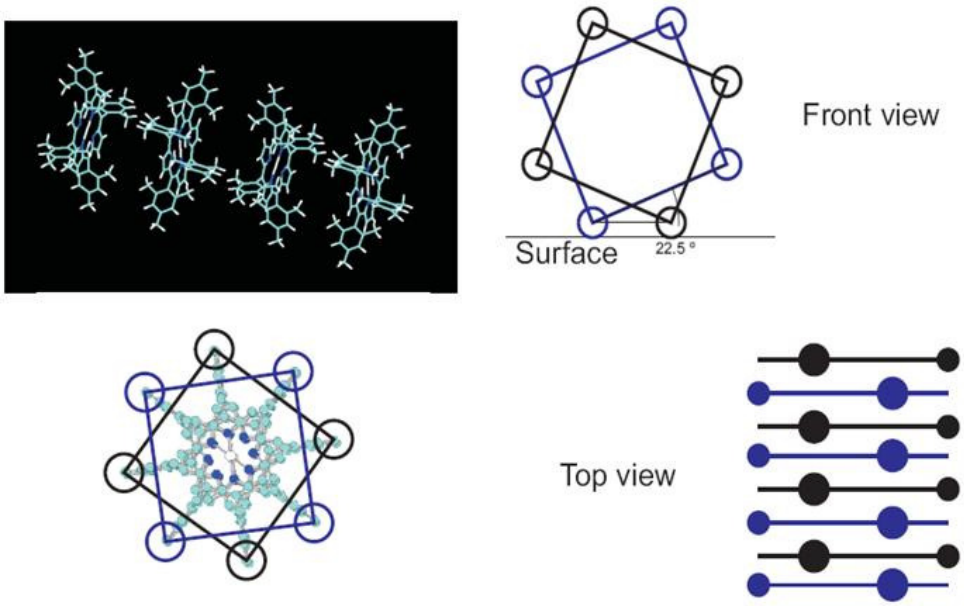

Figure 30. . Scheme of the tubes in respect to the STM and DFT data.

This model predicts the spiral shape observed in the STM images. A look into Figure 31 reveals that the agreement between the experimental images and the model is very good.

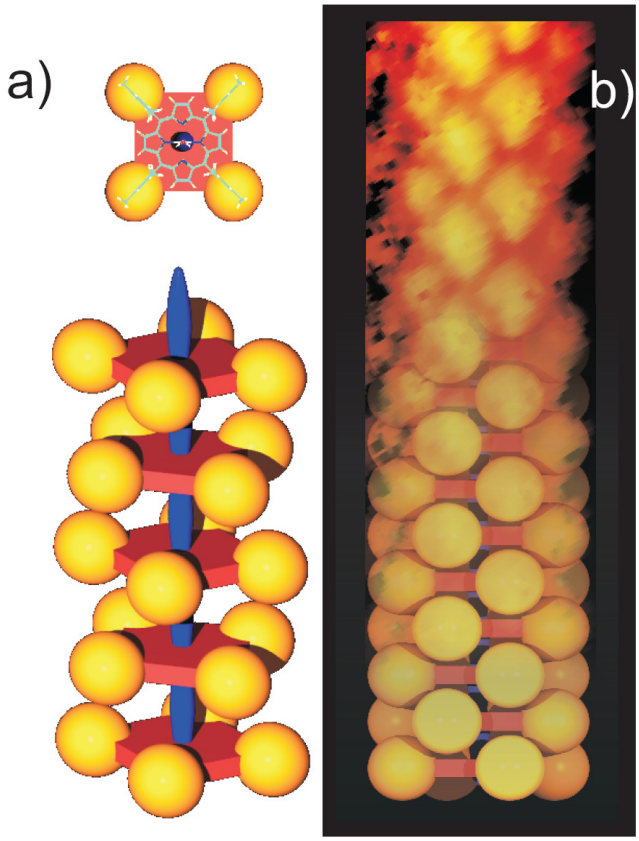

Figure 31. Comparison between the structural model for the tubes and STM images.

2.4Conclusions

We have performed a study of both empty TMP and oxygenated Zn-TMP molecules on different metal surfaces. From a combination of techniques as STM, UPS, XPS and DFT we can conclude that:

- For small coverage TMP molecules adsorb on the Cu(100) surface in a planar geometry, but we could observe some bending of the porphyrin core with respect to the surface. Molecules have a rectangular shape with bright and dark protrusions corresponding to the bend conformation of the mesityl groups at the meso position.
- For higher coverage TMP molecules form 2D islands with two different chiral domains with respect to surface and molecule
- Oxygenated Zn TMP molecule adsorb on the Cu(100) and Au(111) surface as a large one dimensional rods linked together by an oxygen containing ligand There is ample evidence in the literature that this kind of aggregation leads to a red-shift and a broadening in the light absorption spectra of the molecular dyes, both highly desirable properties for sunlight harvesting devices (47) (48)

Chapter 3: Subphthalocyanines on Cu(111): Epitaxial Growth of Organic Nanocrystals with Antiferroelectric Stacking

In this chapter we will focus on another example of a large macrocycle molecule which can host a metallic atom coordinated at the center and can self-assemble through .molecular interactions when deposited on a solid surface.

3.1 Introduction

Controlling the formation of nanosized organic particles of well-defined size and shape is one of the challenges facing modern chemistry. The optical properties of such organic nanostructures, similar to the case of their inorganic counterparts (49) (50) (51), are extraordinary and very different from the properties found for the same materials in bulk form (52) (53). For example, organic nanoparticles have been shown to have size-dependent absorption and fluorescence bands (52) or single photon emission. (53).

However, a detailed understanding of these effects is hindered by the difficulty in the synthesis of these organic nanocrystals. A possibility that remains mostly unexplored is the synthesis of such nanocrystals on solid surfaces. In the same way in which crystalline inorganic nanodots can be epitaxially grown on suitable substrates under conditions in which 3D Volmer-Weber growth takes place (54), an organic system could in principle be devised such that the growth of crystalline 3D islands sets in before the completion of the first monolayer. In practice, however, for organic adsorbates deposited on inorganic substrates intermolecular interactions are much weaker than molecule-substarte interactions, thus promoting a layer-by-layer mode, and preventing the fabrication of isolated 3D nanocrystals (3) (55).

In this chapter we show how, upon deposition of cone-shaped, high dipole moment, subphthalocyanine molecules on Cu(111), isolated triangular nanocrystallites up to 3 ML high appear on the surface before the completion of the first monolayer, i.e. 3D growth is promoted versus layer-by-layer growth.

3.1.1 Subphthalocyanines

Among the large variety of metallo-macrocycle which can allow us to grow organic nano-materials, phthalocyanines play a quite important role. They have interesting optical and physicochemical properties. Phthalocyanines are planar aromatic macrocycles composed of four isoindole units linked together through nitrogen atoms (see Figure 32). Their 42 π electrons are distributed over 32 carbon and 8 nitrogen atoms, but the electronic delocalization mainly takes place on the inner ring which is made of 16 atoms and 18π electrons, the outer benzene rings maintaining their electronic structure.

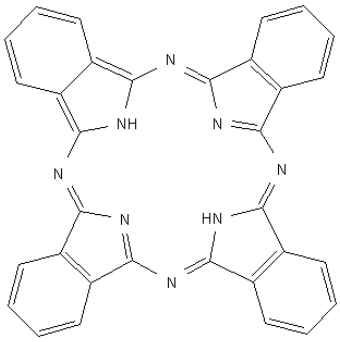

Figure 32. Structure of an empty phthalocyanine

The basic structure of the macrocycle may be modified giving rise to phthalocyanine analogs such as subphthalocyanines (SubPc, from now on) (56) (57) (58), with only three isoindole units coordinated to a central boron atom (see Figure 33.). As a result of this modification, SubPc display a cone-shaped structure, which does not prevent them from being aromatic molecules. As in the case of the phthalocynines, the aromatic nature of the macrocycle is essentially located in the inner ring, where 14 π electrons are delocalized over 6 carbon and 6 nitrogen atoms, the peripheral benzene rings mostly retaining their electronic structure. An axial ligand (Cl, F) covalently attached to the boron atom confers a strong dipolar character to the overall molecule mostly oriented along the C_3 symmetry axis.

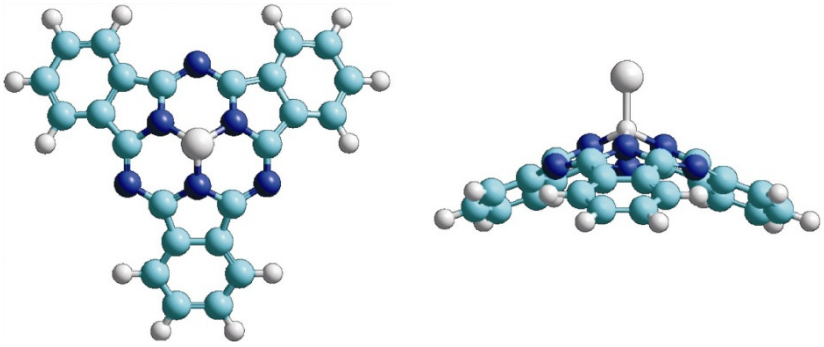

Figure 33. Structure of a SubPc-Cl molecule..

Subphthalocyanines show very attractive photophysical and electrochemical properties and have found applications in nonlinear optics (59), OLEDs (60), and other photovoltaic devices and multicomponent donor-acceptor systems (61).

In this chapter we will show how these properties leads to an unusual growth mode for SubPc-Cl molecules deposited on the Cu(111) surface.

3.1.2 Classification of the growth modes

We will briefly review the main aspects of thin film growth. In figure 34 we can find a schematic drawing of the main atomistic processes involved in thin film growth: adsorption, desorption, intra layer diffusion, inter layer diffusion, nucleation and finally the growth of islands.

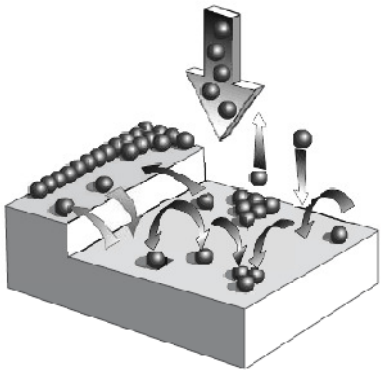

Figure 34. Schematic drawing of the main surface processes involved in thin film grow: adsorption, desorption, intra-layer diffusion, inter-layer diffusion-steps, nucleation and growth of islands.

In the thermodynamic limit the morphology of the resulting film is determined by a delicate balance between adsorbate-adsorbate and adsorbate–substrate interactions. Traditionally, the different growth modes have been phenomenologically clasified as follows (Figure 35):

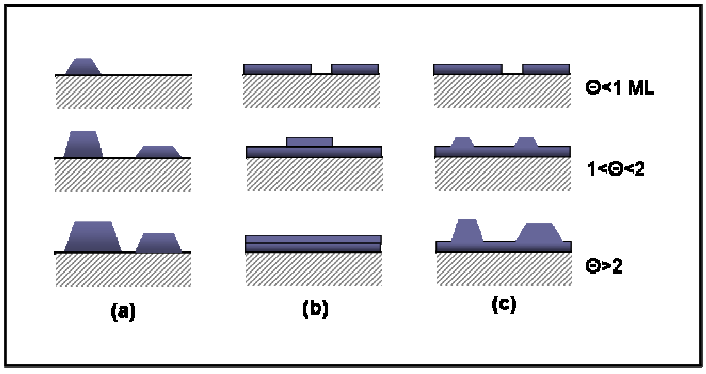

Figure 35. The different growth modes on surfaces. a) islands growth, b) layer by layer growth, and c) island layer growth.

a) Volmer-Weber growth (VM) or island growth(Figure. 35 a)

In the Volmer-Weber growth mode, the interaction between adsorbate atoms is higher than the adsorbate-substrate interaction. As a result, adsorbate 3D islands are created on the surface.

b) Frank van der Merwe (FM) or layer-by-layer growth (Figure 35 b)

In this case the interaction between substrate and adsorbate is much stronger than between adsorbate atoms, which leads to smooth. In the perfect layer-by-layer limit, to create a each new layer the previous one has to be completed.

c) Stranski-Krastanow growth (SK) or layer plus island growth-(Figure. 35 c)

In the Stranski – Krastanow growth mode the first layer wet the surface completely but subsequent layers do not. so 3D island starts to growth on top of the full layers.

In principle, the classification of the growth modes described above can be applied both to inorganic and organic compounds. Nevertheless, the growth of organic compounds can be much more complicated due to the existence of new phenomena such as new degrees of freedom, differences in structure and strength of the interaction potential and the larger size of the molecules.

- Degrees of freedom

The existence of a larger number of degrees of freedom for molecular adsorbates is the most fundamental characteristic in organic thin film growth. For example, orientational degrees of freedom can lead to qualitatively phenomena, such as a change the orientation of the organic molecule during the film growth.

- Interaction potential

The molecule-substrate interactions and molecule-molecule interactions are different from the inorganic adsorbents at surface, with interaction such as hydrogen-bonding or. van der Waals forces that can play a significant role.

- Size of the molecules

The size of adsorbed organic molecules is larger than in the case of inorganic compounds. Thus the apparent corrugation of the surface potential is weaker and we can obtain different domains at the surface more easily than in the inorganic case.

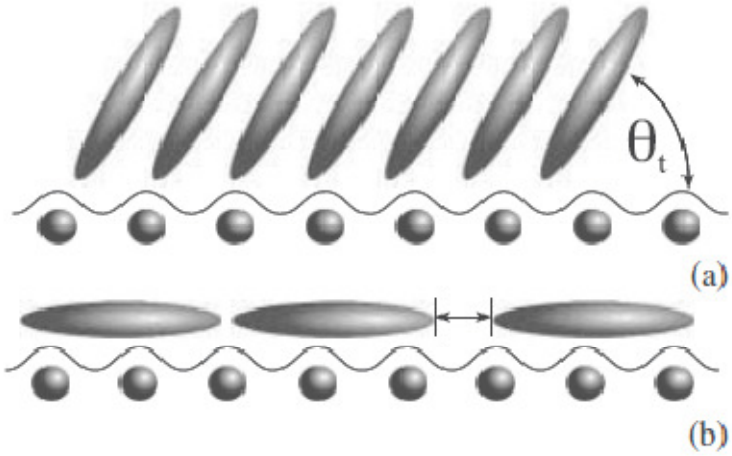

Figure 36.Orientational degrees of freedom in the the growth of organic compounds can lead to new phenomena non-present in inorganic thin film growth.

From the previous discussion it is obvious that in order for organic molecules to grow in the VW mode, the interaction between substrate and molecule must be much weaker, than molecule – molecule interaction. A particular way to achieve this is to use non planar molecules (which decreasies the molecule – substrate interaction) with a high dipole moment (which may increase molecule – molecule interaction).

3.1.3 Previous reported STM studies on SubPc molecules

STM studies of SubPc adsorbtion and self-assembly on different metallic surfaces has been reported. Up to now, the growth of SubPc-Cl on metal surface like Ag(111) (62) (63), Au(111) (64) and Cu(001) (65), and on the semi-conductor reconstructed (7x7) silicon surface (66) has been reported.

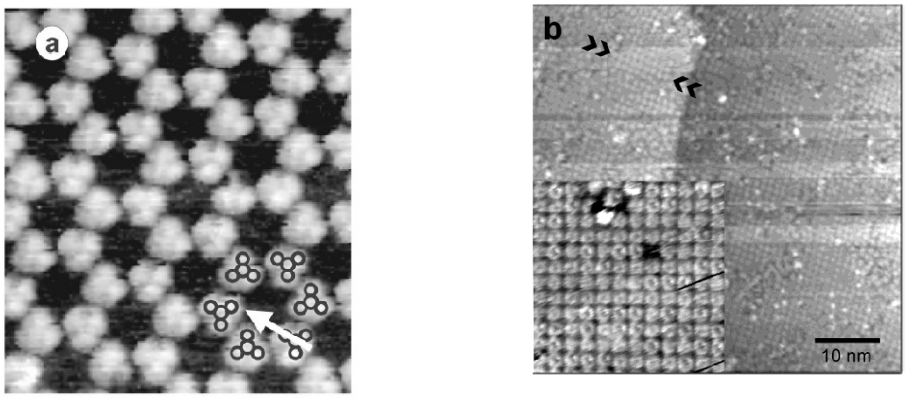

Figure 37. STM images of SubPc molecules on Ag (111) and Cu (100) surfaces.

Ordered honeycomb and hexagonal closed packed (hcp) patterns were found after depositing12HSubPcCl on Ag(111) ($d_{intermolecular} \approx 1.89$ nm); a rectangular pattern was found on Au(111) ($d_{intermolecular} \approx 1.2$ nm) and a square pattern on Cu(100) ($d_{intermolecular} \approx 1.3$ nm). The molecule 12HSubPcCl may adsorb on the surface with the chlorine atom facing the metal surface (Cl-down), like in Ag(111), or with the phenyl groups in contact with the metal substrate (Cl-up), like in Au(111). In addition, a stochastic switching between Cl-up and Cl-down configuration has been reported on Cu(001)., while STM measurement .

3.1.4 Experimental and Theoretical Methods

Subphthalocyanine molecules were synthesized according to a previously reported method at the Autonoma University of Madrid in the Organic Chemical Department by the group of Prof. Tomás Torres (67)The Cu(111) surface was prepared by cycles of Ar+ sputtering (500 eV) and annealing at 850 K, until no contamination was present by Scanning Tunneling Microscopy (STM) inspection. SubPc was deposited in situ by thermal sublimation (420 K) on the clean copper surface which was held at room temperature. STM measurements were performed at 150 K.

Simulated STM images were obtained by simple Extended Hückel quantum mechanical calculations of the molecular electronic structure and conformation in the gas phase with the HYPERCHEM package. The images were subsequently obtained by adding molecular orbitals up to an energy level determined by the applied bias voltage. This approach has been shown to yield images that qualitatively reproduce the experimental ones for small molecular species (68) and macrocycle porphyrins (69) adsorbed on metal surfaces

Finally, the stability of bilayer islands as a function of interlayer separation and relative orientation were also estimated by Molecular Mechanics with the MM+ Force Field, which is known to include dispersive interactions such as van der Waals, which are crucial for the formation of the observed structures and are badly described, or not described at all, by other more sophisticated DFT-type calculations.

3.2 Results

As discussed above, the magnitude of the dipole moment may play a major role in the growth of the SubPc films. It is then important to have some way to control this value. This can be done synthetically by changing the axial ligand and/or functionalizing the molecular peripheral phenyl rings. In particular, we have focused on the evaporation of three kind of polar sub-phthalocyanines: i) the chloro[sub-phthalocyaninanto]boron(III) (12HSubPcCl); the fluor[sub-phthalocyaninato]boron(III) (12HSubPcF); and the 12 fluorated chloro ([sub-phthalocyaninanto]boron(III) (12FSubPcCl)(see Figure 38).

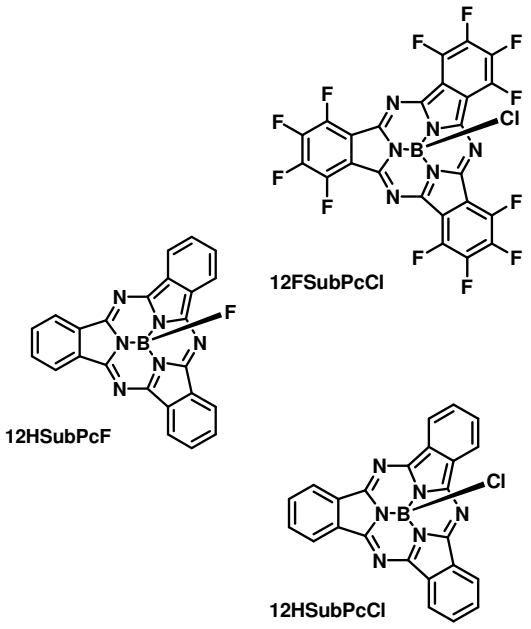

Molecule	Dipole moment (D)
12HSubPcCl	4.6
12HSubPcF	4.0
12FSubPcCl	2.2

Figure 38. Structure of the different SubPc molecules used in the experiments and their calculated dipole moments.

3.2.1 12HSubPcCl on Cu(111).

In order to find out the adsorption configuration of the molecule on the Cu(111) surface we have performed simple theoretical calculations of the apparent shape of the molecule when viewed from above and from below. The results are shown in Figure 39. Both for positive and negative voltage the apparent shape is a trefoil one for the Cl-down configuration and a single bright spot for the Cl-up configuration.

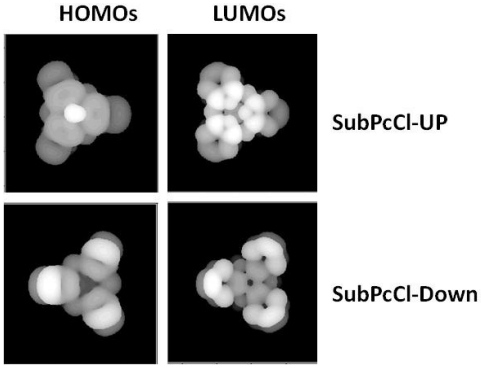

Figure 39: LUMO and HOMO states of two different species adsorptions of the SubPcCl molecule.

When we evaporate a very small amount of 12HSubPcCl we are not able to properly image any molecule. Despite the low temperature during scanning, the inability to see any molecule at very low coverage suggests that a very low diffusion barrier, probably as a consequence of a weak molecule-substrate interaction. After increasing the coverage, we are able to distinguish disordered groups of molecules (see Figure 40a), even with intramolecular resolution, which allows us to distinguish two different species: a bright round spot one and a trefoil-shaped darker one. According to the calculations previously shown, we identify the first species with Cl-up SubPc molecules and the second one with Cl-down SubPc molecules.

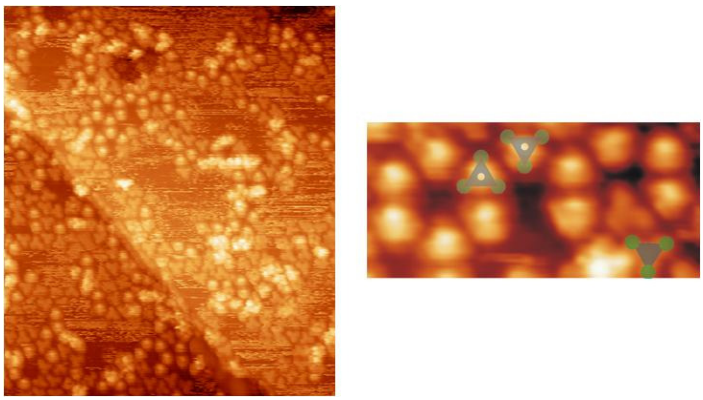

Figure 40. STM image of the evaporation of 12HSubPcCl on Cu(111). A). 14' at 150ºC. Two kind of conformations are distinguished: Chlorine up (brighter) and chlorine down(darker). 334Å x 392Å 0.6nA -2.1V 112Å x 131Å 0.5nA -2.4V

Within this disordered structure, small patches with a honeycomb pattern, almost exclusively formed by Cl-up molecules can be found (Figure 40b). After annealing to 70ºC for 1h, the area of the honeycomb islands increases, and islands with up to 100 nm in diameter can be found (Figure 41). Also in this case the honeycomb structure is formed almost exclusively by Cl-up molecules, although some Cl-down molecules can be found as substitutional defects or on the edges of the of the honeycomb areas, apparently hindering the growth of larger ordered domains.

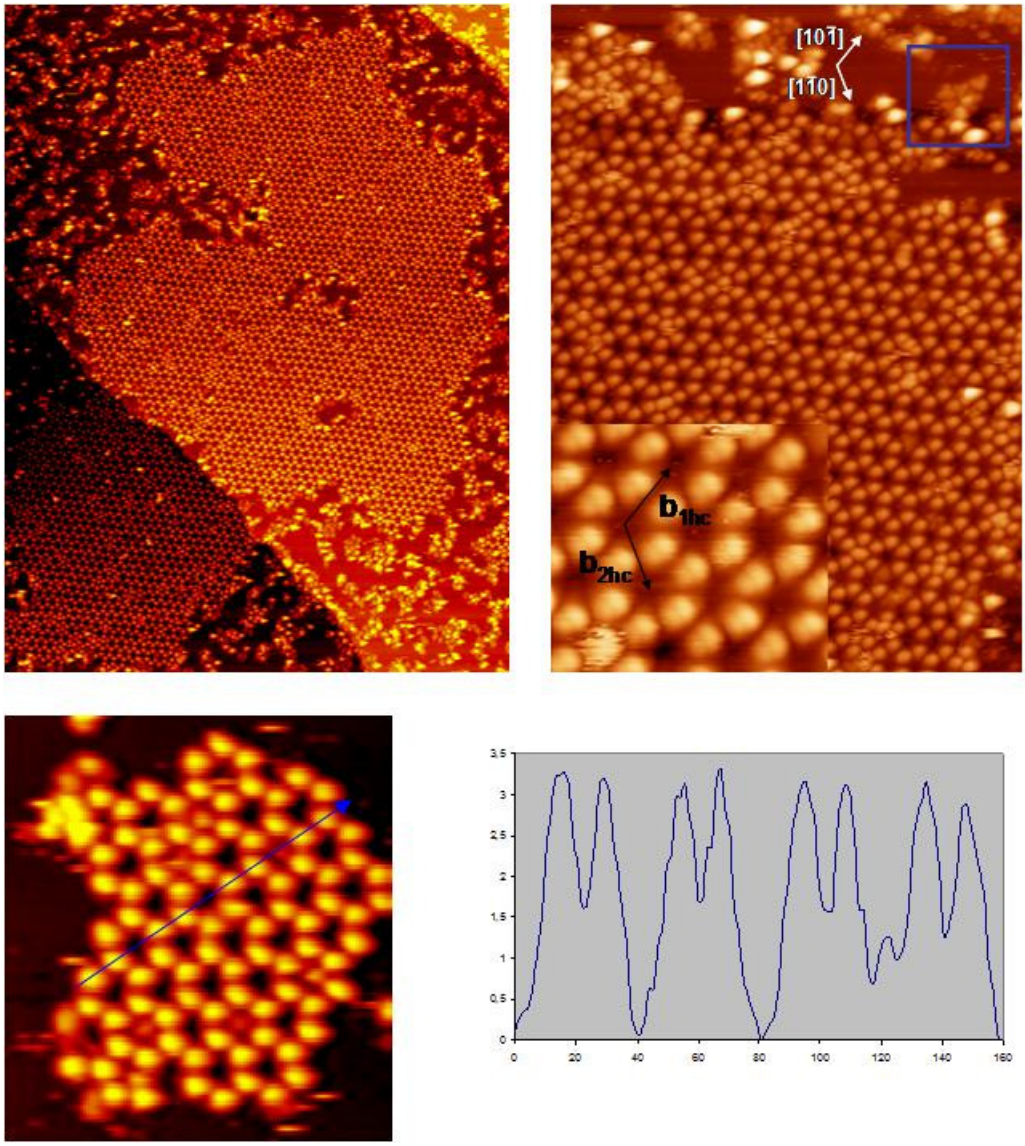

Figure 41. Image of the evaporation of 12HSubPcCl on Cu(111) and subsequent annealing. A honeycomb pattern aligned with the high symmetry [1-10] direction of the substrate is formed. 625Å x 800Å 0.5nA -2.4V 425Å x 600Å 0.6nA -2.0V 181Å x 200Å 0.5nA -2.1V

This honeycomb network is aligned with respect to the [1-10] high symmetry direction of the Cu(111) substrate, making a 9 x 9 unit cell superstructure (Figure 42) This well defined orientation implies that besides intermolecular interaction, molecule-substrate interaction plays a major role for establishing the registry of the molecular

overlayer. The length of the lattice parameter for this structure is 2.3 nm, while the distance between two nearest-neighbours molecules is 1.2 nm.

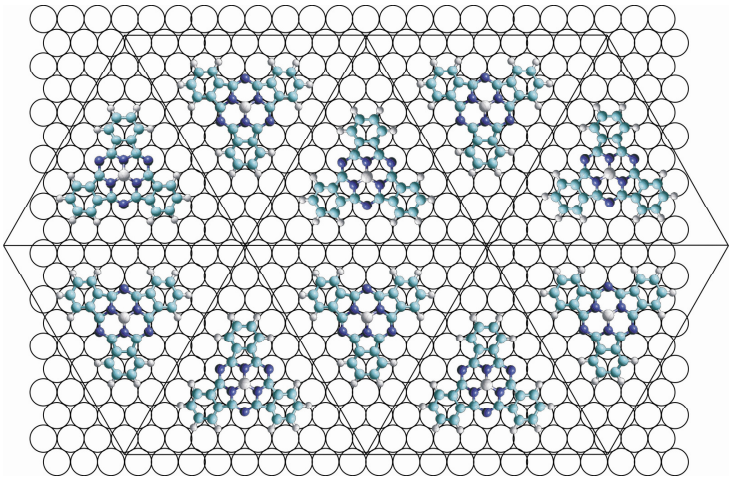

Figure 42. Schematic drawing of the honeycomb pattern that forms 12HSubPcCl on Cu(111), showing a perfect alignment with respect to the high symmetry direction of the substrate, which reflects a non-negligible molecule-substrate interaction.

A statistical analysis of Cl-up and Cl-down molecules shows that, before annealing, the percentage of Cl-up species is slightly above 50 %, while after annealing this number increases up to 80 %, which suggest that the thermodynamically stable situation is the Cl-up configuration.

As mentioned above, a similar honeycomb pattern of has been previously reported for 12HSubPcCl on Ag(111), but our results on Cu(111)show a quite smaller intermolecular distance of 1.34 nm (compared to 1.79 nm reported value for Ag (111)), and only one orientation (aligned with the substrate), instead of the two orientations (± 4.7º with respect to the [1-10] Ag(111)), previously reported.

3.2.1.1 Nanocrystals of 12HSubPcCl molecules

Increasing the coverage of 12HSubPcCl on Cu(111), we observe a striking result. Instead of growing larger honeycomb islands, we get more disordered islands and a new ordered structure in the shape of triangular islands begins to form (Figure 43). The islands are found with two different orientations with respect to the underlying close-packed directions of the Cu(111) surface. The angle between the island edges and the unit cell vectors of the substrate is ±15º, for each of these two orientational enantiomeric domains. The lattice parameter is 1.6 nm, i.e. about 30% smaller than the unit cell of the honeycomb structure, but about 20% larger than the closest distance between molecules in the honeycomb. They correspond thus to different structures and not to imaging the same structure.

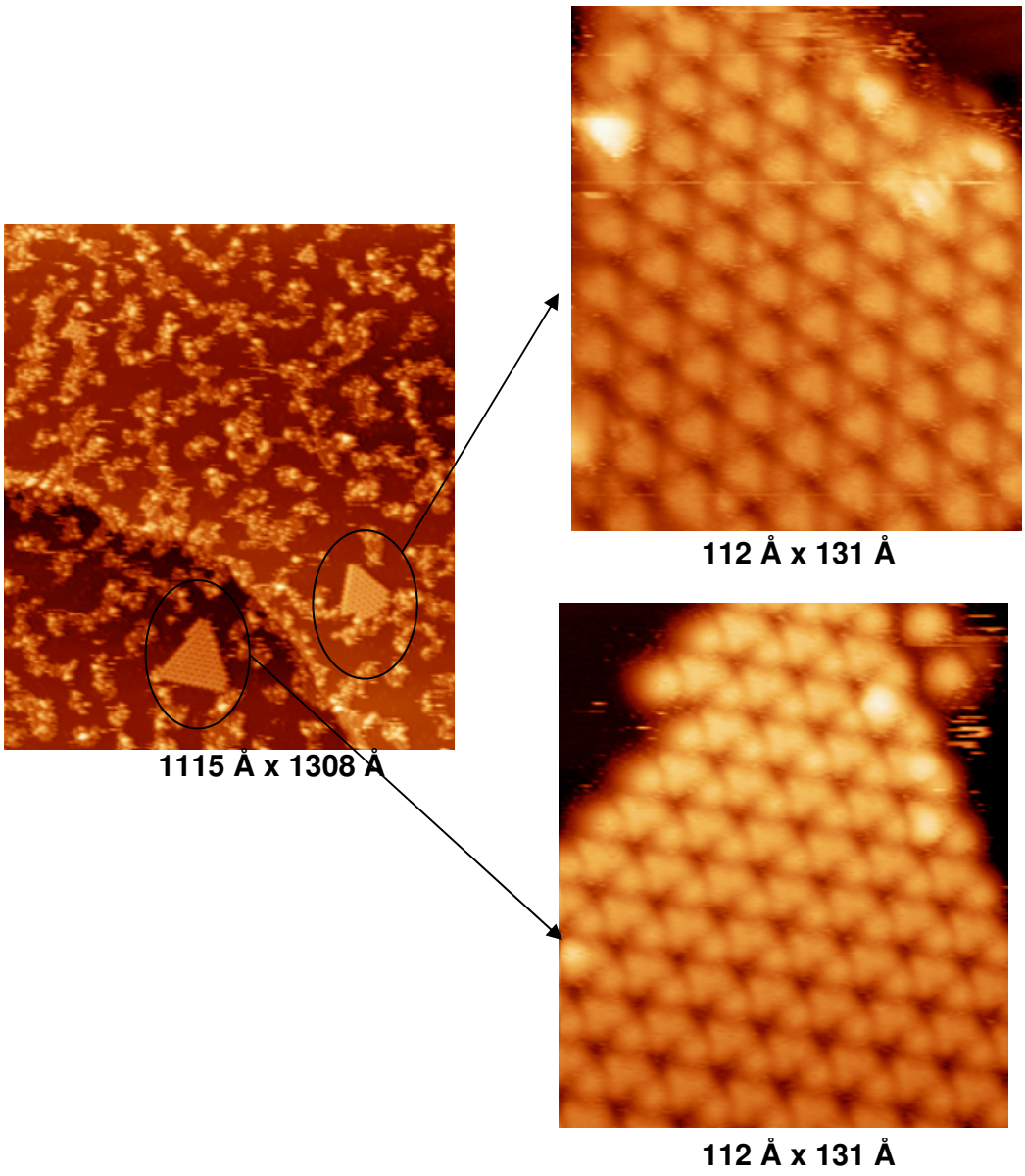

Figure 43. Enantiomeric islands on the Cu(111) surface

High-resolution STM images of the triangular islands reveal that the molecular arrangement is made out of two different SubPc species , which are imaged as bright protrusions (green circle) and trefoils (blue circle). The sublattice of bright-protrusions and the sublattice of trefoil features are both hexagonal (and not honeycomb-like), aligned with the island edges (and thus rotated by ±15º with the close-packed directions of Cu(111)) and with a lattice parameter of 1.6 nm, as mentioned above. The island edges only contain one SubPc species: the one imaged as bright protrusions in the STM images. The height of the bright protrusions is the same as the height of the features previously identified as Cl-up molecules; in contrast, the height of the trefoil features in the triangular islands is about 0.2 nm higher than the Cl-down molecules in the first layer, even though they share a similar trefoil appearance in the STM images. At his stage, thus, we not only have two different heights of the molecules in the STM images like but now three. We conclude that the bright protrusions correspond to 1st-layer Cl-up molecules with a hexagonal arrangement, whereas the trefoil features correspond to

2nd-layer Cl-down molecules sitting on the 3-fold hollow sites of the 1st-layer Cl-up arrangement

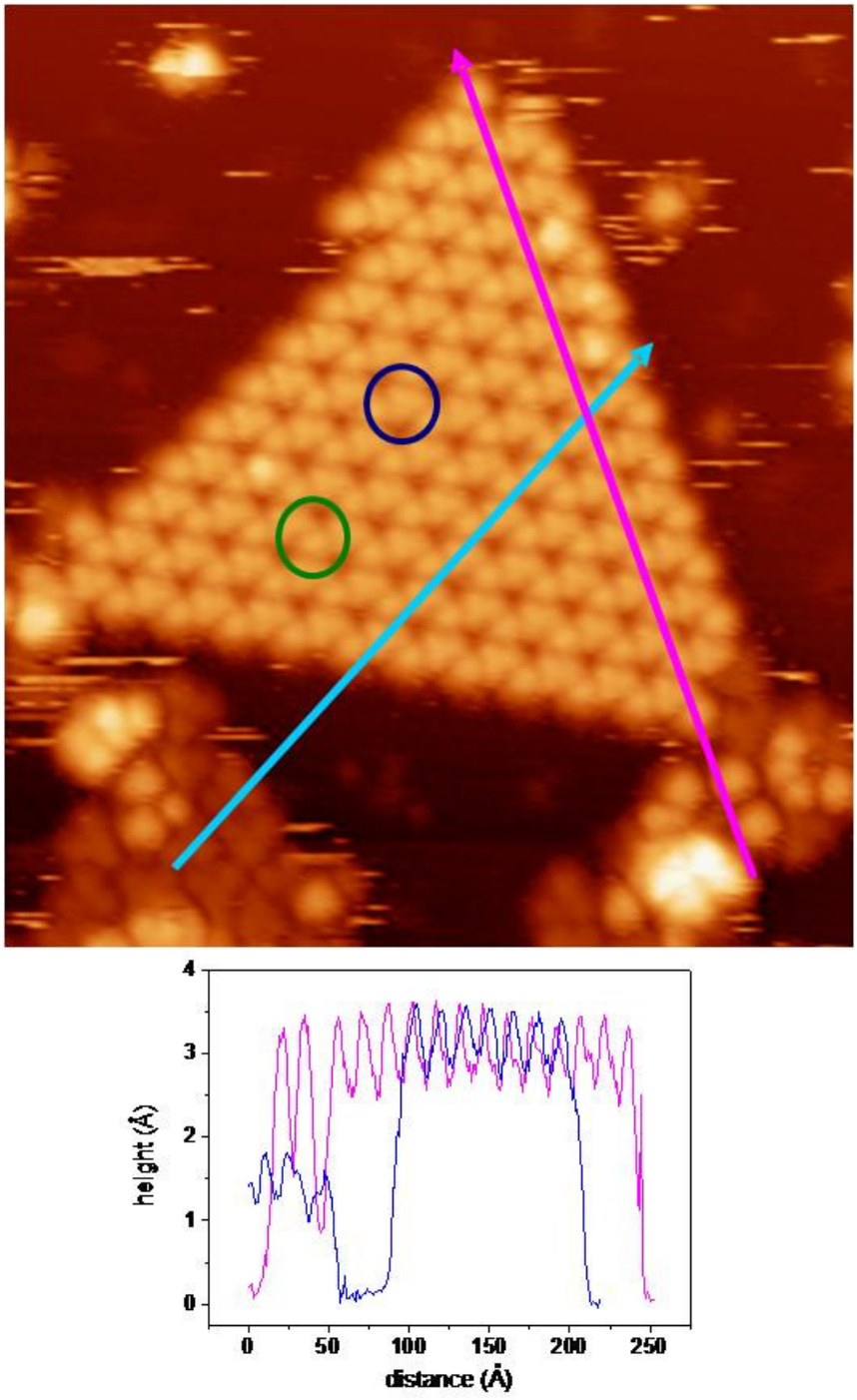

Figure.44. Organic nanocrystal of 12HSubPcCl molecules. 624Å x 416Å -0.8nA -2.9V

Further deposition of SubPc molecules on the sample containing nanocrystallites leads to a twofold effect. On the one hand, the disordered areas surrounding the triangular islands become more and more populated until there exist a 1 ML-thick connective tissue linking all the nanocrystallites. On the other hand new and even brighter features can be observed on top of the bilayer islands (see Figure 45). Such

protrusions appear clustered in trimers, and sitting in the threefold hollow sites of the 2nd layer, preferently those that do not have a 1st-layer, Cl-up molecule underneath, in a fcc-like stacking. Such hcp stacking explains the preferential orientation of the trimers in the same direction than the island. Only a small fraction of trimers are oriented in the opposite direction, and in this case the molecules follow an hcp-like stacking, i.e. the 3rd layer molecules are sitting on top of the threefold hollow sites with a 1st-layer Cl-up molecule underneath. The presence of another molecule directly underneath the 3rd layer molecule might explain the brighter appearance of inverted 3rd layer trimers versus normally oriented 3rd layer trimers..

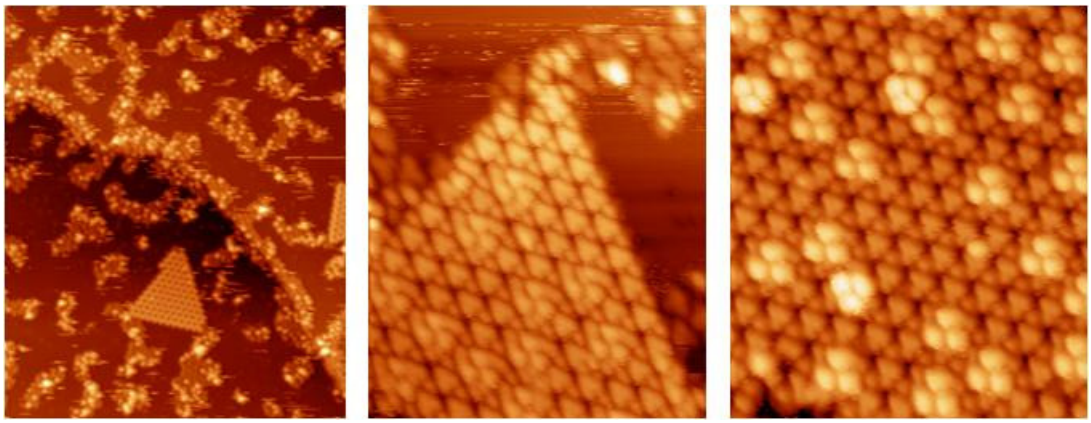

Figure 45. Increasing the amount of evaporated molecules we can observe even 3 rd layer. 425 Å x 600 Å 0.7nA -2.7V 334Å x 392Å 0.3nA -1.9V 181Å x 200 Å 0.8nA 2.2

3.2.1.2 Theoretical calculations

We have identified a system for which the growth of 3D nanocrystallites sets in before completion of the 1st-monolayer. Notice, however, that the honeycomb structure of the 1 ML-thick Cl-up islands is different from the hexagonal arrangement of the Cl-up 1st-layer in the nanocrystallites, indicating that the formation mechanism of the bilayer islands is not the adsorption of Cl-down SubPc molecules on previously formed 1 ML-thick Cl-up honeycomb structure. To seek alternative mechanisms for nanocrystallite formation we need further information about their structure.

The orientation of the trefoil-shaped Cl-down molecules on the 2nd layer around their C_3 axis with respect to the substrate lattice can be determined from our STM images. On the other hand, these images do not offer any clue as to the orientation of the underlying 1st-layer, Cl-up molecules. In order to propose a structural model for the bilayer islands, we have performed theoretical calculations of a 4-molecule cluster in the gas phase (molecular mechanics calculations with the MM+ force field from the HyperChem 7.0 package software). In this cluster we have placed three Cl-down molecules forming an equilateral triangle of 1.58 nm: Each of the Cl-down molecules is aligned with the direction of the supramolecular triangle, as observed for 2nd layer Cl-down molecules in our STM images (see Figure 46a). A Cl-up molecule (representing one of the molecules in the 1st layer of the triangular islands) is placed along the axis defined by the triangle's baricenter and the dipole moment of the SubPc molecules. In

the calculation the distance between the Cl atom and the plane determined by the topmost hydrogen atoms of the supramolecular triangle of 2nd layer molecules (z) is changed from 0 nm to 0.3 nm. We have calculated the bonding energy of the system as a function of the molecular orientation of the 1st layer with respect to the 2nd (as determined by the angle θ defined in Figure 46a) for different interlayer distances z, and the resulting energy landscape is plotted in Figure 46b.

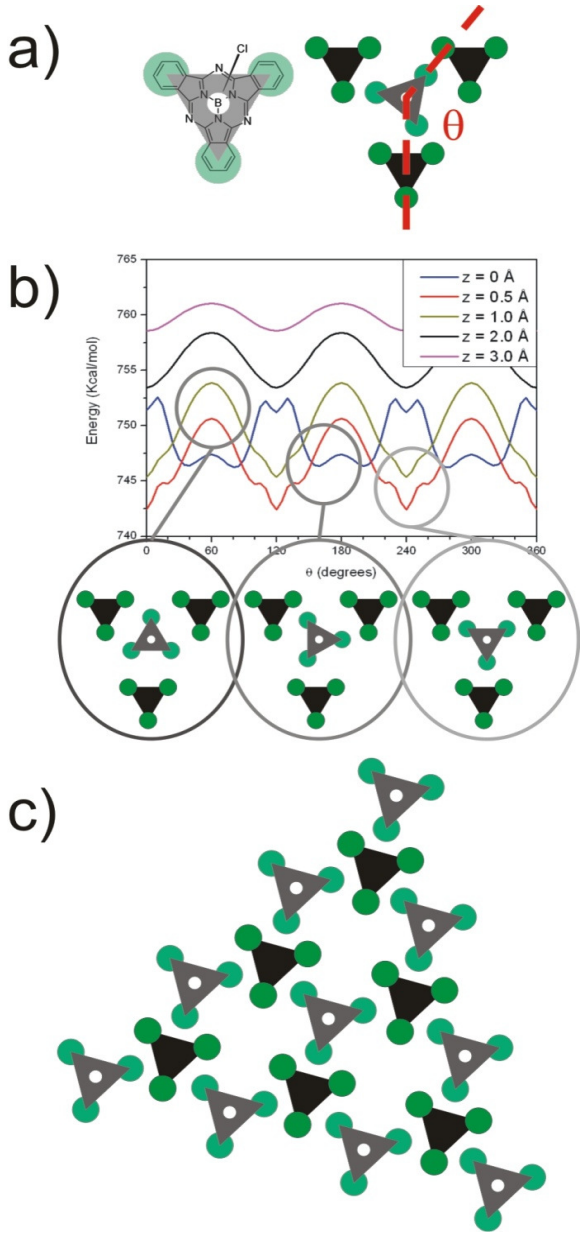

Figure 46. Gas-phase model cluster for Molecular Mechanics calculations. The configuration of the 2nd layer Cl-down molecules is kept fixed to the experimentally observed configuration, whereas both the interlayer distance and the molecular orientation of the 1st layer Cl-up molecule is changed systematically in order to obtain the energy landscape. b) Angular dependence of the cluster's bonding energy for different interlayer distance. All the curves show the C3v symmetry of the original cluster. The configurations of the maxima and minima in the curves are shown as insets. c) Structural model for the triangular nanocrystallites based on experimental STM images and the cluster calculations described in a) and b).

vdW and π-π interactions as well as dipole-dipole interactions between both layers are the main bonding interactions expected to play a role in the stabilization of the nanocrystallites. The trend to higher bonding energies for decreasing interlayer distance in the range 0.3 nm > z > 0.05 nm can be ascribed to the strengthening of dipole-dipole interactions at short distances. However, since the molecular dipoles are parallel to the B-Cl bond, i.e. out of plane, the dipole-dipole interaction is not expected to change significantly with rotations around the C_3 molecular axis. The molecular orientation in such a model cluster must rather be determined by the vdW and π-π interactions. This observation is confirmed by our calculations in Figure 46b: For every interlayer distance, except the smallest one, the minimum energy configuration is such that the 1st-layer Cl-up molecule shares the same orientation with the 2nd layer Cl-down molecules, thereby maximizing π-π interactions between the inner rings of the Cl-down and the outer rings of the three Cl-up molecules. Moreover, θ = 60º is always a local energy maximum due to the lack of π-π interactions. Finally, for z = 0 nm, the inner rings of the Cl-down and the outer rings of the three Cl-up molecules get close enough for steric repulsion to take over π-π interactions. In this case the angle-averaged bonding energy increases, and the minimum energy configuration is characterized by a rotation to θ ~ 90º.

From our cluster calculations we propose the structural model depicted in Figure 46c for the triangular nanocrystallites. The 2nd layer (1st layer) molecules are depicted in darker (lighter) colours. The orientation of the 2nd layer molecules is the one obtained from our experimental STM images. This model explains the triangular shape of the nanocrystallites. Since both 1st-layer and 2nd layer molecules show hexagonal arrangements, the reason for the crystallites to be triangular instead of hexagonal is not immediately clear. However, close inspection of the model shows that the structure of a hypothetical step-edge at 60º with respect to the observed would be less stable than the observed one. In such a step-edge, 1st layer molecules would be interacting with only one instead of two 2nd layer neighbours, thus rendering its overall configuration energetically unfavourable.With this information, a schematic drawing of the structure of the tow enantiomer islands in shown in Figure 47.

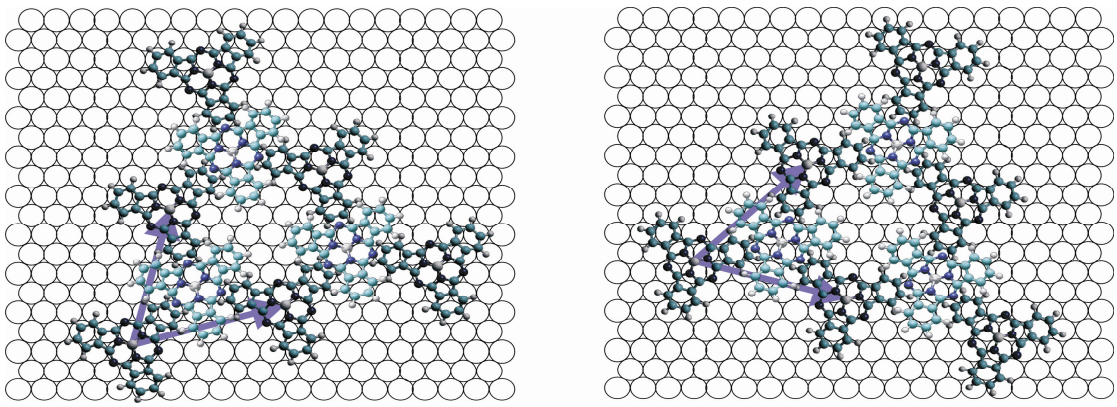

Figure 47. Two different domains of enantiomer islands.

In summary, our results show that the strong dipolar and π-π interactions between adsorbed SubPc molecules, together with the coexistence of two adsorption geometries, Cl-up and Cl-down on the Cu(111) surface direct the growth of nanocrystallites with well-defined shapes and sizes even before the 1st monolayer has been completed. On the basis of our results, we propose that the growth of nanocrystallites on solid surfaces versus single-height monolayers can be promoted by using non-planar molecular architectures provided with strong dipoles and whose adsorption geometry forces the dipoles to be directed out of the surface plane. This strategy is thus opposite to the one followed in most of the previous organic growth studies on solid surfaces, in which the molecular species rest flat on the surface, and their possible dipole moment is also parallel to the surface. As a result of the strong out-of-plane dipole-dipole interaction, such islands will tend to show an antiferroelectric stacking. We expect that a careful control of the 3D shape of the molecular adsorbates will lead to new ways to build 3D molecular nanostructures at solid surfaces, with tuneable optical properties and thus, a strong potential for optoelectronic device applications. This control over the size and shape of the islands might in principle be achieved by using prepatterned surfaces such as bimetallic surfaces with strain-relief patterns or chemically inhomogeneous surfaces.

3.2.2. 12HSubPcF on Cu(111)

In order to try to quantify the role of the dipole moment on the formation of the honeycomb structure we have deposited two other subphthalocyanines derivatives: 12HSubPcF and 12FSubPcCl.

12HSubPcF molecule is similar to 12HSubPcCl where the axial Cl atom has been replaced by a F atom (Figure 38). The lower polarizability of the F atom leads to a reduced dipole moment of 4.0 versus 4.6 Db for the 12HSubPcCl molecule.

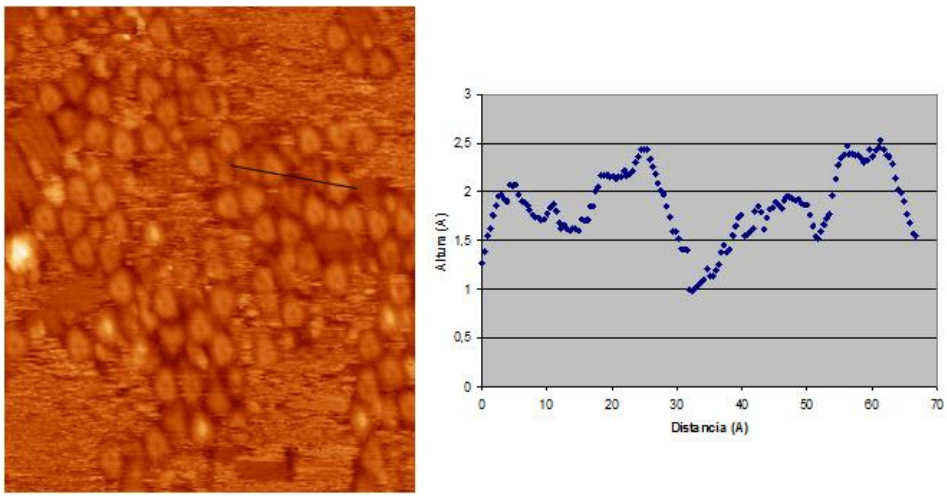

Figure 48. STM image and profile of the evaporation of 12HSubPcF on Cu(111) 223Å x 261Å. 0.4nA - 2V

As in the case of 12HSubPcCl when we evaporate a small amount of 12HSubPcF on Cu(111) we observe disordered islands where again we can distinguish two different molecular conformations: a darker trefoil shaped one, and a brighter rounded triangle with a dark circle in the center (Figure 48). Taking a profile height, we see that the difference in height between both molecules is almost 0.5 Å (Figure 48). Due to the fact that the only change with respect to 12HSubPcCl is just the substitution of the chlorine atom by a fluorine atom, we believe that trefoil-shaped molecule corresponds to the adsorption of 12HSubPcF with the fluorine down (F-down), and that the b molecule represents the adsorption of 12HSubPcF with the fluorine up (F-up).

For low coverages, and as in the previous case, a light annealing (50º- 80º C) favor the formation of small islands with a honeycomb structure formed by F-up molecules, (see Figure 49). The lattice parameter is 2.4 nm, but now two different orientations, with the lattice vectors rotated ± 22º with respect to the lattice vectors of the substrate coexist on the surface (Figure 50).

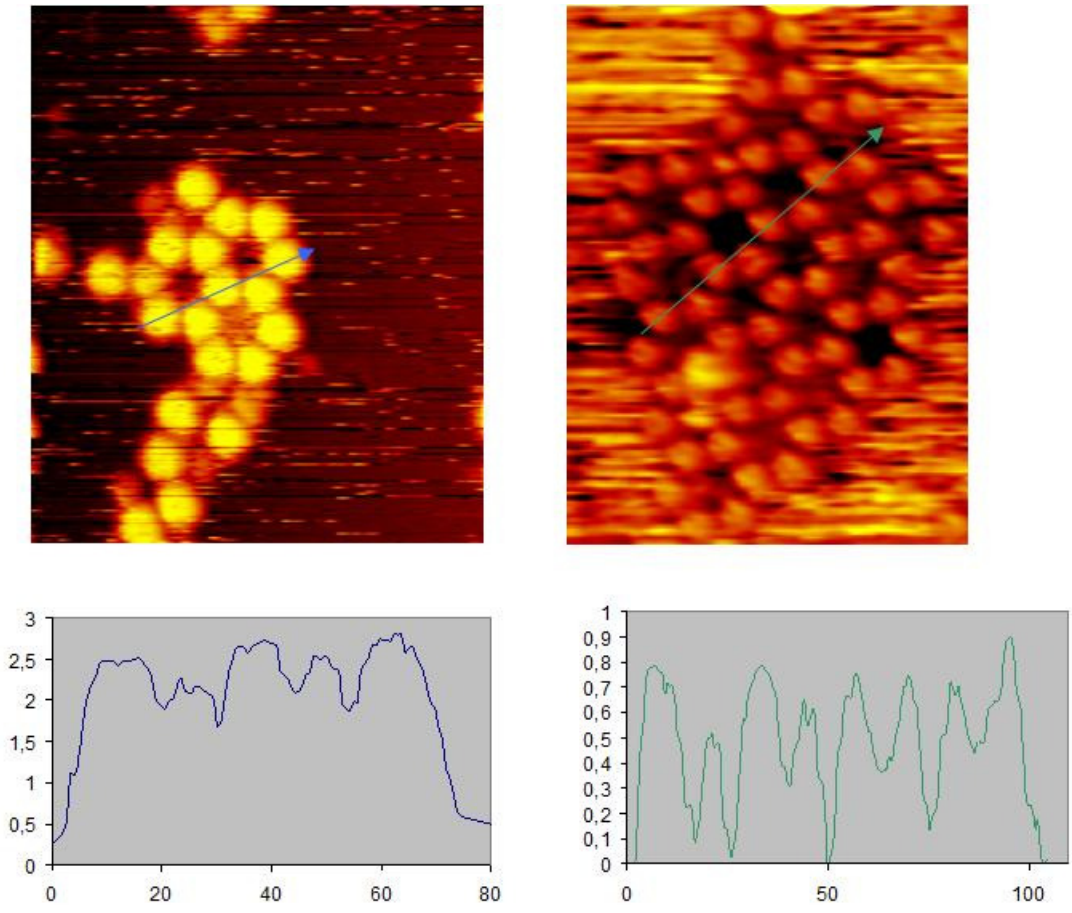

Fig. 49 STM image of the evaporation of 12 HSubPcF on Cu(111), 223Å x 261Å 0.8nA -1.9V 223Å x 261Å 0.8nA -1.8V

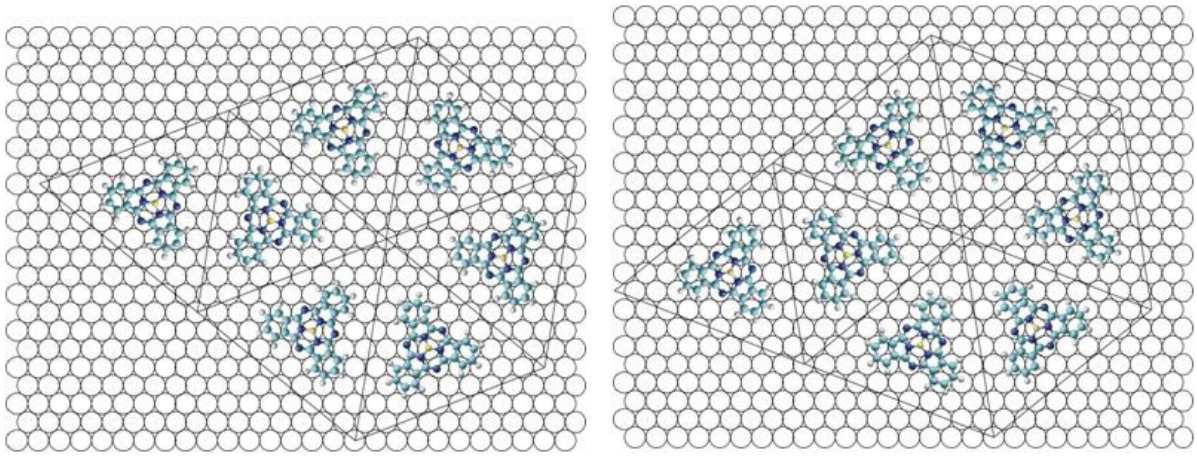

Figure 50. Schematic drawing of the honeycomb molecular network that forms the 12HSubPcF molecule.

For coverage close to the monolayer, annealing at 80ºC for 15 minutes gives rise to a compact hexagonal close pattern of F-up molecules (Figure 51). The HCP molecular domain is aligned with the substrate lattice vectors, forming a 8 x 8 superstructure, with a lattice parameter of 2.04 nm and has a nearest neighbor distance of 1,76nm.

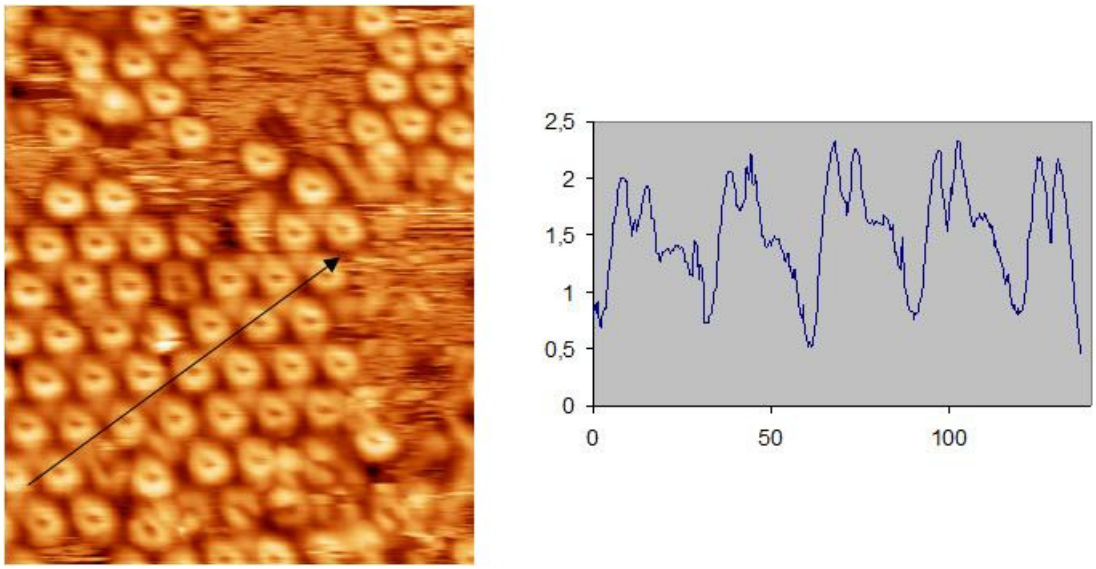

Figure 51. STM image of the evaporation of 12HSubPcF on a clean Cu(111) 223Å x 261Å 0.3nA -2.3V

3.2.3 12FSubPcCl on Cu(111)

As in the previous cases, when we evaporate 12FSubPcCl on Cu(111) we observe disordered islands with some local organization into honeycombs (Figure 52). The honeycomb network is rotated 30º with respect to the substrate, with a network parameter of 2,5 nm x 2,5 nm (Figure 53).

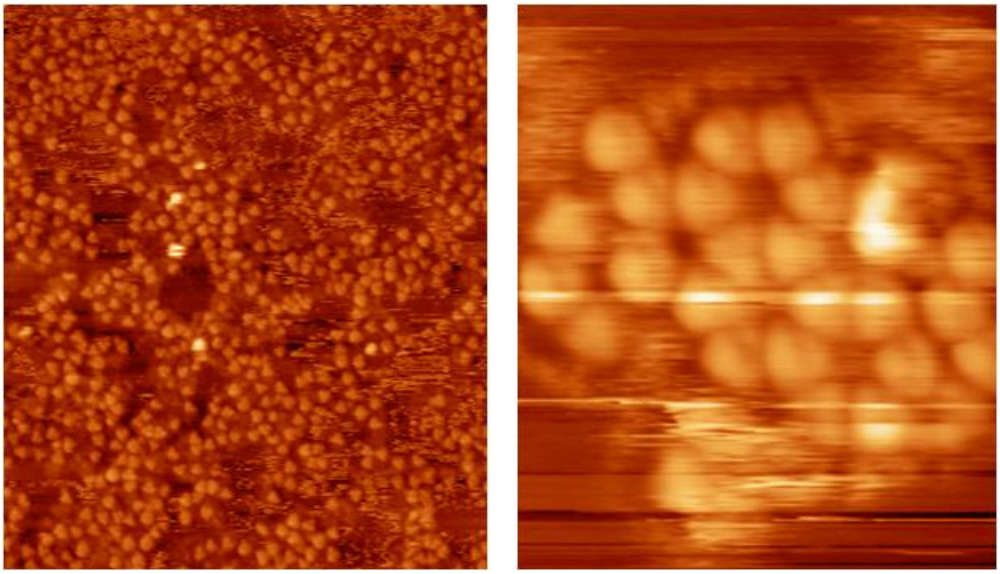

Figure 52. STM images of 12FsubPcCl molecule on Cu(111)558 Å x 654 Å 0.6 nA – 1.8V 112 Å x 131 Å 0.4 nA -1.9V

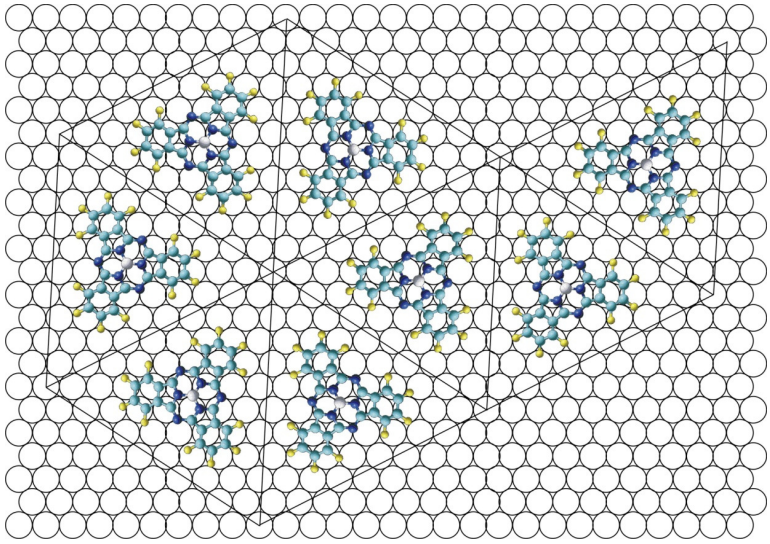

Figure 53. Schematic drawing of the honeycomb molecular network that 12FSubPcCl forms on Cu(111).

3.2.4 Comparison between different SubPc family molecules.

In the table 1 the comparison between the structures obtained for the SubPc molecules family is presented. Interestingly, in the three cases honeycomb structures are found. The ordering of the honeycomb patch is better in the first molecule. The lattice parameter and the nearest neighbor distance changes depending on the peripheral functionalization. Whereas for hydrogenated molecules the last number is about 12,3 Å, for fluorinated molecules the distance is much larger, about 12,8 Å. This could be related to the much lower dipole moment of the fluorinated species.

Molecule	lattice	lattice parameter (Å)	nn distance(Å)	angle	Dipole moment (D)
12HSubPcCl	Honeycomb	23.2	13.3	0	4.6
	Triangular	15.6	15.6	±15	
12HSubPcF	Honeycomb	24.6	14.2	±22	4.0
	Hcp	17.8	17.8	0	
12FSubPcCl	Honeycomb	24.3	14.2	30	2.2

Table 1. Comparison between SubPc molecules

3.3 Conclusions

In summary, we show the creation of a different structures on the copper (111) surface: honeycomb and nanocrystal. For all investigated species a honeycomb ordered pattern is obtained. Just only for the 12HSubPcCl molecules the formation of the organic nanocrystals is found after increasing coverage of sublimated molecules at the surface. The nanocrystals grow up to third layer creating trimers imaged as a bright protrusion. In the studies of SubPc family is presented importance of the dipole moment into the growth process. Taking into account the showed data it is concluded that organic molecules can leads to grow at metal surface into nanocrystals where molecule-molecule interactions play a major role.

Chapter 4: Oxalic Acid, Molecular Coordination Networks

4.1 Introduction

In this chapter we will present the metal organic framework with the smallest metal-to-metal distance reported up-to-date. We will focus on the growth and characterization of the smallest molecule which can be linked to Fe atoms and self assemble into two dimensional (2D) MOCNs (Metal Organic Coordination Networks) (70) through coordination bonding. This smallest molecule is oxalic acid.

4.1.1 Metal-Organic Coordination Networks

MOCNs are compound of organic ligands coordinatively bonded to metallic atom. MOCNs provide new ways for creating well ordered nanoporous materials that could be used in catalysis, synthesis or as sensor materials (8) (71) (72). It was recently shown that 2D MOCNs can be grown on metal surfaces by codeposition of the organic ligands and the metallic adatoms.

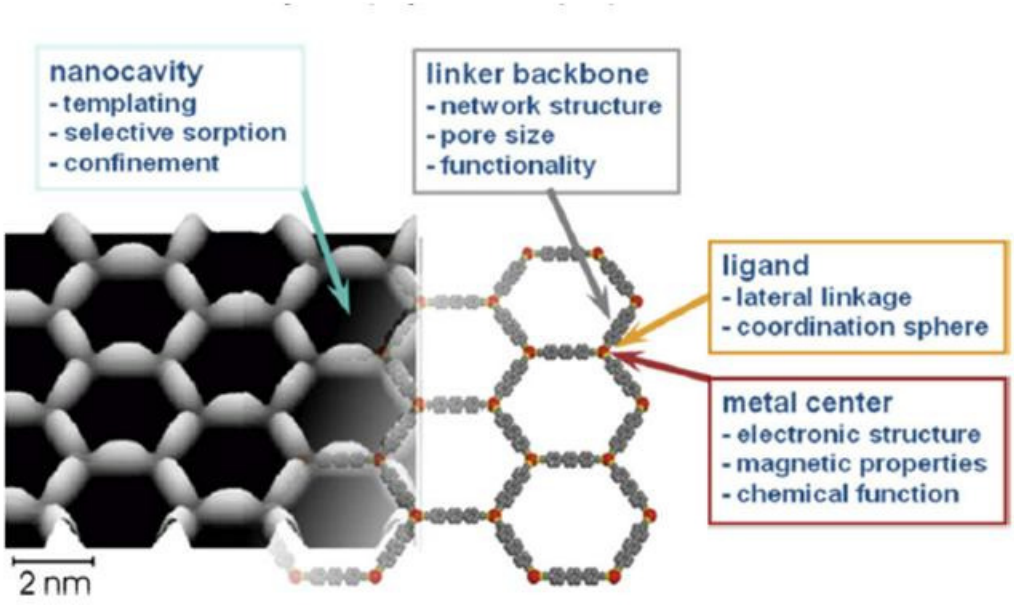

Figure 54. MOCNs at metallic surface.

In the Figure 54 we see the properties of the MOCNs. The metal center can be chemically functionalized with magnetic properties. The ligand play a role of lateral likage and can be changed depending on the codeposited molecules. Also in MOCNs is important the possible templating of the surface in nanoporous scale. In particular, a lot of attention has been paid to metal-organic coordination networks (MCONs), with the

idea of creating functional metallo-supramolecular arrays on surfaces (70). These arrays combine the properties of their constituent metal ions and ligands, showing unique optical, electrochemical and magnetic properties. In addition, metal-ligand interactions are more robust than relatively weak intermolecular interactions, such as hydrogen bonding, van der Waals or electrostatic forces, which provides better thermal stability. These features present potential relevance for nanotechnology, particularly in the area of supramolecular devices for selective molecular recognition and hosting (73), catalysis (74), information storage (molecular magnets (75)) and processing. (76)

Up to now, the investigation have been mainly focused on compounds with carboxylic groups and transition metals which properties are well known giving possibility to investigate metal-ligand structures, although some other metal binding groups as cyano groups have been tested as well. Moreover, all of them contain aromatic moieties in their backbones. These ligands have been designed to promote a planar adsorption geometry, enabling the metal binding centers to hold periodic 2D networks (examples shown in Figure 55, compunds 1-4) (77) (78) (79). Previous studies on non-aromatic carboxylate ligands show that the absence of a π congungted electron system make the σ-backbone of the molecule to bend, thus enabling the bonding between the carboxylate groups and the metallic surface, (80) and thereby hindering the formation of planar coordination networks.

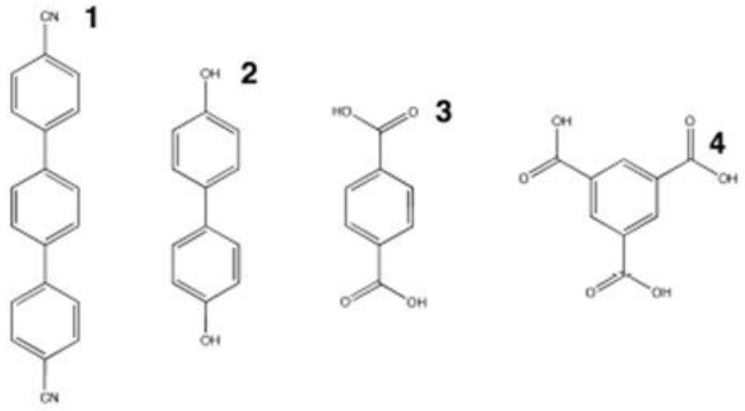

Figure 55. Scheme of the ligands reported in the literature.

As an example, let us consider the previous studies on trimesic acid (tma) on the copper (100) surface. This compound consists of three equivalent carboxylic groups linked to a central phenyl ring. After depositing in Ultra High Vacuum on a Cu(100) surface held at 300 K, the carboxilic molecules are deprotonated and.the carboxylic groups stay at the surface as a reactive carboxylate (COO^-) might be used as a ligand to the metal. The molecules appear with a triangular shape in the STM images groups, consistent with a flat laying geometry. From this studies we know that oxygen atoms from the carboxylic group are not equivalent, the distance between Cu…O is around 3Å, normally should be smaller approximately 2Å, and is related to the atomic lattice of

the surface. The coordination bond between Cu and oxygen is changed because of electrons from the surface conduction band. At the surface is forming complex which can be described as $[Cu(tma)_4]^{n-}$ as in Figure 56. (81) (82).

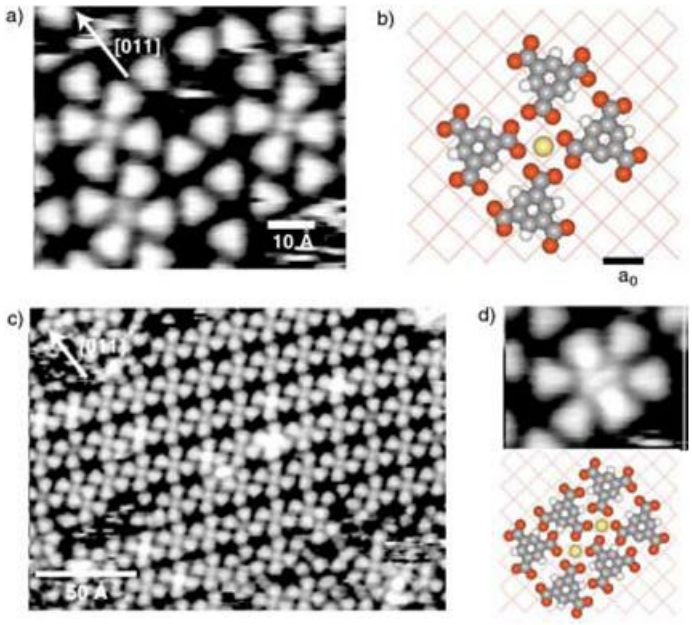

Figure 56. STM studies on tma molecule on copper(100) surface linked to the Cu atom

In the example above, the Cu adatoms are coming from the step edges. In order to provide MOCC`s with functionality is importantt to use metal centers different from substrate atom. Thus can be achieved by codeposition of the organic linker and the metallic adatom. In this this case iron atoms were evaporated to fabricate complexes $[-Fe\text{-}TMA-]_n$ like that shown in Figure 57.

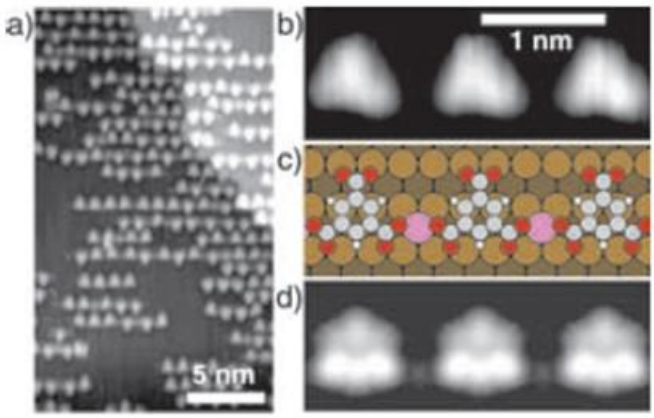

Figure 57. STM images of TMA molecules linked to the iron atom in the MOCC structures.

Another example of a MOCNs formed by iron atoms and a large aromatic molecule is presented below. We can see that with an appropriate choice of the molecule, both the size and shape of the MOCN can be modified at will.

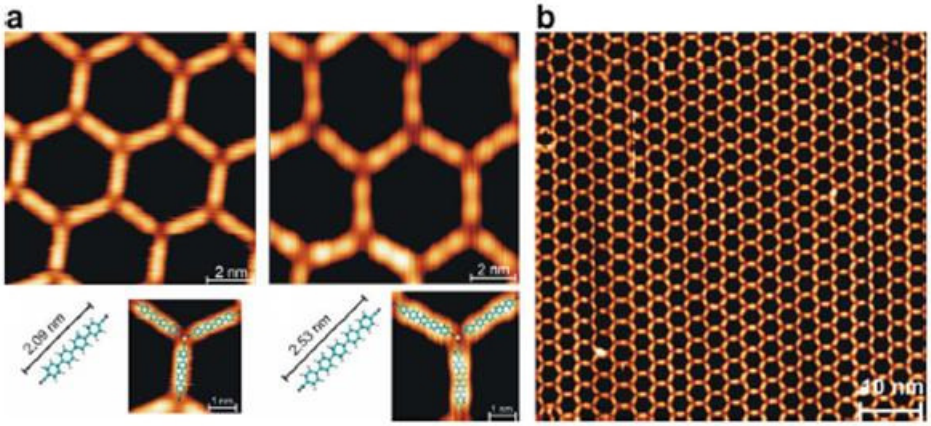

Figure 58. 2D MOCNs of large aromatic molecules.

2D MOCNs have been proposed for a numerous applications. For magnetic application, however, the molecules shown above are quite large, with at least one benzene ring in the structure of the molecule, and the distance between iron atoms is relatively large. Our aim in this work will be to fabricate MOCNs with the smallest molecular ligands with two carboxylate ends implying shorter distance between iron atoms to achieve magnetic properties appropriate for further development.

4.1.2 Carboxilic acid on metal surfaces

Carboxilic acid is a molecule consisting of two of carboxylic groups linked together, whose empirical formula is as $C_2O_4H_2$. Figure 59 displays a structure of the molecule.

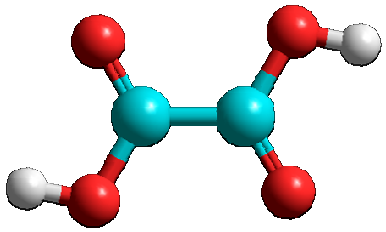

Figure 59. Structure of trans oxalic acid, in red oxygen, in blue carbon, in white hydrogen.

The adsorption a number of different molecules containing carboxilic acid groups has been the subject of a large number of studies, which have shown that, depending on the metal, the surface orientation, and the temperature, the molecule may undergo different processes. Thus, the molecule can be adsorbed intact, without deprotonation or may suffer a partial or total deprotonation. In the case of the carboxilic acid, the result of these processes is expected to strongly influence the adsorption conformation. Thus, in the first case, a planar adsorption geometry is expected in order to maximize vdW interactions. On the other hand, a full deprotonation will also

probably force a flat adsorption configuration. The intermediate case, partial deprotonation, may result either in a flat or an upright adsorption.

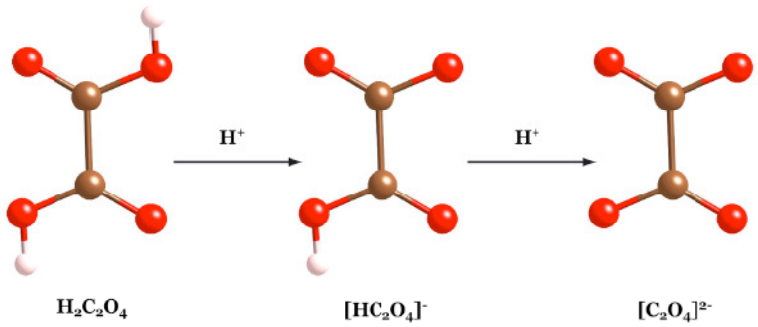

Figure 60. Oxalic acid after deprotonation process.

To our knowledge, there is only a previous study of the adsorption of oxalic acid on a copper surface, Cu(110), which reports experiments using techniques as Reflection Absorption Infrared Spectroscopy (RAIRS) and Reflection Anisotropy Spectroscopy (RAS) (83). Upon adsorption there is a partial deprotonation of part of the molecules. The adsorption geometry depends on the coverage. For low coverage oxalic acid is adsorbed perpendicular to the surface but tilted in the plane of the molecule (Figure 61a,b). When increasing the amount of evaporated molecules oxalic acids changes to an upright conformation, with both oxygen atoms from the carboxylate group towards the surface (Fig 61c, d). Non-deprotonated molecules are found to form hydrogen bonds.

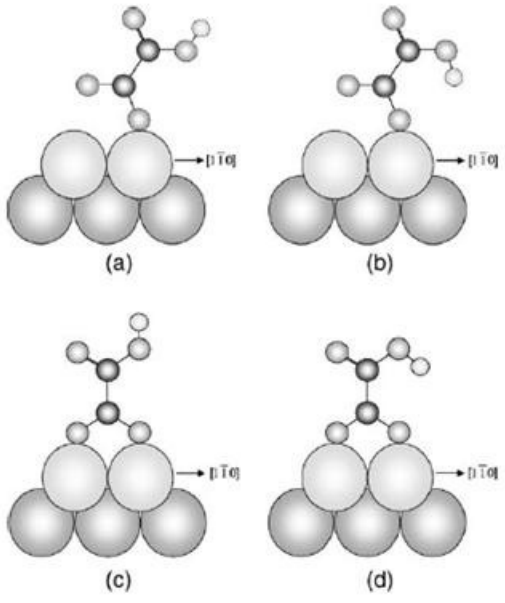

Figure 61. The different oxalate orientations deduced from the RAIRS spectra.

TPD measurements indicate that the molecule is stable till 400 K and above 500 K CO and CO_2 fragments are observed, indicating the breaking of the molecule.

4.1.3 Oxalic acid and magnetic properties of Tris(oxalato)Iron(III) compounds.

In the article of Mathoniere et al. have investigated the magnetic properties of tris(oxalato)iron(III) compounds. They have shown that the compound 3D structure contains 2D honeycomb structures showing collective magnetic properties up to critical temperatures T_c between 33 and 48 K giving possibility to correlate chemical and magnetic properties for the templates.

Oxalic acid is the smallest molecule capable of having two σ bonded carboxylate ends by full deprotonation of its two carboxylic acid groups. Indeed, it has been shown that salts of oxalate derivatives and transition metal are very often magnetic up to high temperatures.

Although the fabrication of 2D iron oxalate networks could be interesting from the applications in magnetic it also very challenging. There are the various problems to check as:

- full deprotonation of the molecule
- intacting of the molecule upon adsorption and
- orientation of the molecule.

The purpose of our investigation is to codeposit oxalic acid together with the iron adatoms to create MOCNs at noble metals.

4.2 Experimental

Oxalic acid molecules were synthesized according to a previously reported method at the University of Valencia, in the Organic Chemistry Department by the group of Prof. Eugenio Coronado. The Cu(111), Cu(100) and Au(111) surfaces were prepared by cycles of Ar+ sputtering (500 eV) and annealing at 850 K, until no contamination was present by Scanning Tunneling Microscopy (STM) inspection. Molecules were thermally evaporated from glass crucible at 40 ºC to the clean surfaces and the images were taken at low temperature 80 K. Sample was kept at RT over the sublimation process. In case of Au(111) surface was kept at low temperature -50ºC over deposition process.

XPS and XAS experiments were performed at MAX-Lab, beamline 313 at Lund University with collaboration with Dr. Joachim Schnadt group.

4.3 Results

In this chapter the adsorption of oxalic acid onto different substrates as Au(111), Cu(111) and Cu(100) will be discussed.

4.3.1 Oxalic Acid on Au (111).

Trying to avoid chemical decomposition and/or deprotonation of the oxalic acid when deposited on the metal surface, we start by depositing the molecules with the substrate held at low temperature on the chemically inert Au(111) surface

Figure 62a and 62b show increasing resolution STM images after depositing ~0.7 ML. Although there is no long range order, the surface is covered with a mixture of two phases: small domains with a Kagome structure, and a second mostly disordered phase. The effect of annealing procures can be seen in Figure 62d. It can be observed that the disordered areas disappear, and a new square phase becomes the most common one.

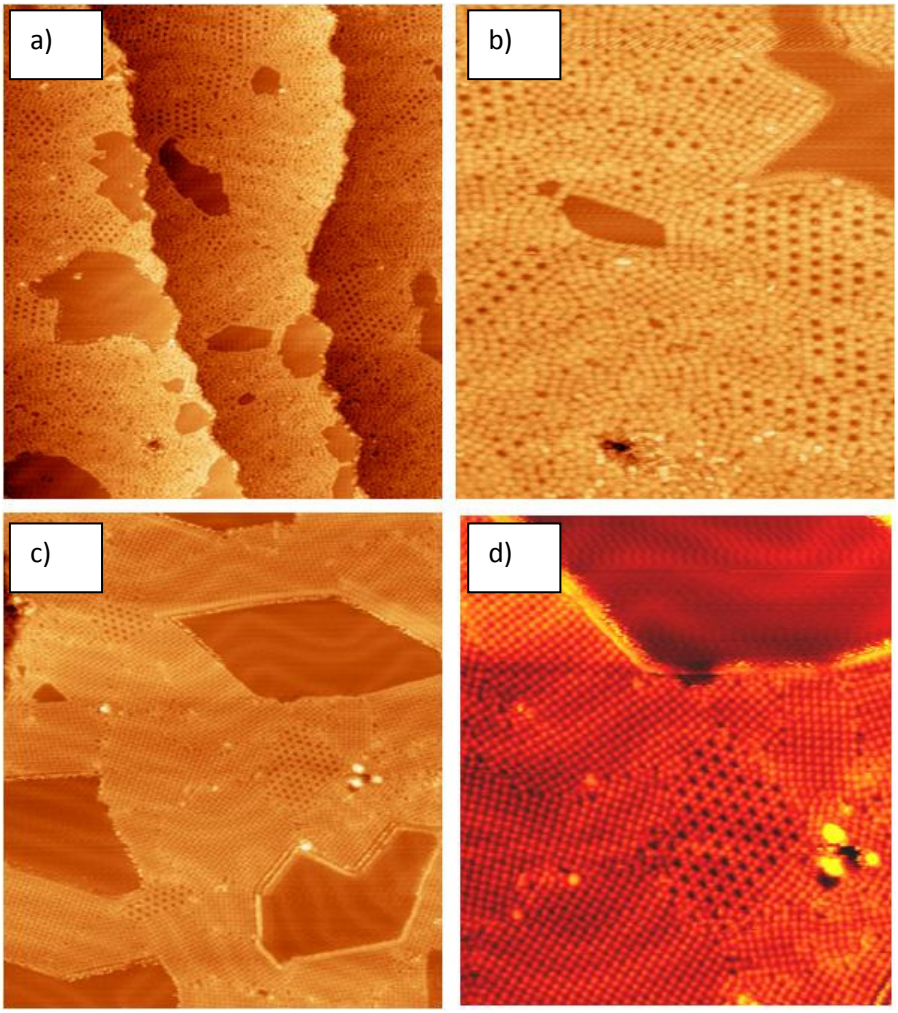

Figure 62. a-b) Increasing coverage of sublimated molecules 0.7 ML 0.8 ML and 1.2 ML. d) After annealing to 40ºC the small domains with a Kagome structure remain on the surface, but the disordered

phase has rearranged itself into domains with a square symmetry. a)425Å x 433Å, 0.2 nA -2.2V b)170Å x 217Å, 0.3nA -2.1 V c)425Åx433 Å, 0.6nA -2.6V d)255Å x 359Å, 0.5nA -1.6V

In the Kagome phase we do observe different domains: with the lattice vectors aligned with the high symmetry direction of the substrate or rotated ±15º .A model of the molecular structure for the Kagome phase, based on hydrogen bonds between the molecules, is shown in Figure 63. Theoretical calculations predict a distance between molecules similar to the experimental one (around 5,2 Å).In this model each molecule is stabilized by four hydrogen bonds, with a distance oxygen-hydrogen of 1,4Å.The similarity between the experimental results and the theoretical calculations allow us to conclude that in this phase the molecules are intact, lying flat on the surface and self-assembled through the formation hydrogen bonds.

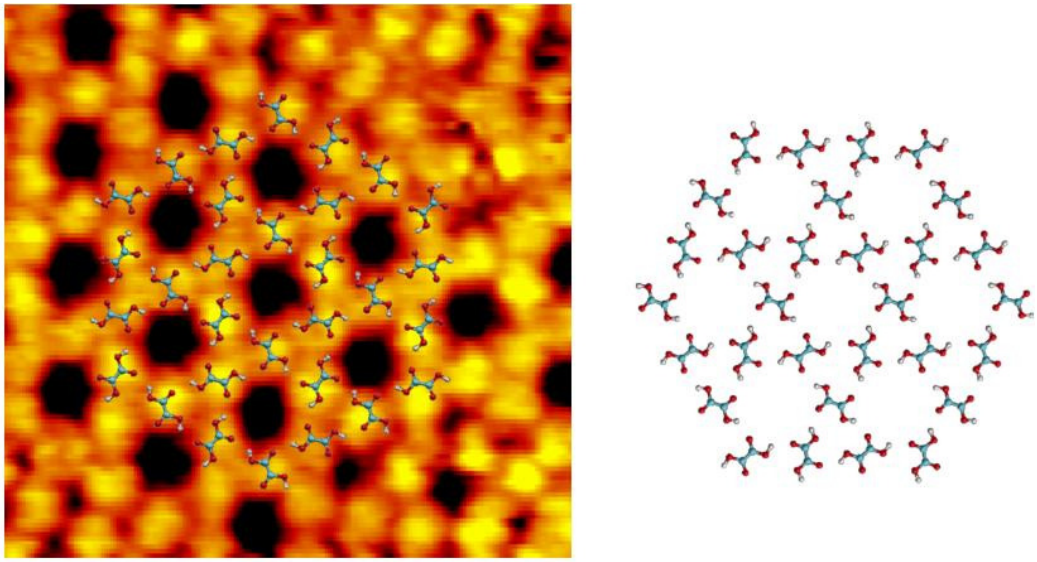

Figure 63. Calculated model for the Kagome phase. 49 Å x 56Å 0.4nA -2.7V

Figure 64 shows a detailed view of the square symmetry structure. Although the main features in the figure correspond to a square lattice with a ~5.1 Å x 5.1 Å unit cell, a careful look and the Fourier transform of the STM image show that the real unit cell is a centered 7.2 Å x 7.2 Å.

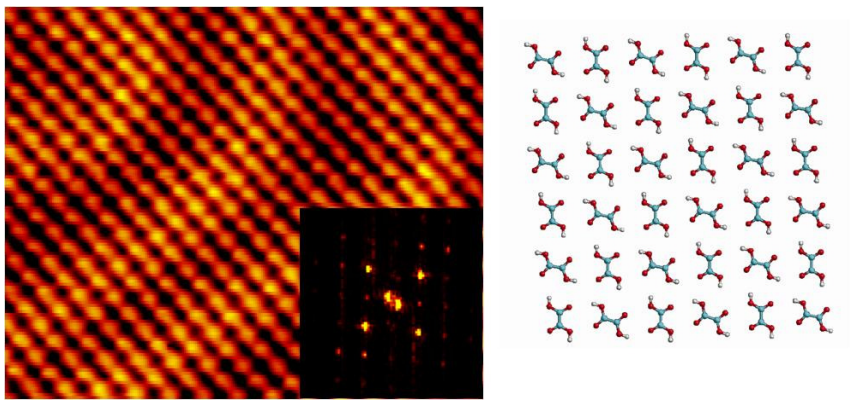

Figure 64. Square phase, STM image and tentative model. 253Å x 161Å 1.1nA -2.4V

A detailed analysis of the orientationsl domains show that there is not preferred orientation of this square phase with respect to the substrate. Only in Figure 66 we can see eight different domains, with no particular orientation with respect to the high symmetry directions of the substrate, which indicates a hydrogen-bonded layers of oxalic molecules interacting very weakly with the Au(111) surface.

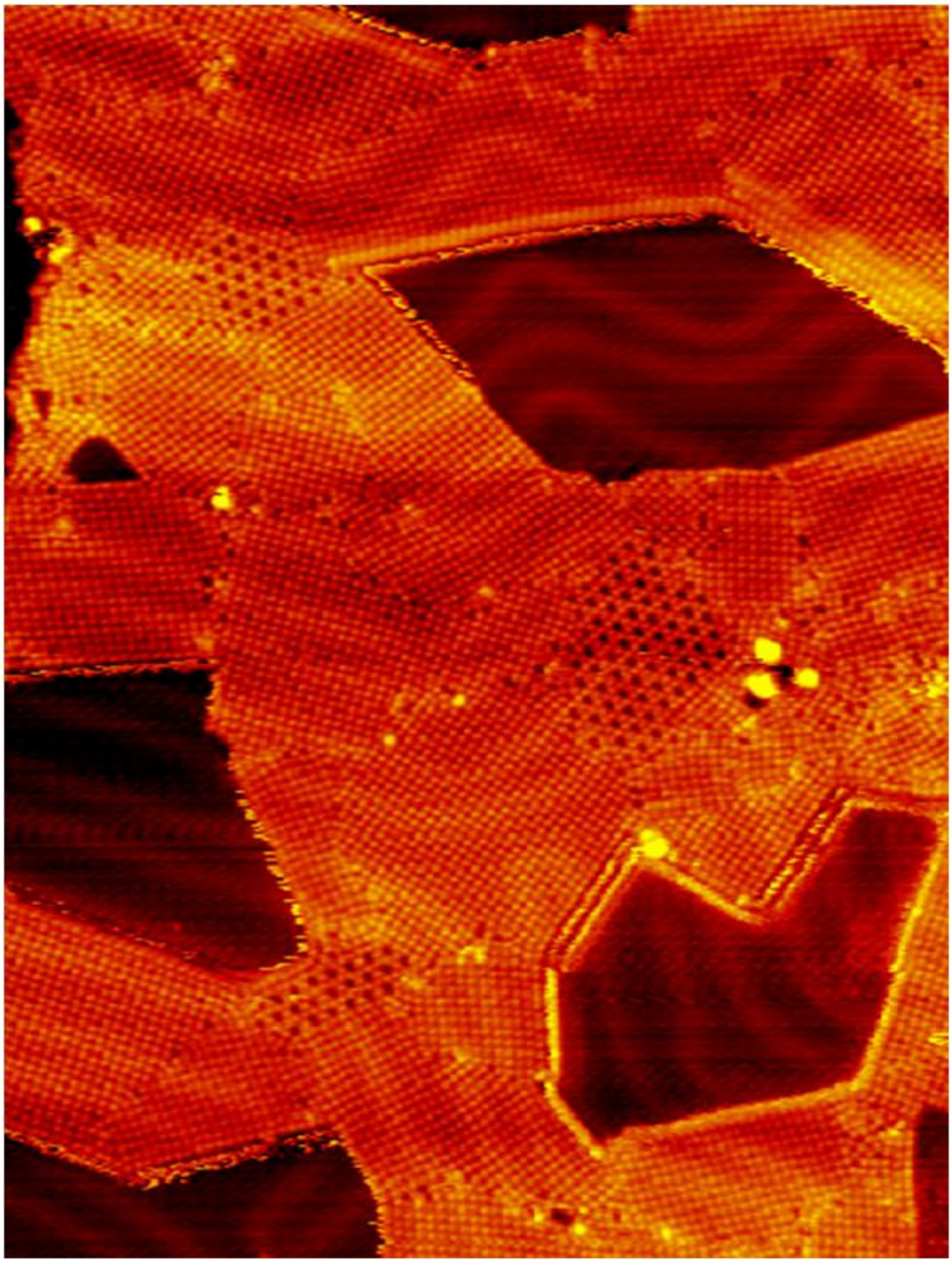

Figure 66. Different domains of a single STM image. 425Å x 529Å 0.6nA -2.2V

4.3.2 Evaporation of Fe atoms into oxalic acid sample.

Figure 67 shows the morphology of the surface after depositing submonolayer amounts of Fe on top of the oxalic acid layer. A number of Fe islands nucleated at the elbows of the herringbone reconstruction are clearly observed. Thus, the Fe atoms do not spontaneously react with the oxalic acid molecules. However, trying to promote the reaction through moderate annealing lead to a complete desorption of the oxalic acid molecules.

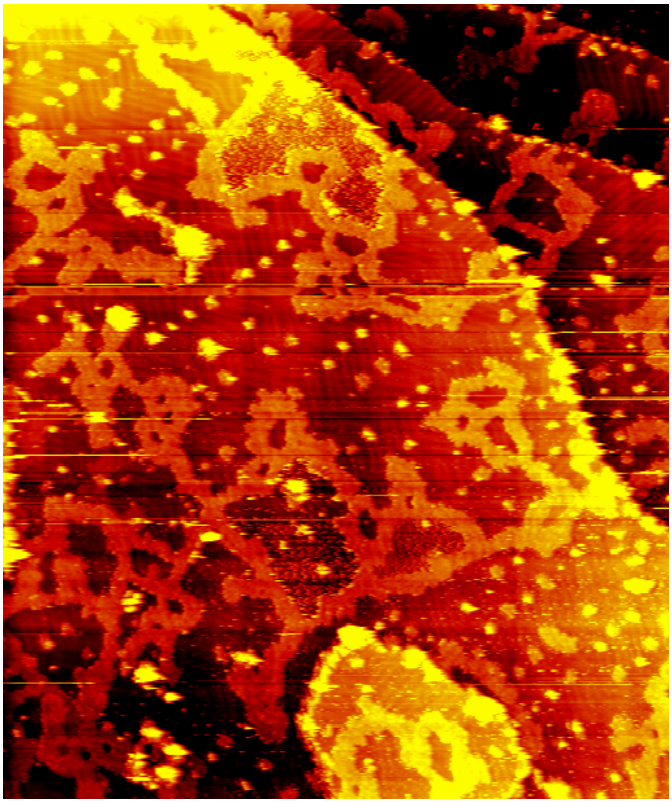

Figure 67. Different domains of a single STM image. 425 Å x 529Å 0.8nA 1.25V

Thus, it seems that the reaction between oxalic acid and Fe to form iron oxalates must be thermally activated. We will try then some other surface with a stronger molecule-surface interaction, in order to prevent desorption to take place before the formation of the Fe-oxalate.

4.3.3 Oxalic Acid on Cu (111)

4.3.3.1 Room temperature deposition.

We have evaporated at 40ºC molecules from glass crucible into clean surface held at RT. All of the images were taken at LT 80 K.

After sublimation of small amount (0.2 ML) oxalic acid onto the clean copper (111) surface we could observe the formation of a number of regular triangular structures at the step edges (see Figure 68).High resolution images show that the edges of the triangles are composed of small rounded spots separated ~5 Å. In addition, a number of disordered and shapeless bright structures are found close to these triangles.

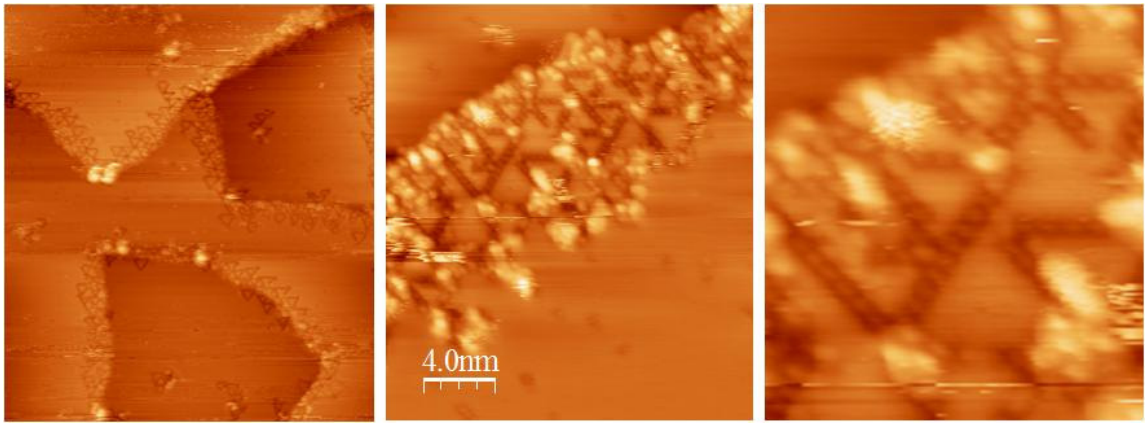

Figure 68. STM images and XPS spectrum of evaporation of 0.2 ML of oxalic acid onto clean Cu (111) surface. 0.8 nA -2.1V

We believe that these triangles are the result of the decomposition of the oxalic acid at the steps of the surface. It is known that, in bulk form, oxalic acid decomposes into formic acid and canrbon dioxide according to the formula

$$C_2O_4H_2 \rightarrow CO_2 + CO_2H_2$$

The spots within the edges of the triangular structures would then be formic acid molecules, while the irregular 3D islands would be the decomposition of carbon dioxide into atomic carbon. Besides the XPS data that will be shown below, the conclusions are supported by previous experiments of the adsorption of formic acid onto the Cu(111) surface (84)(see Figure 69). STM images show that in this case formic acid adsorbs at the steps edges forming triangular structures with edges composed of lines of formic acid molecules.

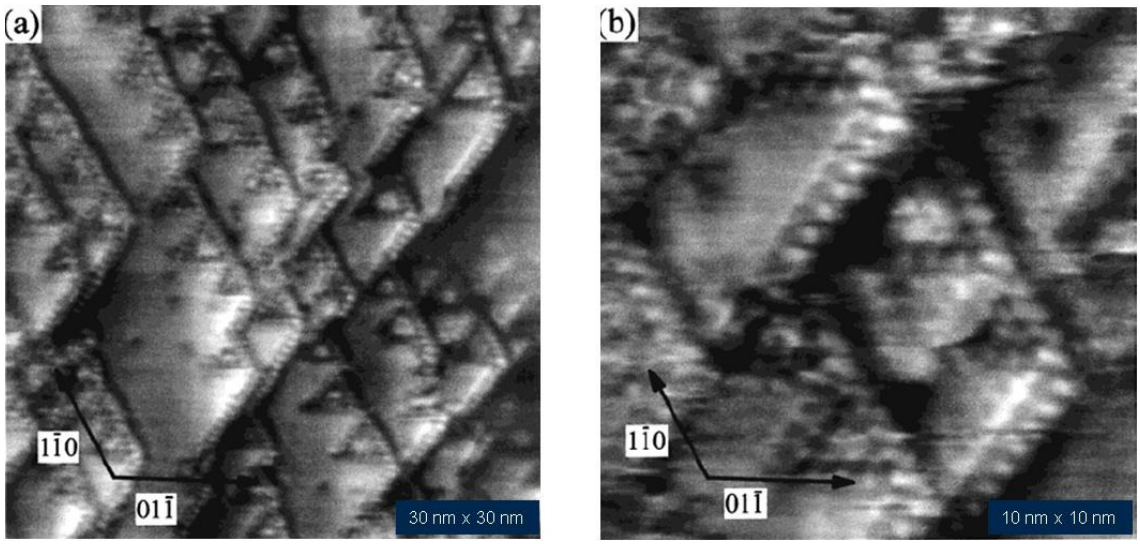

Figure 69. Formate molecules onto Cu(111) surface.

When increasing the amount of sublimated molecules the STM images show the appearance of a new ordered structure with an hexagonal arrangement (Figure 70 a) b) c)). This ne w structure is the one that finally dominates the surface morphology, while the former triangular shapes are confined to the steps edges of the copper surface and the edges of the hexagonal islands. Figure 70 d) shows an enlarged view of the hexagonal islands.

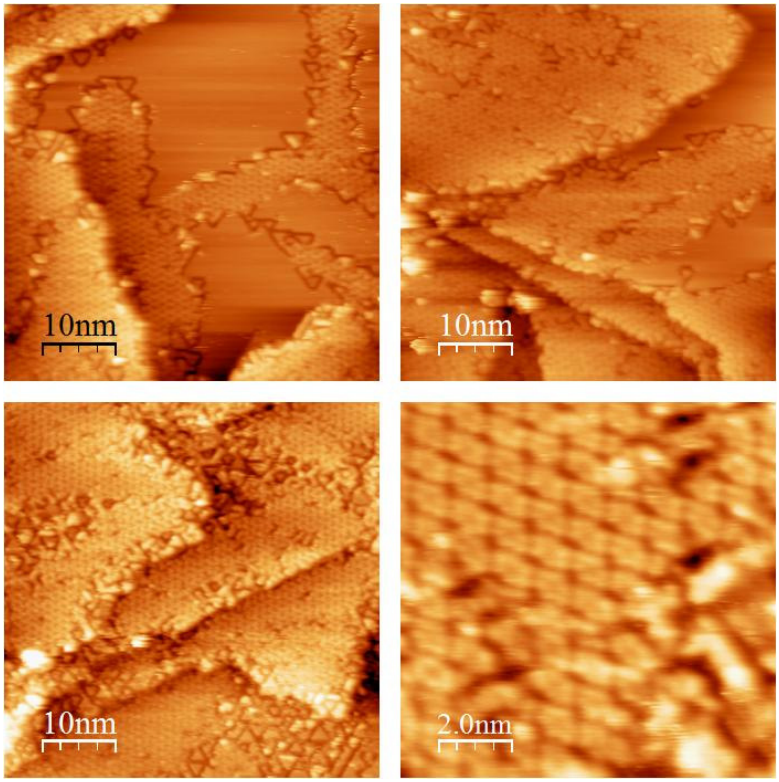

Figure 70. STM images of evaporation of oxalic acid onto clean Cu (111) surface a) 0.6nA -1.9V,b)0.8nA -1.7V, c)0.7nA – 2.1Vd)07nA -2.1V

.

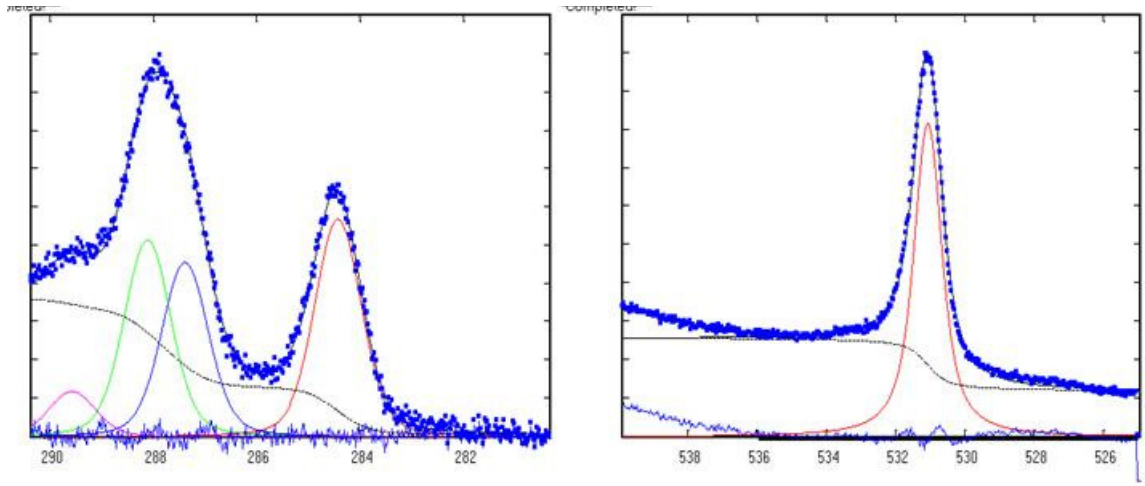

Figure 71. XPS spectra images of evaporation of 0.8 ML of oxalic acid onto clean Cu (111) surface.

From the XPS data of the O1s peak we can deduced that molecules at this stage are fully deprotonated. The existence of just one peak at 531.5 eV indicates the existence of only one species of oxygen atom, while, as we shall see below, two peaks can be distinguished for the full molecule. The analysis of the C1s peaks shows the existence of at least four components at 284.4, 287.4, 288.1 and 289.2 eV. This last one is a shake-up satellite, so we'll exclude it from the following analysis. The peak at 284.4 eV is usually associated to the existence of either -C-C- chains or atomic C on the surface. Since carboxylic acid does not have -C-C- chains, we attribute it to atomic C created during the decomposition of the oxalic acid molecule. The two remaining peaks at 287.4 and 288.1 eV correspond then to C in the formate and the oxalate molecule, respectively. The evolution of the individual components as a function of coverage (Figure 71) shows that the peak at 288.1 is the one finally dominating the C spectra, and should the correspond to oxalate molecules in the hexagonal ordered areas.

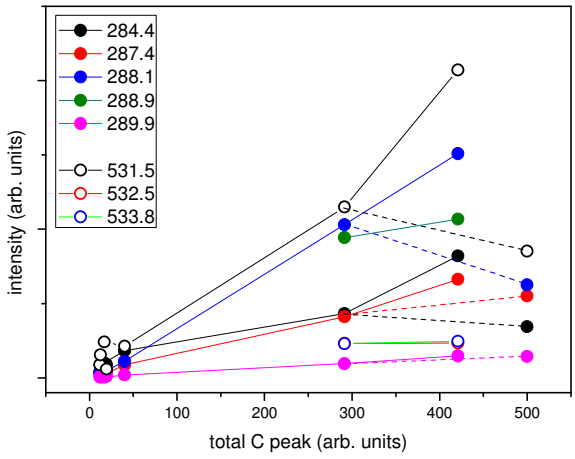

Figure 72. Evolution of the area of the individual XPS components as a function of the coverage (given as a function of the area of the total C peak).

From the O1s NEXAFS data we can deduced that oxalate molecules is adsorbed in planar configuration. The peaks at 533 and 536 3eV correspond to the π bonds of the oxalate molecule and the peaks at 543 and 550 eV to the σ bonds. With increasing the angle of incidence of the light with respect to the surface the intensity of the signal coming from the π bonds increases, while those coming from the σ bonds decrease accordingly, what suggests a planar adsorption geometry.

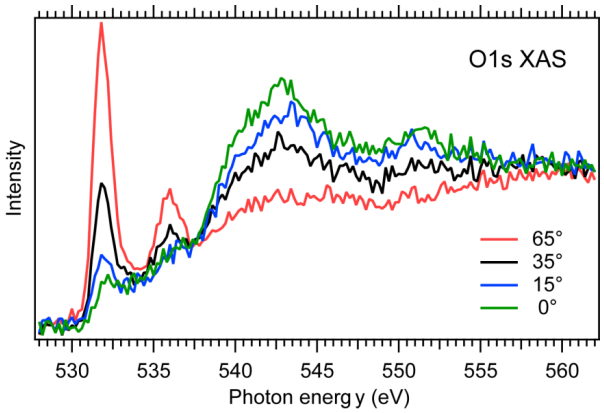

Figure 73. XAS spectra taken after thethe evporation of 0.8 ML of oxalic acid onto clean Cu (111) surface.

When increasing the coverage a second layer starts to grow (Figure 74). At this stage, a new broad feature in the O1s spectrum appears at higher binding energy. This structure can be decomposed into two peaks at 532.5 and 533.8 eV, corresponding the two O atoms in the carboxylic acid (532.5 eV for the carbonyl atom and 533.8 eV for the hydroxyl atom), and thus indicating that second lower molecules are adsorbed intact. The peak at 531.5 eV remains unchanged, corresponding to O in first layer formate and oxalate molecules. Accordingly, in the C1s spectrum a new peak shows up at 288.9 eV, coming from the C atoms in the intact carboxylic acid.

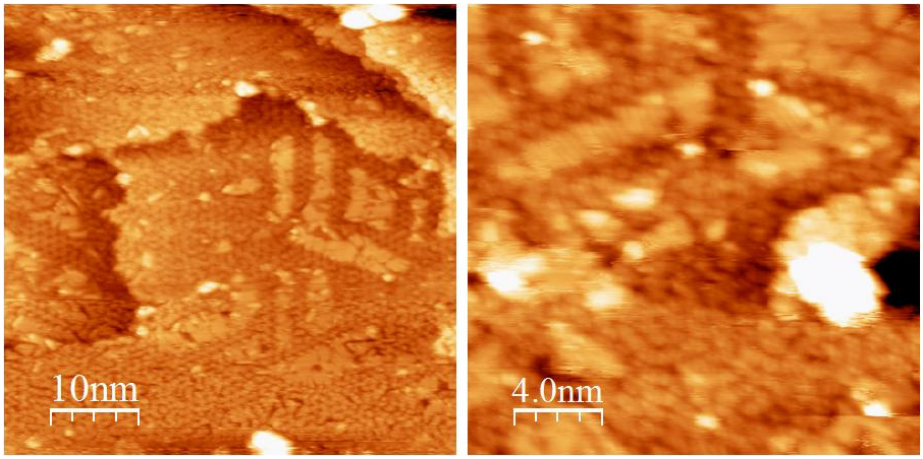

Figure 74. STM images of the evaporation of 1.2 ML of oxalic acid onto clean Cu (111) surface. a) 0.3nA -2.4V b) 0.3nA -2.4V

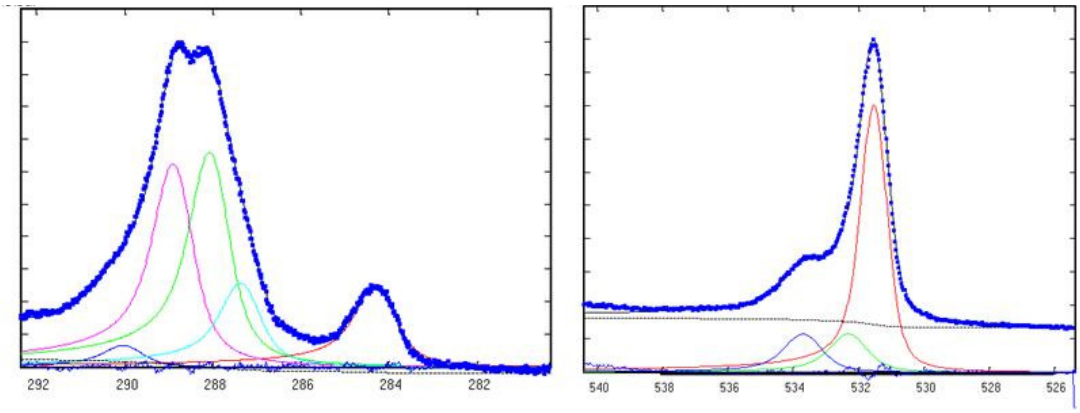

Figure 75. XPS spectrum of 1.2 ML of oxalic acid onto clean Cu (111) surface.

4.3.3.2 Annealing.

For higher coverage, STM images show the formation of a mostly disordered overlayer. (Figure 76a). The effect of annealing this surface to 40 ºC and 60 ºC are shown in Figures 76b and 76c, respectively. An enlarged view of the final state is shown in 76d.

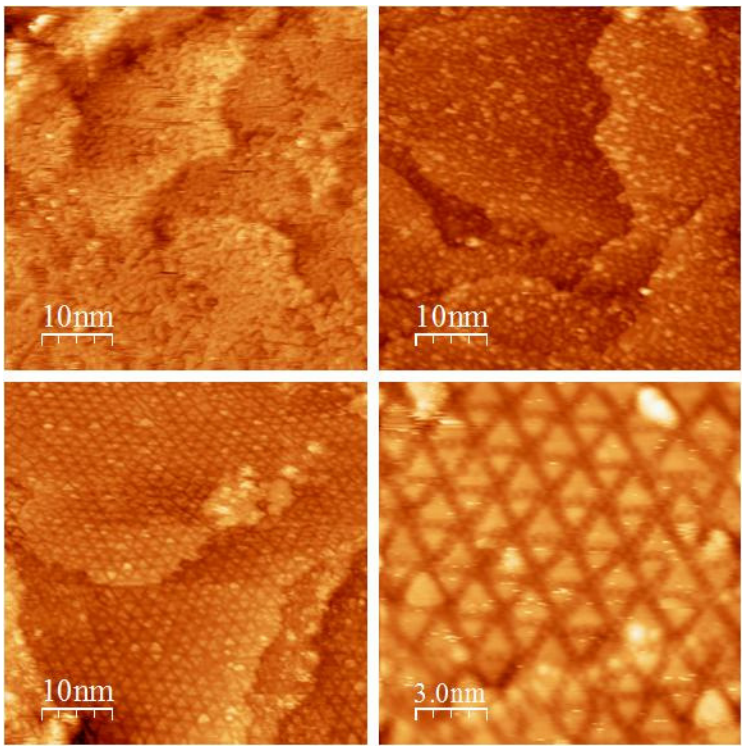

Figure 76. STM images of evaporation of 1.2 ML of oxalic acid onto clean Cu (111) surface and flash annealing a) 0.4nA -2.1V b) 0.7nA -2.2V c) 0.3nA -2.2V d) 0.3nA -2.2 V

The surface is covered now by an ordered array of triangular structures that remind of the ones found during the early stages of growth, except that now they extend all over the surface. By comparing the XPS spectra (Figure 77) with those taking before annealing (Figure 75), we can see the disappearance of all those features associated with the intact molecule, indicating the desorption of the second monolayer. In addition, the intensity of the peak at 287.4 eV increases with respect to the peak at 288.1, which indicates that annealing induces the decomposition of oxalate molecules into formate molecules.

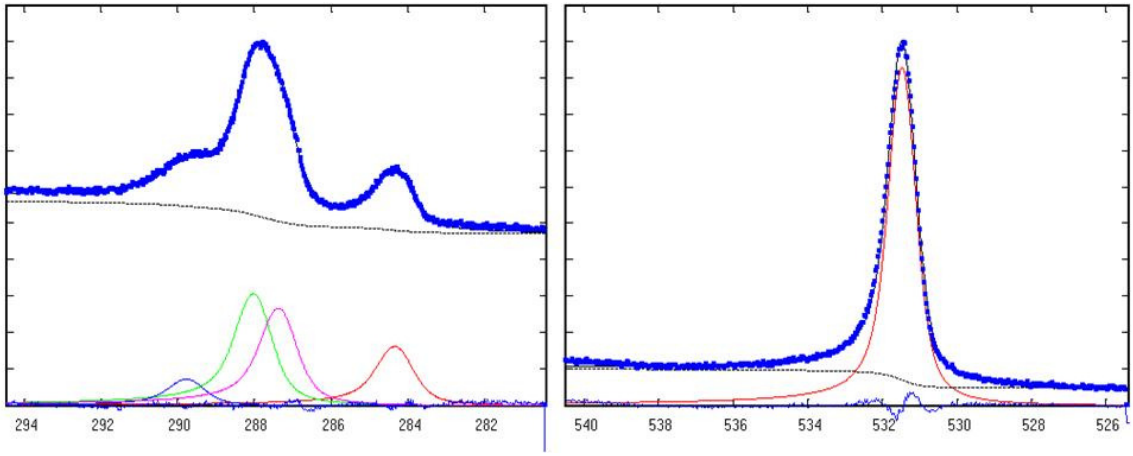

Figure 77. XPS spectrum of evaporation 1.5 ML of oxalic acid and annealing till 60 ºC

4.3.3.3 Iron deposition.

The purpose of the experiment was dosing iron atoms and create an Fe-Ox For this reason we have been evaporated a small amount of iron onto a freshly deposited 0.5 ML of molecules (Figure 78a). The STM images (Figure 78b) show that this process completely destroys the order of the hexagonal islands, which now look irregular and with no noticeably inner order. The triangular structures, on the other hand, remain almost completely intact. The modification of the oxalate structure upon Fe deposition points towards the incorporation of metal centers within the oxalate islands to readily form metal-oxalate coordination networks,, creating disordered patches of Fe-oxalate coordination networks.

The order within this Fe-oxalate islands is greatly improved by a gentle annealing up to 373 K for 10 minutes. The STM images (Figures 78c, 78d, Figure 79) show that the islands have now an ordered honeycomb structure. The lattice parameter of the network, i.e. the hole-hole distance, is 0.77 nm. The side of the hexagonal cell is thus about 0.5 nm long.. This structural motif has been widely described for the coordination chemistry of the 1st row transition metals with the oxalate ligand. A tentative model for this new Fe-MOCN is displayed in Figure xx. According to it, each Fe atom is coordinated by three bis-bidentate fully deprotonated 2-oxalate bridging ligands, thus resulting in 2D honeycomb lattice composed of 6-fold coordinated Fe

atoms. Figure xx shows a detailed view of the honeycomb network together with a comparison between the proposed structure and the the crystal structure of the [FeFe(ox)3] network asextracted from single crystal x-ray diffraction experiments performed on a bulk material.

Unfortunately, as we have seen and Figure 78d shows, the creation of the ordered 2D network through the annealing procedure by the decomposition of oxalate into formate, altough further experiments are being developed to maximize the MOCN area.

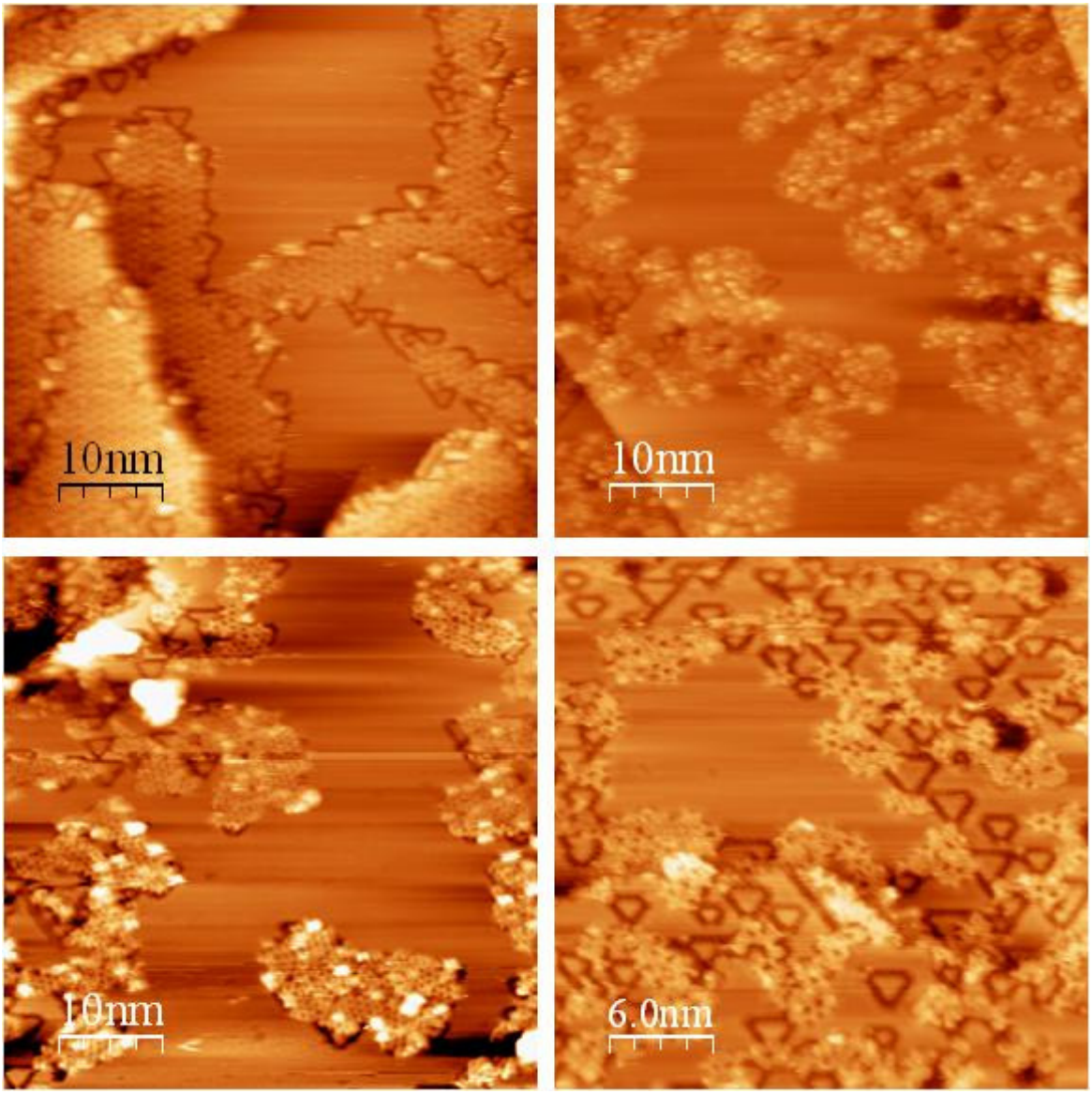

Figure 78. STM images of evaporated molecules a and onto molecular layer dosing iron atom b and subsequent annealing c.a) 0.6nA -1.9V b) 0.3nA 1.7V c)0.6nA 1.8V

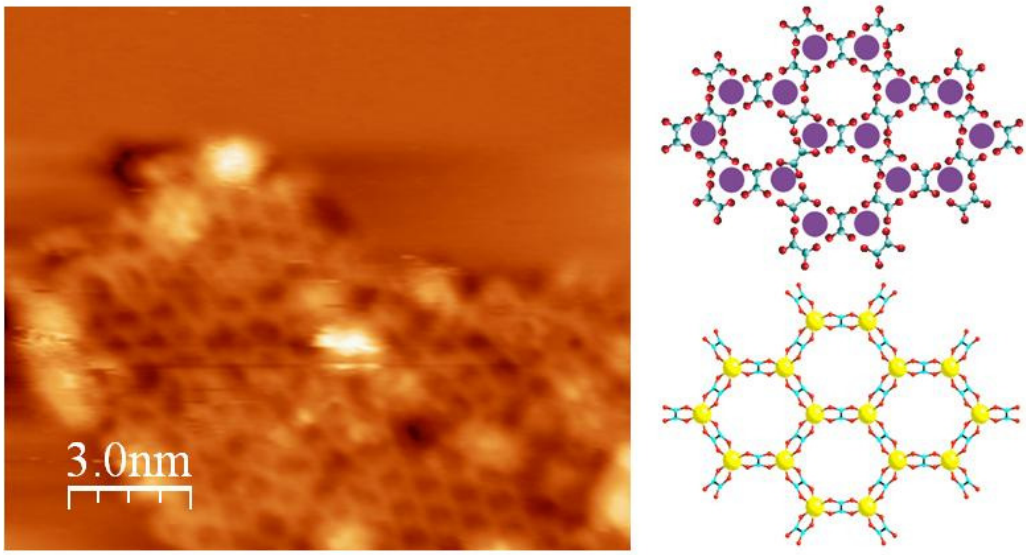

Figure 79. A honeycomb structure after dosing ion atoms into oxalate sample. 0.6nA 1.8V

4.3.4 Oxalic Acid on Cu (100).

4.3.4.2 Room temperature deposition.

At the early stages of evaporation at room temperature on the clean copper (100) surface, STM images (Figure 80a) show the steps decorated by molecules and some small islands on the terraces. The height of the islands is around 1,2 Å, which is in agreement with a flat adsorption of the molecules. When increasing the coverage (Figure 80b) the molecules tends to grow to complete the first monolayer. Only one species is visible in the STM images, which seems to discard here the decomposition of the molecule that takes place at the steps of the Cu(111) surface.

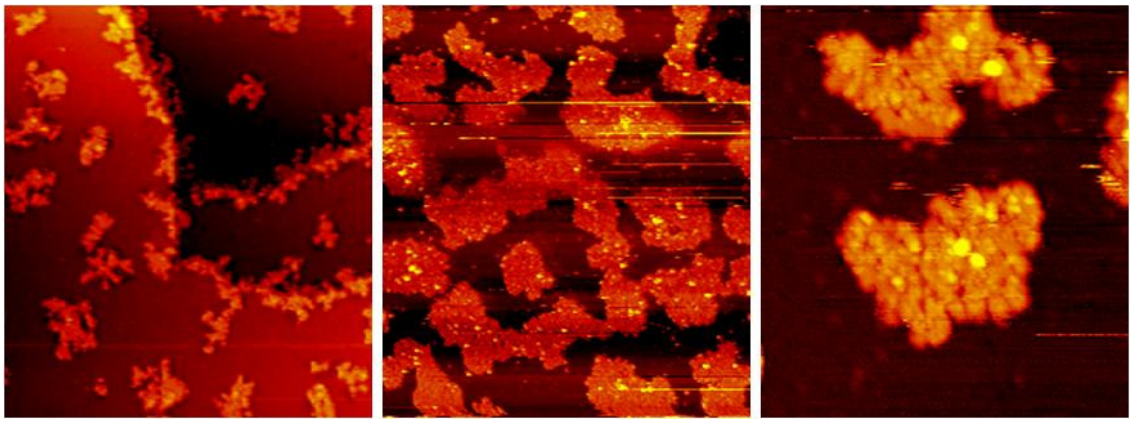

Figure 80 STM images of different time of evaporation of oxalic acid onto clean Cu 100 surface.a)1140Å x1276Å 0.14nA -2.97V b)1140Å x 1276Å 0.2nA -2.7V c)342Å x 383Å 0.2nA -2.7V

Taking into account the disordered appearance of the islands we can assume the absence of the formation of hydrogen bonds between molecules, which seems to indicate again the deprotonation of the oxalic acid molecule.

4.3.4.3 Annealing.

After annealing to 360 K the molecules self-assemble into a rectangular pattern aligned with the high symmetry directions of the substrate.

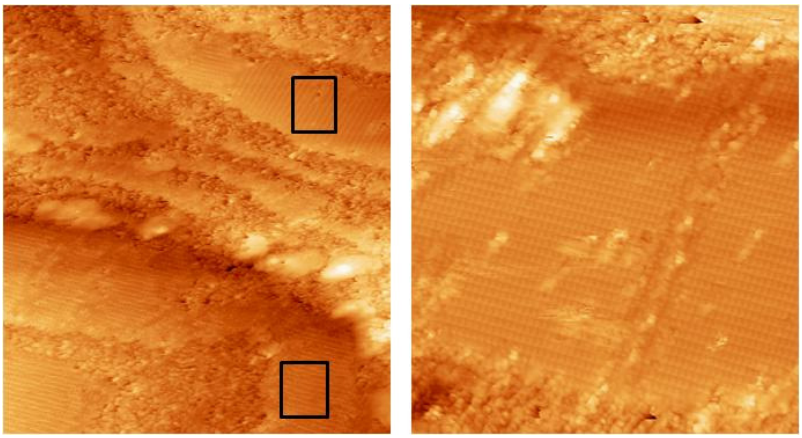

Figure 81.STM images of oxalic acid onto Cu 100 surface after flash annealing to 80º C. 425Å x 600Å 0.7nA 2.2V

As shown in Figure 81. there are two different domains at the surface which are rotated 90º with respect to each other. The matrix describing the epitaxial relationship for this two domains are.

Matrix $\begin{pmatrix} b_1 \\ b_2 \end{pmatrix} = \begin{pmatrix} \frac{5}{2} & 0 \\ 0 & 2 \end{pmatrix} \cdot \begin{pmatrix} a_1 \\ a_2 \end{pmatrix}$ $\begin{pmatrix} b_1 \\ b_2 \end{pmatrix} = \begin{pmatrix} 2 & 0 \\ 0 & \frac{5}{2} \end{pmatrix} \cdot \begin{pmatrix} a_1 \\ a_2 \end{pmatrix}$

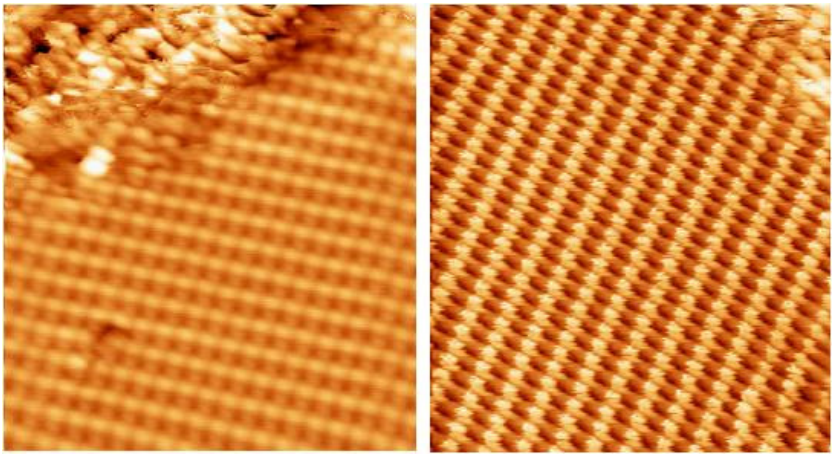

Figure 82. Two different domains with respect to the directions of the surface. 171Å x 191Å 0.7nA 1.6V

Taking a closer look to the ordered areas we can distinguish two different species, bright and dark spots. According to the literature, at this temperature the molecules are fully deprotonated,. The deprotonated carboxylic groups form ligands which can be linked to the Cu atoms from the surface. The copper atoms come from steps or kinks because of their high mobility at this temperature and these reactive atoms may interact with the deprotonated molecules to form metal-organic coordination bonds. Thus, we assume that after annealing to 360 K a Cu-oxalate metal coordination bond is formed.

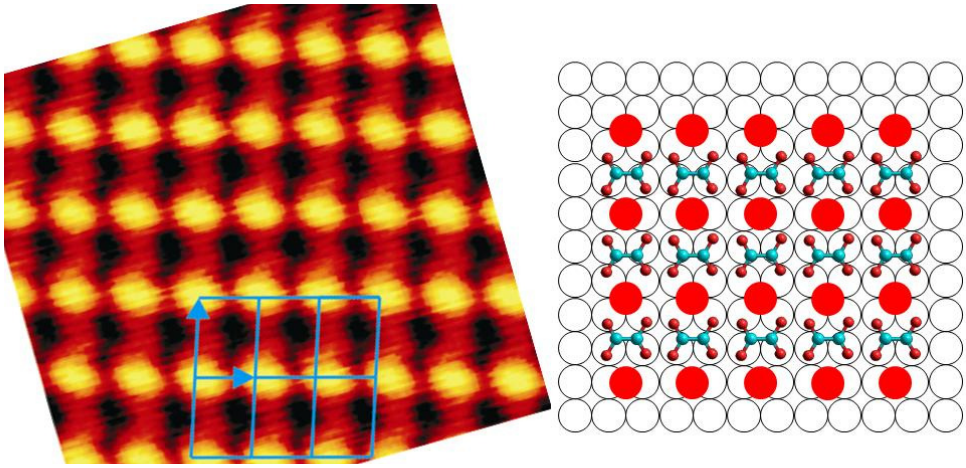

Figure 83. A model for the two adsorption domain. 55 Åx38Å 1.44nA 0.9V

An schematic model of this MOCN is shown in Figure 84. In here, each copper adatom is coordinated to four oxygen atoms of two different oxalate molecules, forming copper-oxalate coordination bonding. The distance between the copper adatom and oxygen atom is around 2 Å, and with adjacent copper atom is 2 x 2.56 Å 5.1Å and 2.5x2.56 6.4 along the high symmetry directions of the substrate 110 and -110.

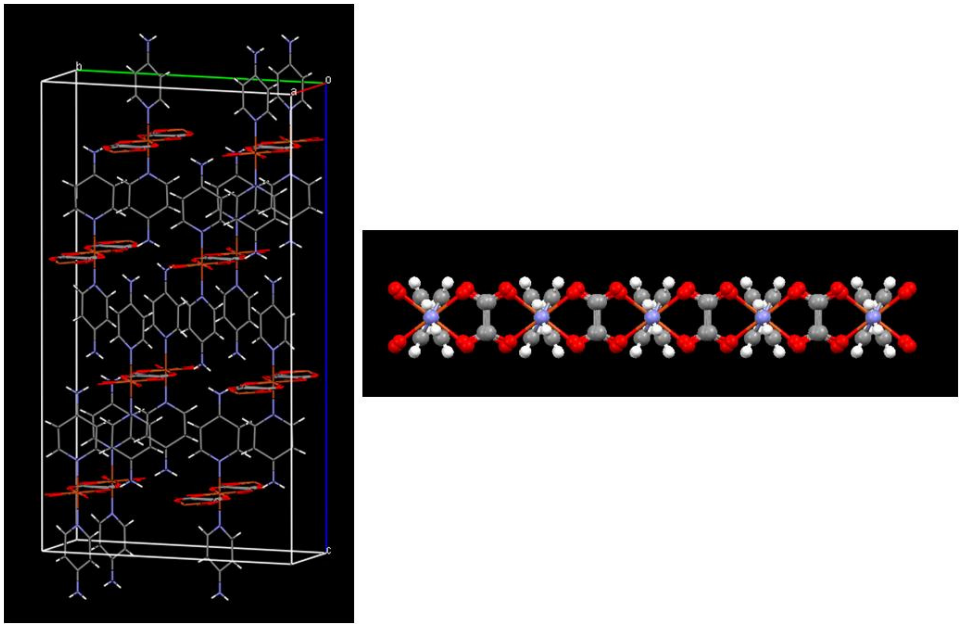

Figure 84. A schematic model of the bulk structure of a Cu-oxalate compound.

Upon further annealing to 90º C we observe a new change in the surface morphology (Figure 85).), which now displays lines of dots (bright and dark, with an apparent height difference of 0.3 Å), following the high symmetry directions of the surface. The distance between dots is 5.0 Å. A population analysis of the dots shows that 62% are bright and 38 % dark, but the number of dark dots increases proportionally to the annealing time. As shown before on Cu(111), these behavior can be attributed to the decomposition of oxalic acid into. Besides, previous works report the decomposition of small carboxylic molecules at even lower temperatures (85) (86) (87) (88) (89) (90). With this in mind, Figure 85 can be considered as a mixture of oxalate (bright dots) and formate ones (dark dots), where the amount of formate increases with the annealing time. Thus, at this temperature, oxalate molecules have started to decompose breaking the former Cu-ox coordination bonds.

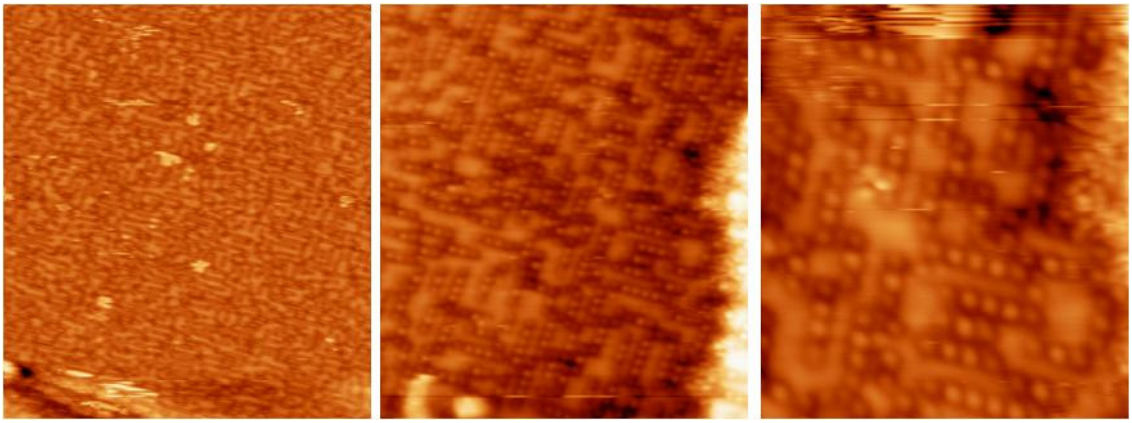

Figure 85. STM images after flash annealing till 90ºC a) 228 Åx 255Å 0.9nA 1.9V b)170 Å x 240Å 1.3 nA 0-9V

4.3.4.4 Iron deposition.

Although 2D [Cu-ox]n motifs are spontaneously formed when oxalic acid is deposited on Cu(100), the main goal of the conducted experiments was to create Fe-MOCN. We have taken the three different phases of oxalic acid on Cu(001) as a starting point, which are: the disordered islands (Figure 80), the 2D [Cu-ox]n system (Figure 82) and the oxalate/formate phase (Figure 85). No matter which one was employed, once 0.2-0.3 ML of Fe were evaporated at room temperature onto the molecular layer (to avoid any possible surface intermixing between Fe and Cu at room temperature[26]), the result was always a mainly disordered pattern. However, after annealing at temperatures higher than 373 K, a completely new phase appeared. As in the case of the Cu(111) surface, this new phase exhibits a honeycomb motif (slightly distorted now) which coexists with the oxalate/formate phase described above (Figure 85). Moreover, if in a first step 0.7 ML of Fe are directly evaporated on Cu(001) and then 0.5-0.9 ML of oxalic acid are evaporated on top of the Cu-Fe mixture, a disordered pattern, which evolves towards the new iron-based honeycomb network once the surface is annealed up to 373 K, is observed.

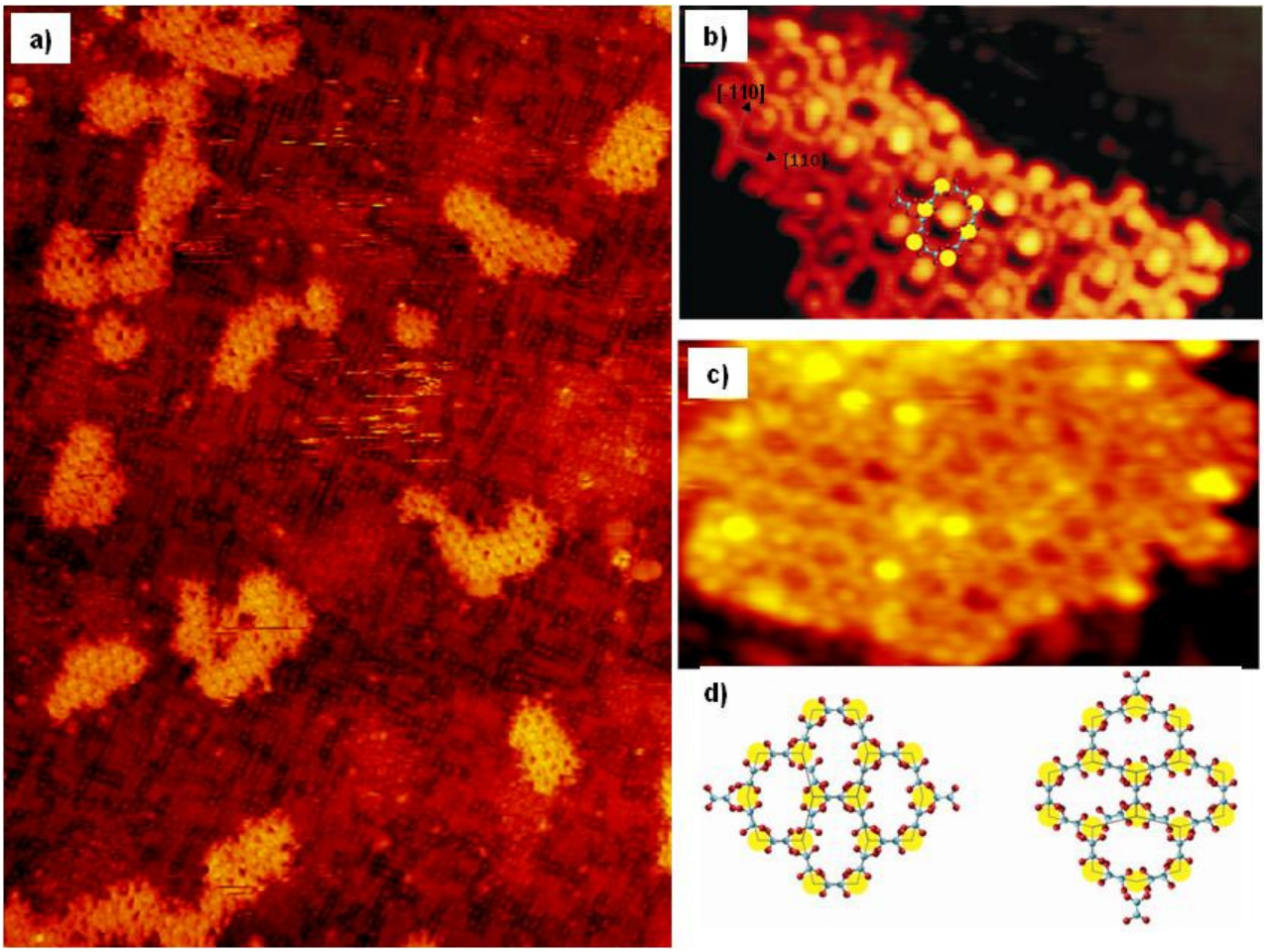

Figure 86. A structural model for iron oxalate superimposed onto STM image. a)425Å x 529Å b) 91Å x 41Å 0.9nA 1.25V c)91Å x 41 Å 0.9nA 1.3V

Taking a closer look at Figure 86, it is possible to distinguish individual molecules, but not Fe atoms, a difficulty that has been already reported. (91) Geometrically, this distorted honeycomb has four sides of 5.3 Å and two shorter sides of 5.2 Å. The internal dihedral angles are 104º and 152º, quite different from the expected value of 120º for a perfect honeycomb. In addition, each honeycomb island has the short sides aligned with the [110] or the [-110] directions, which results in two different domains (α and β), related by a rotation of 90º. A tentative model for this new Fe-MOCN, similar to the one found in the Cu(111) case, is displayed in Figure 86.

4.4 Conclusions

Our purpose of the experiment was to create large ordered pattern composed of oxalic molecules and iron atoms. We have been able to find conditions for growing a honeycomb structures but we have not been able to create large areas of ordered patterns because of decomposition of molecules at 80ºC.

We have proposed fabrication of MOCNs with the smallest possible ligand. For the Au(111) surface it was not possible to create MOCNs because of too less reactivity of the surface. The Kagome and oblique phases are found.

For the Cu(111) and Cu(100) surfaces we could obtain MOCNs with codeposition of oxalic molecule with iron adatoms. Nevertheless, to grow of large islands of Molecular Organic Coordinetion Networks is difficult, we could synthesis just small patches.

Summary

In this summary we conclude the experimental part of the thesis. The investigations were conducted at UHV chambers using Scanning Tunneling Microscopy and X ray Photoemission Spectroscopy for the organization characterization of the organic compounds at the different metallic surfaces. In particular we have been focused on the compounds which consists metal-organic coordination bonding. As well already at the structure of the molecule or adding to the molecule of metal ions for forming those coordination structures.

In the chapter three we have investigated large organic macrocycle compound as Zn porphyrin. In this case we have shown the self assembly of porphyrin molecule into large 2D tubes linked together by oxygen. The STM and XPS experiments were done into to different substrates with different reactivity as Cu (100) and Au (111). The main role in the organization at the surface plays a Zn atom which is able to coordinate an oxygen and because of this linking to self assembly. In comparison to the metal-organic porphyrin we have shown the date taken from the empty porphyrin resolving a flat adsorption at the surface, which conclude that the Zn coordinated to the oxygen leads to the formation 2D structures.

Chapter four was dedicated as well to the large organic compounds. In this case we have been investigated subphthalocyanines with different ligands attached into the macrocycle ring (based on boron atom) or with different atoms inserted into the outer phenyl rings on Cu (111) surface. The main role in the structure of the molecule is related to the cone shape of the compound because of the high dipole moment of the boron ligand axis. Due to this shape molecules can adsorbed at the surface in different way: as a honeycomb structure made or into two layers triangular islands. The honeycomb structure is forming due to the strong molecule-substrate interaction in contrary the triangular island are forming due to the molecule-molecule interaction. Those structure mentioned above are created by chlorine subphthalocyanine. For the other molecules for example which have attached fluorine atom into outer phenyl ring we have found small honeycomb structures. The best results we have obtained for the ligand boron-chlorine. The studies were done by STM.

The last experimental chapter consists studies on the smallest carboxylic compound: oxalic acid. As well for this compound the major role for the self assembly plays the coordination bonds. But for this molecule which consists in their structure just carbon, oxygen and hydrogen atoms we have sublimated molecules at Cu (100) surface and after obtaining some ordered structures dosing iron atoms into the substrate. In this way we are able to obtain a 2D honeycomb patches where the oxygen atom from the carboxylic group is linked to the iron atoms. The structures were investigated by STM and for further chemical information we have conducted XPS and NEXAFs experiments.

The main goal of the thesis was to present the importance of the metal-oragnic bonding for the self assembly of the molecules. It was shown different ordered structures related to the metal-ligand interaction.

Conclusiones

Esta tesis trata del crecimiento de estructuras manométricas de moléculas orgánicas (porfirinas, subftalocianinas y acido oxalico) en UHV, mostrando que bajo ciertas condiciones de crecimiento se obtienen patrones auto-organizados. Los resultados obtenidos contribuirán al desarrollo de los futuros aplicaciones en nanotecnología.

En el capitulo tres se muestra el crecimiento de la porfirina que lleva un atomo de zinc en el anillo aromatico. Gracias a esta propiedad hemos podido crecer nanotubos de moleculas unidas a través de moléculas que contienen oxigeno sobre superficies metalicas como cobre e oro. Desde estudios del STM y XPS hemos sacado conclusiones que moléculas no están adsorbidas planas en el metal gracias el enlace de coordinación entre atomo zinc y oxigeno pueden formarse en grandes estructuras de forma tubular.

En el capitulo siguiente hemos estudiado la adsorbcion de las subftalocianinas sobre cobre (111). Las moléculas se autoorganizan en grandes islas de honeycomb y también bajo distintos condiciones de evaporacion en islas triangulares de dos mono capas. El crecimiento era estudiado por STM. La mayoría de los experimentos sobre subftalocinainas ha sido con el especie que llevaba el cloro como pegado al anillo aromatico.

Finalmente, en el capitulo cinco hemos observado el ordenamiento de moléculas de acido oxálico sobre cobre e oro con y sin Fe presente estudiado por el STM y XPS. Las moléculas de acido oxálico junto con hierro añadido en la superficie forman estructutras parecidas a honeycomb donde enlace hierro-oxygeno tiene la gran importancia.

De todos los estudios sobre moléculas que pueden tener un enlace metaloorganico hemos visto que tienen posible importancia en futuros aplicaciones.

El enlace metalorganico diriga la adsorcion de las moléculas en la superficie en distintas nanostructuras.

Publications

Authors: David Ecija, Marta Trelka, Christian Urban, Paula de Mendoza, Eva Mateo-Marti, Celia Rogero, Jose A. Martin-Gago, Antonio M. Echavarren, Roberto Otero, Jose Maria Galego and Rodolfo Miranda
Title: Molecular Conformation, Organizational Chirality and Iron Metalation of Meso-Tetramesitylporphyrins on Copper(100)
Journal: J.Phys. Chem C
Reference: 2008, 112 (24) pp 8988-8994

Authors: David Ecija, Marta Trelka, Christian Urban, Paula de Mendoza, Antonio Echavarren, Roberto Otero, Rodolfo Miranda and Jose Maria Gallego
Title: *Templeted growth of an ordered array of organic bidimensional mesopores*
Journal: Applied Physics Letters
Reference: 92, 223 117(2008)

Authors: Christian Urban, David Ecija, Yang Wang, Marta Trelka, Iulian Preda, Antje Vollmer, Nicolas Lorente, Andres Arnau, Manuel Alcami, Leonardo Soriano, Nazario Martin, Fernando Martin, Roberto Otero, Jose Maria Gallego and Rodolfo Miranda
Title: *Growth and Structure of Self-assembled Monolayers of a TTF Derivative on Au(111)*
Journal: J.Phys.Chem C
Reference: 2010 114(14) pp 6503-6540

Authors: Tzu-Chun Tseng, Christian Urban, Yang Wang, Roberto Otero, Steven L.Tait, Manuel Alcami, David Ecija, Marta Trelka, Jose Maria Gallego, Nian Lin, Mitsuharu Koruma, Ulrich Starke, Alexei Nefedov, Alexander Langner, Christof Woell, Maria Angeles Herranz, Fernando Martin, Nazario Martin, Klaus Kern and Rodolfo Miranda
Title: *Charge-transfer-induced structural rearrangements at both sides of organic metal interfaces*
Journal: Nature Chemistry
DOI: 10.1038 /NCHEM.591

Authors: Marta Trelka, Anais Medina, David Ecija, Christian Urban, Christian Classenes, Roberto Otero, Jose Maria Gallego, Tomas Torres and Rodolfo Miranda
Title: *Epitaxial growth of SubPc based nanocrystals*
Journal: JACS
Reference: Submitted

Authors: Marta Trelka, Cristina Isvoranu, Carlos Martí-Gastaldo, David Écija, Christian Urban, Evren Ataman, José María Gallego, Joachim Schnadt, Roberto Otero, Eugenio Coronado, and Rodolfo Miranda
Title*: The Densest Iron Coordination Network Based on Carboxylate Ligands*
Reference: In preparation

Authors: Gonzalez-Moreno, Ruben; Sanchez Sanchez, Carlos; Ruiz-Bermejo, Marta; Trelka, Marta; Otero, Roberto; Cossaro, Albano; Floreano, Luca; Martin-Gago, Jose; Rogero, Celia
Title: *Coordination reaction of porphyrins with surface metal atoms at room temperature*
Journal: JACS
Reference: Submitted

Acknowledgments

For having this thesis it was many people involved in whose I would like to gratitude.

First, to my supervisors: **Dr. Roberto Otero** and **Dr. José María Gallego** for their help in all of those years in many ways, not just in science but also for their talks and always for having time for me.

To Prof. Rodolfo Miranda, head of the Surface Science Laboratory of giving me opportunity of doing PhD at Surface Science Laboratory.

To TIREMISU team: Roberto, Josemari, David, Christian, Jonathan, Fabiola and a new student Luigi. It was a pleasure to work with you during all those long hours in the lab. In this place I would like to give special thanks to Dr. David Écija for his help and contribution to this thesis.

And to all of the members of the Surface Science Laboratory.

To the people whose I collaborated: to the groups of Dr. José Angel Martín - Gago, Prof. Antonio Echavarren, Prof. Tomas Torres and Prof. Eugenio Coronado.

To all the members of the Early Stage Researcher Training Network MONET, specially to Achim, Cristina and Evren from Lund University where I performed XPS measurements.

I would like to thank to my friends in Madrid and Poland (Yami, Michela, Desiré, Gina, Alejandro, Inma, Youseli, Anaïs, Agnieszka, Aga, Dominika, Monika, Jędrzej).

And of course, I would like to give special gratitude to my family, my parents and brother for being with me all those years and supporting in every moment.

Thank you,

Marta

References

1. *Scanning Tunneling Microscopy-From Birth to Adolescense.* **G.Binning, H.Rohrer.** Zurich Research Laboratory : Nobel lecture, 1986.

2. *Scanning tunneling microscopy studies of metal surfaces.* **F.Besenbacher.** 1737-1802, s.l. : Rep.Prog.Phys., 1996, Vol. 59.

3. **Barth, J. V.** 375-407, s.l. : Annu. Rev. Phys. Chem., 2007, Vol. 58.

4. **Roberto Otero, Maya Lukas, Ross E. A. Kelly, Wei Xu, Erik Lægsgaard, Ivan Stensgaard, Lev N. Kantorovich, Flemming Besenbacher.** 5861, s.l. : Science, 2008, Vol. 319.

5. *Electron spectroscopy study of the initial stages of iron phthalocyanine growth on highly oriented pyrolitic graphite.* **C.Isvoranu, J.Ahlund, B.Wang, E.Ataman, N.Martensson, C.Puglia, J.Andersen, M.Bocquet, J.Scnadt.** 214709, s.l. : Journal of Chemical Physics, 2009, Vol. 131.

6. *Fullerenes from aromatic precusrsors by surface catalysed cyclodehydrogenation.* **G. Otero, G. Biddau, C. Sánchez-Sánchez, R. Caillard, M. F. López, C. Rogero, F. J. Palomares, M.A. Basanta, J. Ortega, J. Mendez, A. M. Echavarren, R. Pérez, B.Gómez-Lor and J. A. Martín-Gago.** 865-868, s.l. : Nature, 2008, Vol. 454.

7. **F. Schiller, J. Cordón, D. Vyalikh, A. Rubio, and J. E. Ortega.** 029702, s.l. : Phys. Rev. Lett. , 2006, Vol. 96.

8. **Barth, J., Costantini, G. y Kern, K.** 671, s.l. : Nature, 2005, Vol. 437.

9. *Caracterización estructural del crecimiento de siliciuros de hierro sobre Si(111) con microscopía de efecto túnel.* **Vázquez_de_Parga, A. L.** s.l. : Universidad Autónoma de Madrid, 1991.

10. **J.Tersoff, D.R. Hamann.** 805-813, s.l. : Phys. Rev. B, 1985, Vol. 31.

11. **J. Tersoff, D.R. Hamann.** 1998-2001, s.l. : Phys. Rev.B, 1983, Vol. 50.

12. **G.Binning, H.Rohrer.** 279-293, s.l. : IBM J.Res.Develop., 2000, Vol. 44.

13. **A.Kubby, J.J. Boland.** 61-204, s.l. : Surf.Sci.Rep., 1996, Vol. 26.

14. **www.specs.com.**

15. **H.Hert.** 983-1000, s.l. : Annalen der Physik, 1887, Vol. 31.

16. **A.Einstein.** 132-148, s.l. : Annalen der Physik, 1905, Vol. 17.

17. *Photoelectron Spectroscopy.* **S.Huefner.** Berlin-Heidelberg : Springer-Verlag, 1995.

18. *Atomic and nuclear analytical methods.* **Verma, H.R.** Heidelberg : Springer, 2007.

19. *Surfaces.* **Barnes, G.Attord and C.** New York : Oxford University Press, 1998.

20. *Fundamentals of surface and thin film analysis.* **Mayer, L.C. Feldman and J.W.** s.l. : Elsevier, Science Publishing CO. INC, 1986.

21. *Fundamentals of nanoscale film analysis.* **T.L.Alford, L.C. Feldman and J.W.Mayer.** New York : Springer, 2007.

22. *The Porphyrin Handbook .* **K. M. Kadish, K. M. Smith, and R. Guilard.** San Diego, CA : Academic Press, 2003.

23. *Biocoordination Chemistry .* **Fenton, D. E.** Oxford : Oxford Science Publications, 1997.

24. *Biochemistry .* **Stryer, L.** New York : W.H. Freeman, 1997.

25. **H. Imahori, K. Tamaki, D. M. Guldi, C. Luo, M. Fujitsuka, O. Ito, Y. Sakata, and S. Fukuzumi.** 2607, s.l. : Journal of the American Chemical Society , 2001, Vol. 123.

26. **Guldi, D. M.** 22 , s.l. : Chemical Society Reviews, 2002, Vol. 1.

27. **Sakata, H. Imahori and Y.** 537, s.l. : Advanced Materials, 2004, Vol. 9.

28. **B. A. Gregg, M. A. Fox, and A. J. Bard.** 1586, s.l. : Journal of Physical Chemistry, 1989, Vol. 94.

29. **Liska, M. Graztel and P.** s.l. : Estados Unidos de América, 1990), Vol. 4927721.

30. *Energy transfer and trapping in photosynthesis.* **van Grondelle, R., Dekker, J. P., Gillbro, T. & Sundstrom, V.** 1-65 , s.l. : Biochimica et Biophysica Acta (BBA) - Bioenergetics, 1994, Vol. 1187.

31. *Integration of Photosynthetic Protein Molecular Complexes in Solid-State Electronic Devices.* **Das, R. et al.** 1079-1083, s.l. : Nano Lett. , 2004, Vol. 4.

32. *Photosynthesis.* **McGraw-Hill.** 469, s.l. : Encyclopedia of Science and Technology, 2007, Vol. 13.

33. *Oxford dictionary of biochemistry and molecular biology.* **Smith, A. L.** 508, s.l. : Oxford University Press, 1997.

34. *Prokaryotic photosynthesis and phototrophy illuminated.* **Frigaard, D.A. Bryant and N.-U.** 488, s.l. : Trends Microbiol , 2006, Vol. 14 .

35. *Photovoltaics Power Up.* **Swanson, Richard M.** 891, s.l. : Science, 2009, Vol. 324.

36. *Prokaryotic photosynthesis and phototrophy illuminated.* **Frigaard, D.A. Bryant and N.-U.** 488, s.l. : Trends Microbiol., 2006, Vol. 14.

37. *Biochemistry.* **al., Jeremy M. Berg et.** 2002, Vol. Fifth Edition .

38. *Tailoring Porphyrins and Chlorins for Self-Assembly in Biomimetic Artificial Antenna Systems.* **Balaban, T. S.** 612-623, s.l. : Acc. Chem. Res., 2005, Vol. 38.

39. *The SIESTA method for ab initio order- N materials simulation.* **Soler, J. M. et al.** 2745 , s.l. : Journal of Physics: Condensed Matter , 2002, Vol. 14.

40. **M.Veld, P.Iavicoli, S.Haq, D.Amabilinio, R.Raval.** 1536-1538, s.l. : Chem. Commun., 2008.

41. *Crystal Structure of the Bis-pocket Porphyrin Aquo(tetramesitylporphyrinato)Zn(II).* **Song, H. & Scheidt, W. R.** 37-41, s.l. : Inorg. Chim. Act, 1990, Vol. 173.

42. *Conductive Polymers Derived from Iron, Ruthenium, and Osmium Metalloporphyrins: The Shish-Kebab Approach. .* **Collman, J. P. et al.** 4581-4585 , s.l. : Proc. Natl. Acad. Sci. USA, 1986, Vol. 83.

43. *Electrically Conductive Metallomacrocyclic Assemblies.* **Marks, T. J.** 881-889 , s.l. : Science, 1985, Vol. 227.

44. *Metal-spine conductivity in a partially oxidized metallomacrocycle: (phthalocyaninato)cobalt iodide.* **Martinsen, J. et al.** 6915-6920, s.l. : J. Am. Chem. Soc., 1985, Vol. 107.

45. *Conducting Stacked Metallophthalocyanines and Related Compounds.* **Hanack, M. & Lang, M.** 819-833 , s.l. : Adv Mater, 1994, Vol. 6.

46. *Scanning Probe Studies of Porphyrin Assemblies and Their Supramolecular Manipulation at a Solid-Liquid Interface.* **Elemans, J. A. A. W. et al.** 2070-2073, s.l. : Adv Mater , 2003, Vol. 15.

47. *CP-MAS 13C-NMR Dipolar Correlation Spectroscopy of 13C-Enriched Chlorosomes and Isolated Bacteriochlorophyll c Aggregates of Chlorobium tepidum.* **Balaban, T. S., Holzwarth, A. R., Schaffner, K., Boender, G. & de Groot, H. J. M.** 15259-15266 , s.l. : Biochemistry , 1995, Vol. 34.

48. *Green Self-Assembling Porphyrins and Chlorins as Mimics of the Natural Bacteriochlorophylls c, d, and e.* **Balaban, T. S., Linke-Schaetzel, M., Bhise, A. D., Vanthuyne, N. & Roussel, C.** 3919-3930, s.l. : Eur. J. Org. Chemi., 2004, Vol. 2004.

49. **Alivisatos, A. P.** 933, s.l. : Science, 1996, Vol. 271.

50. **Murray, C. B., Kagan, C. R. y Bawendi, M. G.** 545-610, s.l. : Annual Review of Materials Science, 2000, Vol. 30.

51. **Orrit, Brahim Lounis and Michel.** 1129, s.l. : Reports on Progress in Physics , 2005, Vol. 68.

52. **Xiao, D., y otros.** 6740-6745, s.l. : J. J. Am. Chem. Soc. , 2003, Vol. 125.

53. **Fu, H. -. y Yao, J. -.** 1434-1439, s.l. : J. Am. Chem. Soc., 2001, Vol. 123.

54. **Stangl, J., Holý, V. y Bauer, G.** 725, s.l. : Rev. Mod. Phys., 2004, Vol. 76.

55. **Kowarik, S., Gerlach, A. y Schreiber, F.** 184005, s.l. : Journal of Physics: Condensed Matter, 2008, Vol. 20.

56. *The Porphyrin Handbook.* **Kobayashi, N.** San Diego, CA : Academic Press, Vol. Vol. 15.

57. **C. G. Claessens, D. Gonzalez-Rodriguez, T. Torres.** 835, s.l. : Chem. Rev., 2002, Vol. 102.

58. **Inokuma, Y. y Osuka, A.** 2517-2526, s.l. : Dalton Trans, 2008.

59. **Claessens, C. G., y otros.** 3800-3806, s.l. : J Phys Chem B , 2005, Vol. 109.

60. **Díaz, D. D., y otros.** 4657-4660, s.l. : Tetrahedron Letters, 2007, Vol. 48.

61. **Medina, A., y otros.** 1759-1761, s.l. : Chem. Commun., 2008.

62. **S. Berner, M. Brunner, L. Ramoino, et al.,.** 175, s.l. : Chemical Physics Letters , 2001, Vol. 348.

63. **S. Berner, M. d. Wild, L. Ramoino, et al.,.** 115410, s.l. : Physical Review B, 2003, Vol. 68.

64. **S. Mannsfeld, H. Reichhard, and T. Fritz,.** 213, s.l. : Surface Science, 2002, Vol. 323.

65. **H. Yanagi, K. Ikuta, H. Mukai, et al.,.** 951 , s.l. : Nanoletters , 2002, Vol. 2.

66. **H. Yanagi, D. Schlettwein, H. Nakayama, et al.,.** 1959 , s.l. : Physical Review B , 2000, Vol. 61.

67. **C. G. Claessens, T. Torres.** 1298, s.l. : Chem. Commun., 2004.

68. *Energy transfer and trapping in photosynthesis.* **van Grondelle, R., Dekker, J. P., Gillbro, T. & Sundstrom.** 1187, s.l. : Biochim. Biophys. Acta-Bioenerg, 1994, Vols. 1-65.

69. *Conformational Adaptation and Selective Adatom Capturing of Tetrapyridyl-porphyrin Molecules on a Copper (111) Surface.* **Auwarter, W. et al.** 11279-11285 , s.l. : J. Am. Chem. Soc., 2007, Vol. 129.

70. **Ruben, M., y otros.** 3644, s.l. : Angew. Chem.Int.Ed., 2004, Vol. 43.

71. **Lehn, J. M. Science.** 2400, s.l. : Science , 2002, Vol. 295.

72. **Proc., J. M.** 4673, s.l. : Natl. Acad. Sci. USA, 2002, Vol. 99.

73. **G. M. Yaghi, G. Li, H. Li,.** 703, s.l. : Nature , 1995, Vol. 378.

74. **J. S. Seo, D. Whang, H. Lee, S. I. Jung, J. Oh, Y. J. Jeon, K. Kim.** 404, s.l. : Nature, 2000, Vol. 404.

75. **T. Yuen, D. Danilovic, K. Li, J. Li.** 07B725, s.l. : Journal of Applied Physics , 2008, Vol. 103.

76. **O. M. Yaghi, M. O´Keeffe, N. W. Ockwig, H. K. Chae, M. Eddaoudi, J. Kim.** 705, s.l. : Science, 2003, Vol. 423.

77. **Messina, P., y otros.** 14000, s.l. : J. Am. Chem. Soc., 2002, Vol. 124.

78. **Stepanow, S., y otros.** 229, s.l. : Natur. Mater., 2004, Vol. 3.

79. **Stepanow, S., y otros.** 710, s.l. : Angew. Chem. Int. Ed., 2007, Vol. 46.

80. **Ortega Lorenzo, M., y otros.** 376, s.l. : Nature, 2000, Vol. 404.

81. **N.Lin, A.Dmitriev, J.Weckesser,J.V.Barth and K.Kern.** 24, s.l. : Angew.Chem.Int.Ed., 2002, Vol. 41.

82. **T.Classen, G.Fratesi, G.Costantini, S.Fabris, F.L. Stadler, C.Kim, S.de Gironcoli, S.Baroni and K.Kern.** 6142-6145, s.l. : Angew.Chem.Int.Ed., 2005, Vol. 41.

83. **D.S. Martin, R.J. Cole and S.Haq.** 171-181, s.l. : Surface Science, 2003, Vol. 539.

84. **T Fujitani, Y Choi, M Sano, Y Kushida and J Nakamura.** 1235, s.l. : J Phys Chem B, 2000, Vol. 104.

85. **J. E. Crowell, J. G. Chen, J. T. Yates.** 3111, s.l. : Journal of Chemical Physics, 1986, Vol. 85.

6. **P. R. Davies, M. W. Roberts, N. Shukla.** S237, s.l. : Journal of Physical Chemistry C, 1991, Vol. 3.

87. **J. G. Chen, J. E. Crowell, J. T. Yates.** 733, s.l. : Surface Science, 1986, Vol. 172.

88. **J. E. Crowell, J. G. Chen, J. T. Yates.** 97, s.l. : Spectroscopy Related Phenomena , 1986, Vol. 39.

89. **P. Parent, C. Laffon, G. Tourillon, A. Cassuto.** 5058, s.l. : Journal of Physical Chemistry , 1995, Vol. 99.

90. **F. Bournel, C. Laffon, P. Parent, G. Tourillon.** 228, s.l. : Surface Science , 1995, Vols. 352-354.

91. **F. Klappenberger, A. Weber-Bargioni, W. Auwärter, M. Marschall, A. Schiffrin, J. V. Barth.** 214702, s.l. : The Journal of Chemical Physics, 2008, Vol. 129.